DOT/FAA/AR-99/34

Office of Aviation Research
Washington, D.C. 20591

Characterization of Early Stages of Corrosion Fatigue in Aircraft Skin

Phase II: Interpretation of Corrosion-Fatigue Fracture Surfaces in Alclad 2024-T3 Aluminum Alloy Sheet

May 1999

Phase II Report

This document is available to the public through the National Technical Information Service (NTIS), Springfield, Virginia 22161.

U.S. Department of Transportation
Federal Aviation Administration

NOTICE

This document is disseminated under the sponsorship of the U.S. Department of Transportation in the interest of information exchange. The United States Government assumes no liability for the contents or use thereof. The United States Government does not endorse products or manufacturers. Trade or manufacturer's names appear herein solely because they are considered essential to the objective of this report. This document does not constitute FAA certification policy. Consult your local FAA aircraft certification office as to its use.

This report is available at the Federal Aviation Administration William J. Hughes Technical Center's Full-Text Technical Reports page: www.tc.faa.gov/its/act141/reportpage.html in Adobe Acrobat portable document format (PDF).

Technical Report Documentation Page

1. Report No.	2. Government Accession No.	3. Recipient's Catalog No.
DOT/FAA/AR-99/34		

4. Title and Subtitle	5. Report Date
CHARACTERIZATION OF EARLY STAGES OF CORROSION FATIGUE IN AIRCRAFT SKIN PHASE II: INTERPRETATION OF CORROSION-FATIGUE FRACTURE SURFACES IN ALCLAD 2024-T3 ALUMINUM ALLOY SHEET	May 1999
	6. Performing Organization Code PYD-5082
7. Author(s) C. G. Schmidt, T. Kobayashi, and D. A. Shockey	8. Performing Organization Report No.
9. Performing Organization Name and Address SRI International 333 Ravenswood Avenue Menlo Park, CA 94025-3493	10. Work Unit No. (TRAIS)
	11. Contract or Grant No. 95-G-065
12. Sponsoring Agency Name and Address U.S. Department of Transportation Federal Aviation Administration Office of Aviation Research Washington, DC 20591	13. Type of Report and Period Covered October 95 – September 98 Phase II Report
	14. Sponsoring Agency Code ACE-100

15. Supplementary Notes

The FAA William J. Hughes Technical Center Project Monitor: Dr. Thomas Flournoy

16. Abstract

New methods were developed and applied to extract and interpret information from the fracture surfaces of corrosion-fatigue specimens of clad and bare 2024-T3 aluminum sheet. We developed two fracture surface topography analysis methods that characterize the effects of environment and a fracture surface analysis and finite element modeling approach to detect and quantify overloads that occurred during fatigue crack propagation. We used these methods to perform a detailed analysis of the fracture surface topography produced in the early stages of corrosion fatigue, and developed an understanding of the effect of environment on the crack nucleation mechanism based on fracture surface features.

In addition, cyclic load experiments were conducted on bare and clad 2024-T3 sheet under vacuum and in air, salt water, and arsenated salt water environments to assess the effects of environment, stress, and material condition on nucleation and early propagation kinetics of corrosion-fatigue cracks. For bare 2024-T3 sheet, substantial reductions in fatigue life were observed when the environment produced elongated pits associated with constituent particle corrosion. For clad 2024-T3 sheet, reductions in fatigue life were observed in environments that did not produce pitting (e.g., laboratory air and salt water). A likely mechanism for enhanced crack nucleation in 2024-T3 sheet with pure aluminum clad is the weakening effect of hydrogen on pure aluminum and the concomitant enhancement of cracking kinetics.

The analytical methods developed and the analyses performed bear directly on the understanding of corrosion-fatigue in commercial aircraft through the relevancy of the materials, loading conditions, and test environments. Ultimately, we expect that the analysis techniques developed in this program, combined with the results obtained by other participants in the FAA's National Aging Aircraft Research Program, will lead to more accurate predictions of and additional opportunities to mitigate corrosion-fatigue cracking in aircraft skin.

17. Key Words			18. Distribution Statement
Corrosion Fatigue 2024-T3 Alclad	Crack nucleation Aircraft skin Pitting Hydrogen	Aluminum Clad	This document is available to the public through the National Technical Information Service (NTIS), Springfield, Virginia 22161.

19. Security Classif. (of this report)	20. Security Classif. (of this page)	21. No. of Pages	22. Price
Unclassified	Unclassified	76	

Form DOT F1700.7 (8-72) Reproduction of completed page authorized

CONTENTS

Section		Page
	EXECUTIVE SUMMARY	vii
1	INTRODUCTION	1
	1.1 Nucleation and Growth Kinetics of Corrosion Fatigue Cracks	1
	1.2 Corrosion Fatigue Experience in Commercial Aircraft	2
	1.3 Analysis of Corrosion Fatigue Failure Surfaces	4
2	EFFECT OF STRESS INTENSITY RANGE AND ENVIRONMENT ON FRACTURE SURFACE CHARACTERISTICS	5
	2.1 Background	5
	2.2 Fatigue Experiments and Fracture Surface Topography Characterization	6
	2.3 Fourier Analysis of Fracture Surface Topography	10
	2.4 Comparison of Conjugate Fracture Surface Topographs	10
	2.5 Discussion	15
	2.6 Summary	16
3	CORRELATION OF FRACTURE SURFACE TOPOGRAPHY WITH FATIGUE LOAD HISTORY	17
	3.1 Background	17
	3.2 Experimental Procedure	17
	3.3 Experimental Results	18
	3.4 Finite Element Simulations	20
	3.5 Discussion	23
	3.6 Summary	25
4	DETAILED FRACTURE SURFACE ANALYSIS OF THE EARLY STAGES OF A CORROSION FATIGUE CRACK	26
	4.1 Experimental Procedures	26
	4.2 Fracture Surface Topography Analysis (FRASTA)	28
	4.3 Discussion	36
	4.4 Summary	37
5	FACTORS AFFECTING FATIGUE CRACK NUCLEATION	38
	5.1 Experimental Procedures	38
	5.2 Results	38
	5.3 Discussion	55
	5.4 Summary	57
6	REFERENCES	59
	APPENDIX: SEM STEREO PROGRAM DEVELOPMENT	

FIGURES

Figure		Page
1	Effect of maximum stress intensity change on crack growth rate	6
2	Crack growth history of a cyclically loaded center-cracked panel of 2024-T3 aluminum in air and under vacuum	7
3	SEM micrograph showing the fatigue fracture surface morphology produced in air and under vacuum	8
4	High-magnification SEM micrographs of a fatigue fracture surface created in air and under vacuum	9
5	Gray-scale images and perspective views of the topographics of conjugate fracture surfaces produced under low and high ΔK and K_{max} fatigue conditions	11
6	Fast Fourier transform elevation power spectral density curves for conjugate fatigue failure surfaces produced under high and low ΔK and K_{max} fatigue conditions	12
7	Elevation power spectral density curves for fatigue surfaces produced in air and under vacuum	12
8	Reconstruction of the crack front configuration by superimposing fracture surface topographs	13
9	A series of plan views of a crack front at increasing topograph displacements	14
10	Effect of environment on fracture progression curve (FPC)	14
11	Comparison of overload history to perturbations in fracture progression curve (FPC)	18
12	Fracture progression curve (FPC) with baseline	19
13	Monotonic and cyclic stress-strain behavior of 2024-T3 aluminum alloy	20
14	Finite element mesh around crack tip in center-cracked panel specimen	21
15	Cyclically hardened areas near crack tip	22
16	Computed crack tip geometries	22
17	Comparison of computed and measured FPC perturbation heights resulting from overloads	24

Figure		Page

18 Cross section of representative aircraft skin 26

19 SEM micrograph of fracture surface showing area where crack initiated 27

20 Conjugate surfaces of the crack initiation area 27

21 Contrast and gray-scale topography images of conjugate surfaces of the crack initiation site 29

22 A series of FAPPs produced by FRASTA showing crack formation and growth process 30

23 Superposition of FAPPs on SEM micrograph relating fracture processes to microstructural features 32

24 Fractured area increase rate as a function of conjugate surface spacing 33

25 A series of XSPs made along the line A-A in the thickness direction 34

26 A series of XSPs made along the line B-B that is parallel to the exterior surface of the plate 35

27 Effect of stress, cladding, and environment on the fatigue life of 2024-T3 aluminum 40

28 Fracture surface appearance of Alclad 2024-T3 fatigue specimens tested in vacuum 41

29 Comparison of fatigue life of Alclad 2024-T3 aluminum under vacuum and in air 43

30 Fracture surface appearance of Alclad 2024-T3 fatigue specimens tested in air 44

31 Fracture surface appearance of Alclad 2024-T3 fatigue specimens tested in 0.5 M NaCl solution 46

32 Fracture surface appearance of Alclad 2024-T3 fatigue specimens tested in 0.5 M NaCl solution + 0.13 M As_2O_3 48

33 Fracture surface appearance of bare 2024-T3 fatigue specimens tested in vacuum .. 50

34 Fracture surface appearance of bare 2024-T3 fatigue specimens tested in air 52

35 Fracture surface appearance of bare 2024-T3 fatigue specimens tested in 0.5 M NaCl solution 54

TABLES

Table		Page
1.	Corrosion-fatigue test results	39

EXECUTIVE SUMMARY

New methods were developed and applied to extract and interpret information from the fracture surfaces of corrosion-fatigue specimens of clad and bare 2024-T3 aluminum sheet. We developed two fracture surface topography analysis methods that characterize the effects of environment and a fracture surface analysis and finite element modeling approach to detect and quantify overloads that occurred during fatigue crack propagation. We used these methods to perform a detailed analysis of the fracture surface topography produced in the early stages of corrosion fatigue and developed an understanding of the effect of environment on the crack nucleation mechanism based on fracture surface features.

We found that

- Fourier analysis of topographic data from fracture surfaces of cyclically loaded 2024-T3 aluminum fatigue crack growth specimens detected variations in load and environmental conditions that are not easily detected by conventional scanning electron microscope (SEM) examination.
- Fracture Surface Topography Analysis (FRASTA) distinguished between fracture surfaces formed in air and vacuum using cyclically loaded 2024-T3 specimens.
- FRASTA detected the location on the fracture surface of overloads applied during fatigue crack propagation in 2024-T3 aluminum alloy and provided an estimate of their magnitude.
- FRASTA showed the locations and sequence of corrosion-fatigue crack nucleation, the crack front structure and position evolution, and the crack propagation directions in clad 2024-T3 aluminum aircraft skin.

In addition, cyclic load experiments were conducted on bare and clad 2024-T3 sheet under vacuum and in air, salt water, and arsenated salt water environments to assess the effects of environment, stress, and material condition on nucleation and early propagation kinetics of corrosion-fatigue cracks. For bare 2024-T3 sheet, substantial reductions in fatigue life were observed when the environment produced elongated pits associated with constituent particle corrosion. For clad 2024-T3 sheet, reductions in fatigue life were observed in environments that did not produce pitting (e.g., laboratory air and salt water). A likely mechanism for enhanced crack nucleation in 2024-T3 sheet with pure aluminum clad is the weakening effect of hydrogen on pure aluminum and the concomitant enhancement of cracking kinetics.

The analytical methods developed and the analyses performed bear directly on the understanding of corrosion-fatigue in commercial aircraft through the relevancy of the materials, loading conditions, and test environments. Ultimately, we expect that the analysis techniques developed in this program, combined with the results obtained by other participants in the National Aging Aircraft Research Program (NAARP), will lead to more accurate predictions of and additional opportunities to mitigate corrosion-fatigue cracking in aircraft skin.

1. INTRODUCTION.

Corrosion fatigue in difficult-to-access areas of an aircraft fuselage is an occasional problem in commercial aircraft and has the potential to affect the structural integrity and the useful life of aircraft structures. Although the effects of fatigue and corrosion have been extensively documented, their synergy is not thoroughly understood and continues to be an area of considerable interest. As a result, the Federal Aviation Administration (FAA), through the National Aging Aircraft Research Program (NAARP) initiated a program of research aimed at a quantitative understanding of the relationship between fatigue and aggressive chemical environments.

Specifically, this program seeks to develop an understanding of the synergism between mechanical fatigue and corrosion; to develop crack growth rate data that will allow estimates of residual strength of fuselage panels with cracks; and to develop inspection interval criteria with an associated probability of detection for each nondestructive inspection technique.* SRI International designed a three-part investigation to contribute to achieving these objectives and to complement ongoing research supported by the FAA Grants Program, National Aeronautics and Space Administration (NASA), and aircraft manufacturers.

1.1 NUCLEATION AND GROWTH KINETICS OF CORROSION FATIGUE CRACKS.

In September 1995, we completed the first part of this program, a study aimed at characterizing corrosion-fatigue crack nucleation and growth kinetics.[1] In this first phase of the program, we developed an experimental technique for producing corrosion fatigue cracks in the laboratory. This was developed to allow examination of crack nucleation and growth kinetics in both a statistical and deterministic manner. A range of environments, material conditions, and loading conditions were investigated experimentally in an effort to assess their effects on the crack nucleation and growth rate.

Findings include the following.

- Crack nucleation in bare material (i.e., clad and paint removed) was slower than crack nucleation in clad material. The mechanisms of crack nucleation were substantially different in the two materials: in bare material, cracks nucleated at constituent particles; whereas in clad material, cracks usually nucleated at or near crystallographic pit colonies.

*Program Plan, National Aging Aircraft Research Program, DOT/FAA/CT-88/32-1, Department of Transportation, Federal Aviation Administration Technical Center, Atlantic City International Airport, New Jersey 08405 (September 1991).

- Crack nucleation from crystallographic pits in the clad did not always occur at the largest pit. The lack of correlation between crack nucleation sites and geometrical features suggests that the effect of a pit is more than simply to raise the local stress. A high local hydrogen concentration in the clad created by accelerated corrosion processes associated with pitting may promote cracking in a nearby favorably oriented grain.

- In aircraft skin, the crack nucleation mechanism that dominates depends on environment (e.g., pH), the presence or absence of a clad layer, and additional variables that were not investigated, such as material composition and heat treatment.

- Crack propagation rates in the early stages of corrosion fatigue were slightly higher in a pH 2 environment than in pH 6 or pH 10 environments. This result is generally consistent with the results of other investigators and is attributed to enhanced cathodic reaction rates in acidic solutions.

- Surface roughness did not affect the early stages of corrosion-fatigue crack propagation. However, cracks growing from exposed edges of painted skin material had a slightly higher crack growth rate than unpainted material. We speculate that a local occluded environment might accelerate crack growth rates.

Laboratory tests were performed under conditions relevant to conditions in service without necessarily simulating them. The intent was to conduct corrosion fatigue tests to clarify the underlying mechanisms. Additional experimental and analytical work will be necessary to translate a new or more comprehensive understanding of the early stages of damage into a more reliable life prediction capability and new opportunities for mitigating corrosion-fatigue cracking in aircraft skin.

1.2 CORROSION FATIGUE EXPERIENCE IN COMMERCIAL AIRCRAFT.

The second part of the program, a study of corrosion-fatigue experience in commercial aircraft, was completed in May 1996.[2] The specific objectives were to establish the pervasiveness of corrosion fatigue in the nation's airliners and to obtain information for checking the fidelity of damage produced in the laboratory. In pursuit of these objectives, we

- visited an airline maintenance facility to discuss the observations and experiences of inspectors, maintenance engineers, and managers.

- visited an airframe manufacturer to discuss the design philosophy and experiences of aircraft designers and engineers.

- reviewed FAA documents that address corrosion and fatigue [e.g., Airworthiness Directives (ADs) and Advisory Circulars (ACs)].

- reviewed charters and findings of industry working groups, task forces, and programs [e.g., Industry Steering Committee, Industry Working Groups, Airworthiness Assurance Task Force, and Corrosion Prevention and Control Program (CPCP)].

- reviewed the National Transportation Safety Board's report of the Aloha Airlines incident of 1988.

- reviewed operation and maintenance documents [e.g., Service Difficulty Reports (SDRs), commercial airline documentation, and airframe manufacturer documentation].

- conducted telephone interviews with personnel responsible for U.S. Air Force (USAF) aircraft maintenance.

- reviewed USAF programs that address aircraft maintenance issues.

- reviewed published accounts that describe case histories of corrosion fatigue in aircraft fuselage structures.

Firm conclusions regarding the prevalence and characteristics of corrosion fatigue damage in the commercial fleet could not be drawn from the findings. The Service Difficulty Reports (SDRs), while having the potential to indicate the breadth of corrosion and fatigue occurrences, were not designed to provide all the information needed for the assessment purposes of this study. Moreover, the SDRs were usually only partially completed, were often missing from the logs, and are not used consistently throughout the industry as a reporting mechanism. The other available documentation (Advisory Circulars, Airworthiness Directives, Corrosion Prevention and Control Program documents) likewise provided little insight into the occurrence frequency and conditions that resulted in corrosion fatigue. Similarly for the USAF, the inspection and maintenance protocols at the base and program depot maintenance levels do not explicitly look for and classify damage as corrosion fatigue. The major airframe manufacturers have examined many damaged panels, and a data base could possibly be compiled from their experience that might provide unique and valuable insights into corrosion-fatigue processes. However, airframe manufacturers are constrained from sharing this information by proprietary concerns.

Thus, the corrosion fatigue experience of commercial aircraft could not be determined from available historical data and remains unassessed. An evaluation of the pervasiveness and severity of corrosion fatigue will require a more diligent and more focused effort to document the results of inspections as well as the detailed examination of selected fuselage panels that contain corrosion-fatigue damage. The cooperation of the airlines and aircraft manufacturers is essential. A comprehensive effort would indicate whether corrosion fatigue should be a concern to commercial aviation and, if so, would assist in developing new procedures for controlling and preventing structural degradation. Whether corrosion fatigue occurs frequently or not, the results of a such a study will increase confidence in extending the operational life of the fleet.

1.3 ANALYSIS OF CORROSION FATIGUE FAILURE SURFACES.

The third part of the SRI effort was aimed at developing and applying new methods to extract and interpret information from the fracture surfaces of corrosion fatigue specimens. The fracture surfaces produced during corrosion-fatigue are potentially a rich source of information about the environment history, stress history, and the mechanisms of crack nucleation and propagation.

We sought in particular to gain insight into the corrosion damage/crack transition. Most previous studies of environment effects on corrosion fatigue have emphasized effects on the rate of propagation of long cracks, as opposed to the nucleation of cracks. This is, at least in part, due to the emphasis of modern design practice, such as damage tolerance design, on the fatigue crack propagation rate. Less clear, though, is the utility of understanding the effect of environment on the nucleation kinetics of fatigue cracks, because current design practices do not require a knowledge of crack nucleation kinetics.

Despite the lack of a clear, direct, and immediate application of crack nucleation kinetics in aircraft design, improving our understanding of the environmental effects on fatigue crack nucleation has significant value. That value stems from the continual need to develop improved measures to retard the effects of environment and fatigue wherever and whenever possible. The inhibitive measures could involve the design of the metallic components of the skin (core and clad), the choice of coatings (primers, paints, and corrosion inhibitors), and the design of skin splices.

This report describes fractographic examinations of specimens of clad and bare 2024-T3 aluminum sheet. From these investigations, we developed (1) two fracture surface topography analysis methods that characterize the effects of environment, (2) a fracture surface analysis tool and finite element modeling approach to quantify overloads during fatigue crack propagation, (3) a detailed analysis of the fracture surface topography produced in the early stages of corrosion fatigue, and (4) an understanding of the effect of environment on the crack nucleation mechanism based on fracture surface features.

The analytical methods developed and the analyses performed bear directly on the understanding of corrosion-fatigue in commercial aircraft through the relevancy of the materials, loading conditions, and test environments. Ultimately, we expect that the results of this program, combined with the efforts of other participants in the NAARP, will lead to more accurate predictions of and additional opportunities to mitigate corrosion-fatigue cracking in aircraft skin.

2. EFFECT OF STRESS INTENSITY RANGE AND ENVIRONMENT ON FRACTURE SURFACE CHARACTERISTICS.

2.1 BACKGROUND.

The growth history of a fatigue crack is governed in large part by load spectrum and environment. Thus, when a structural component fails under oscillatory loads, the failure analyst attempting to establish the cause of failure often seeks to learn the service conditions. Unfortunately, a record of load spectrum is not usually available. This project explored the possibility of determining the load spectrum from post-fracture analysis.

Because the important loads in a spectrum are those that affect the crack process, it may be possible to deduce the load spectrum (in particular, the local load spectrum) by examining the fracture surfaces of the failed part or a part containing a crack. By propagating the crack, by blunting the crack tip, or by retarding crack growth, these loads should manifest themselves somehow on the fracture surfaces. Fracture surfaces, therefore, may act as a load spectrum gauge providing details of the maximum and minimum loads, their frequency and sequence, and the occurrence and severity of overloads as well as changes in environment.

However, a way is needed to read the fracture surfaces and interpret the features in terms of the important parameters of the load. A procedure for deducing the stress intensity range, ΔK, already exists. When fatigue striations can be detected, striation spacing is sometimes correlated with crack growth rate,[3,4] and growth rate is empirically related to the stress intensity range, ΔK, by the Paris equation.[5] More recently, a relationship was reported between the striation height-to-spacing ratio and R, the ratio of minimum to maximum load in a load cycle.[6,7] Combining these relationships suggests that the maximum and minimum loads of the spectrum are obtainable from the fracture surfaces.

In practice, however, the use of fatigue striations in failure analysis is often difficult.[8] In many cases, striations or regions containing enough uniform striations for meaningful analysis cannot be found. Moreover, the crack growth rate deduced from striations can differ significantly (by as much as a factor of 20) from the measured macrocrack growth rate. Nevertheless, it seems likely that valuable information regarding crack growth rate, load spectrum, and environment conditions is encrypted in the topography of the fracture surfaces.

SRI has developed a technique that can characterize fracture surface topography in three dimensions, at high resolution, and with reasonable speed. We also use a fast Fourier transform analysis of the topography for specifying a signature curve reflective of causative failure conditions.

2.2 FATIGUE EXPERIMENTS AND FRACTURE SURFACE TOPOGRAPHY CHARACTERIZATION.

To produce fracture surfaces for topographic analysis, we performed fatigue experiments on center-cracked panel specimens of 1-mm-thick 2024-T3 aluminum sheet typical of that used for aircraft fuselage skin. To investigate the effect of stress intensity range, ΔK, and maximum stress intensity, K_{max}, a fatigue test was performed in which the crack was propagated several millimeters at a ΔK of 4.8 MPa√m and a K_{max} of 12 MPa√m and then an additional several millimeters at a ΔK of 8 MPa√m and a K_{max} of 20 MPa√m (see figure 1). The increase in K_{max} produced a substantial increase in the crack growth rate from about 2×10^{-5} mm/cycle to 9×10^{-5} mm/cycle. To investigate the effect of environment, a specimen was cyclically loaded under constant K_{max} conditions but with variations in the environment.

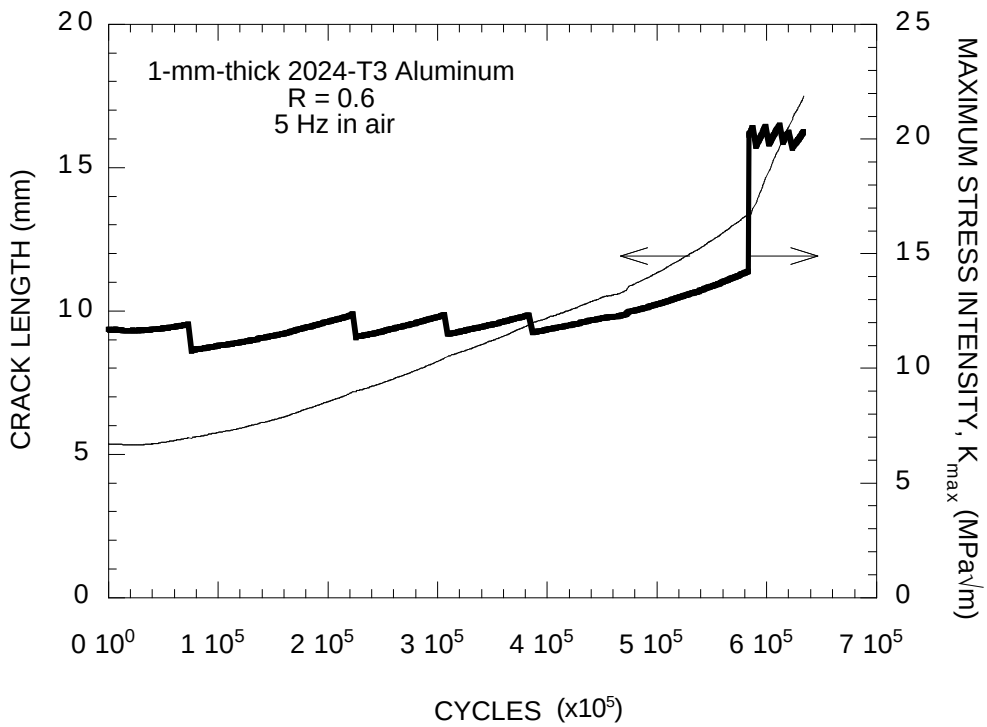

FIGURE 1. EFFECTS OF MAXIMUM STRESS INTENSITY CHANGE ON CRACK GROWTH RATE.

In these experiments, a vacuum of about 10^{-6} torr was imposed while the fatigue crack propagated a few millimeters. Then, the environment was suddenly changed to laboratory air as cyclic loading continued. Several changes in environment were imposed in this way under a range of loading conditions. The changes in environment immediately and reproducibly changed the crack growth rate such that the rate in air was about three times the rate under vacuum, as shown in figure 2(a), (b), and (c). The stress ratio, R, was constant at 0.6, and the load cycle frequency was 5 Hz in all tests.

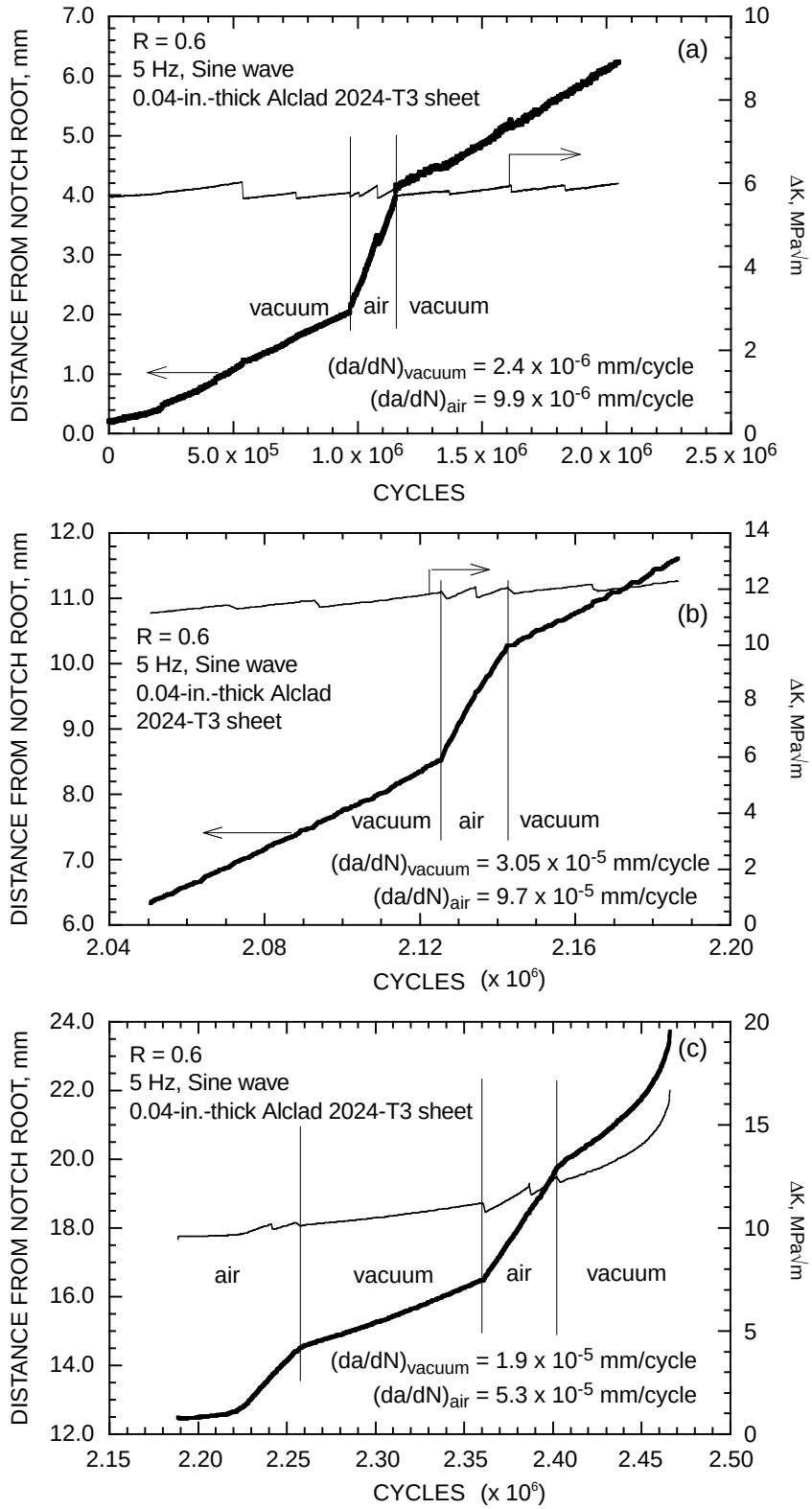

FIGURE 2. CRACK GROWTH HISTORY OF A CYCLICALLY LOADED CENTER-CRACKED PANEL OF 2034-T3 ALUMINUM IN AIR AND UNDER VACUUM.

Figure 3 shows an example of the change in fracture surface appearance at the transition between crack propagation under vacuum and in air. There is a suggestion of denser features on the fracture surface generated in air; however, the difference is barely detectable by visual inspection. Examination of high-magnification SEM micrographs (see figure 4 for an example) shows no discernible difference in the fracture surface features for air and vacuum crack growth environments. We will show that Fourier analysis and FRASTA are capable of detecting and quantifying differences in fracture surface characteristics that are almost undetected by conventional SEM examination.

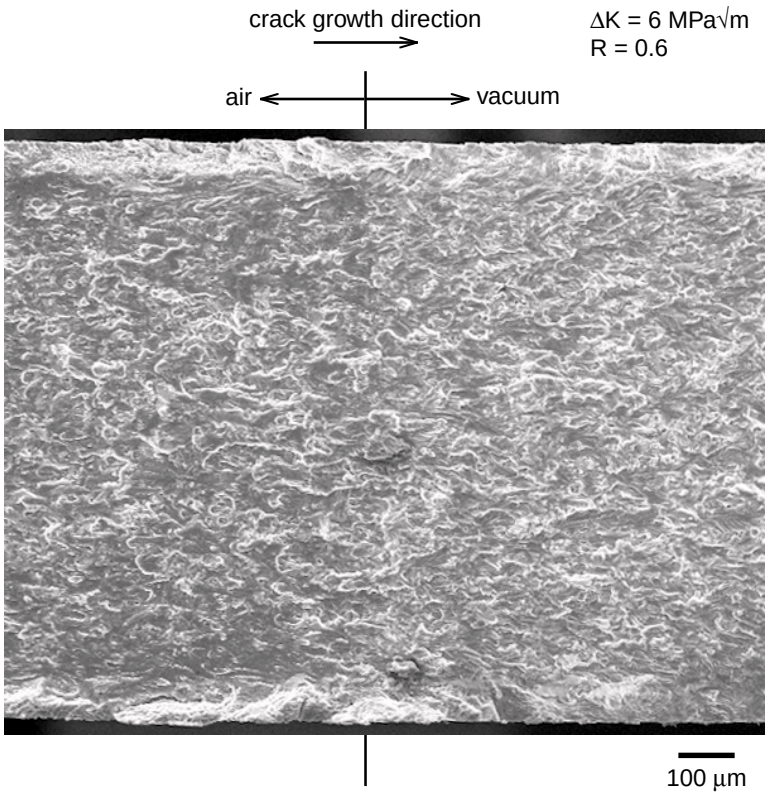

FIGURE 3. SEM MICROGRAPH SHOWING THE FATIGUE FRACTURE SURFACE MORPHOLOGY PRODUCED IN AIR AND UNDER VACUUM.

After specimen failure, elevation maps of selected areas of the conjugate fracture surfaces were made using the FRASTAscope, a system we developed consisting of a confocal optics scanning laser microscope* (COSLM), a precision, computer-controlled x-y-θ stage,† and computer programs to control data acquisition, manipulation, and display. When a 50x objective is used, the

*Model 1LM21W, Lasertec Corporation, Yokohama, Japan.
† 6- x 6-inch HighLine Dual-Axis Stage, Pacific Precision Laboratories, Inc., Chatsworth, CA.

FRASTAscope surveys a rectangular fracture surface area of 223 x 149 μm by optically scanning in the x direction and mechanically stepping in the y direction, recording the strength of the signal for each pixel in a 600 x 400 pixel array. After completing the survey of the initial plane, the specimen is raised in the z direction by 1/256 of the elevation range of the rectangular area and resurveyed to measure the new signal strength for each pixel in the array. The procedure of incrementally raising the specimen, surveying the area, and recording signal strength is repeated until the elevation range is traversed.

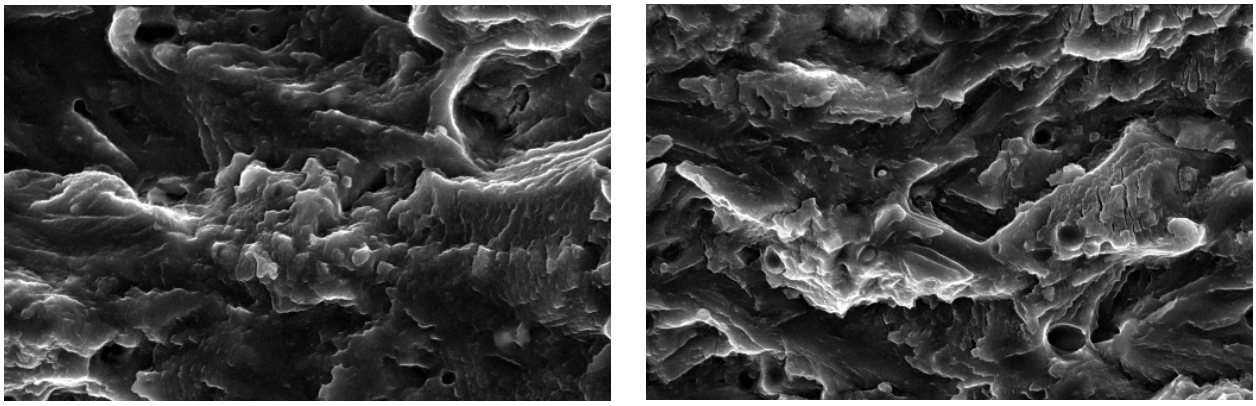

(a) Air (b) Vacuum

10 μm

FIGURE 4. HIGH-MAGNIFICATION SEM MICROGRAPHS OF A FATIGUE FRACTURE SURFACE CREATED IN AIR AND UNDER VACUUM.

Because of the very short depth of focus of the confocal optics (60 nm), the strength of the signal from a pixel is very sensitive to the distance of the surface in the pixel from the focal plane. The height of the area in each pixel is the z-position at which signal strength is maximum. Thus, the maximum signal strength position as a function of x and y provides an elevation map of the rectangular area. The x-y-z characterization requires 10 to 100 seconds depending on the fracture surface topography and reflectivity. At the most sensitive setting, in-plane and out-of-plane resolutions are 0.25 μm and 60 nm, respectively. Larger areas of fracture surfaces are characterized by abutting the elevation data from adjacent areas. Depending on the size of the area one desires to examine, the abutting operation (which is also software controlled) can take several hours.

An alternative procedure for characterizing fracture surface topography in three dimensions is stereoscopy in which stereo views are taken with the SEM and the digitized elevation data are evaluated with a software program.[9] The SEM procedure can characterize a fracture surface at higher magnification than the COSLM procedure and is thus useful for analyzing fracture surface details. Furthermore, by use of low magnification, say 10x, larger areas (125 mm^2) can be analyzed at high data density in about 30 to 40 seconds.

Both methods capture the elevation data in digital form. The data can be displayed in gray-scale images and in three-dimensional perspective plots.

2.3 FOURIER ANALYSIS OF FRACTURE SURFACE TOPOGRAPHY.

Figure 5 shows gray-scale images and perspective views of conjugate areas from the low and high ΔK and K_{max} surfaces obtained with the COSLM-based FRASTAscope. The shades of gray indicate relative height: lighter areas are higher; darker areas are lower.

Figure 5 provides a physical representation of the topographies that is relatively easy to grasp. However, differences in the topographies arising from differences in ΔK and K_{max} are not easily discerned. To obtain an alternative representation of the topography, a one-dimensional fast Fourier transform operation was applied, row by row, to 400 rows of 400 elevation data points. Figure 6 shows the "power spectral density" curve obtained by averaging the 400 rows. In the figure, the sum of the squares of the real and imaginary components of the elevation amplitudes normalized by a crack extension distance is presented as a function of spatial frequency or roughness wavelength rather than as a function of position (as in figure 5). The power spectral density curve (a name that has its origins in Fourier applications to electrical signals) might be more aptly called the elevation power spectral density (EPSD) when topographic information is analyzed.

The EPSD curves in figure 6 for the fracture surfaces produced under low ΔK and K_{max} differ measurably from those produced at high ΔK and K_{max}. Thus, EPSD characterization discriminates these important load parameters. Moreover, the EPSDs of conjugate surfaces are nearly identical, suggesting that topographies produced under identical conditions are unique and reproducible.

Figure 7 shows the EPSD curves for the specimen fatigued under vacuum and then in air. A small but distinct difference is apparent above a spatial frequency of 3×10^4 m^{-1} (or wavelength less than 30 μm). Furthermore, the EPSD curve for the area fatigued in air closely matches the curve for the low ΔK area obtained on the previous specimen, demonstrating specimen-to-specimen reproducibility of fracture surface topography generated under similar conditions.

Thus, fracture surface topography appears to be sensitive to loading and environment conditions, and the EPSD curve appears to be a characteristic signature of the topography that reflects these conditions. Moreover, the EPSD is obtained objectively and efficiently and may be more representative of macrocrack behavior than fatigue striations.

2.4 COMPARISON OF CONJUGATE FRACTURE SURFACE TOPOGRAPHS.

The topographies of a 1.0-mm-wide strip of the conjugate fracture surfaces in the center of the specimen were quantified with a COSLM in the crack growth direction. With the aid of computer software, the conjugate topographs were positioned and aligned with respect to each other to approximate the configuration of the fracture surfaces during the fatigue test, as shown schematically in figure 8. A cross-sectional view of the intersecting topographs shows the crack in profile, and a projection of the crack front configuration is obtainable in a plan view. Damage in the process zone ahead of the crack front is shown in both views. Areas where the topographs overlap are shown in black and are interpreted as areas where the material is unbroken; areas where

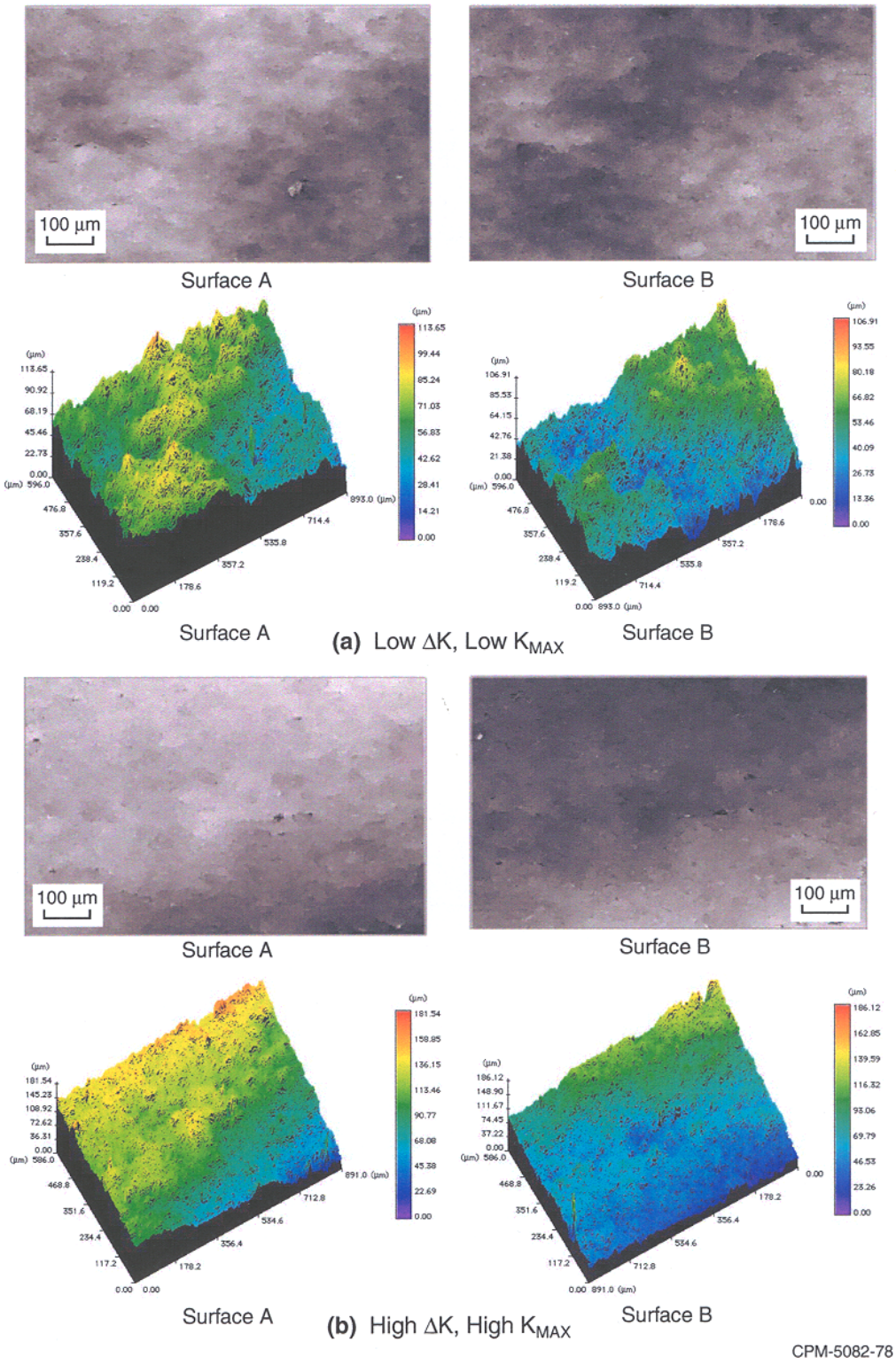

FIGURE 5. GRAY-SCALE IMAGES AND PERSPECTIVE VIEWS OF THE TOPOGRAPHICS OF CONJUGATE FRACTURE SURFACES PRODUCED UNDER LOW AND HIGH ΔK AND K_{MAX} FATIGUE CONDITIONS.

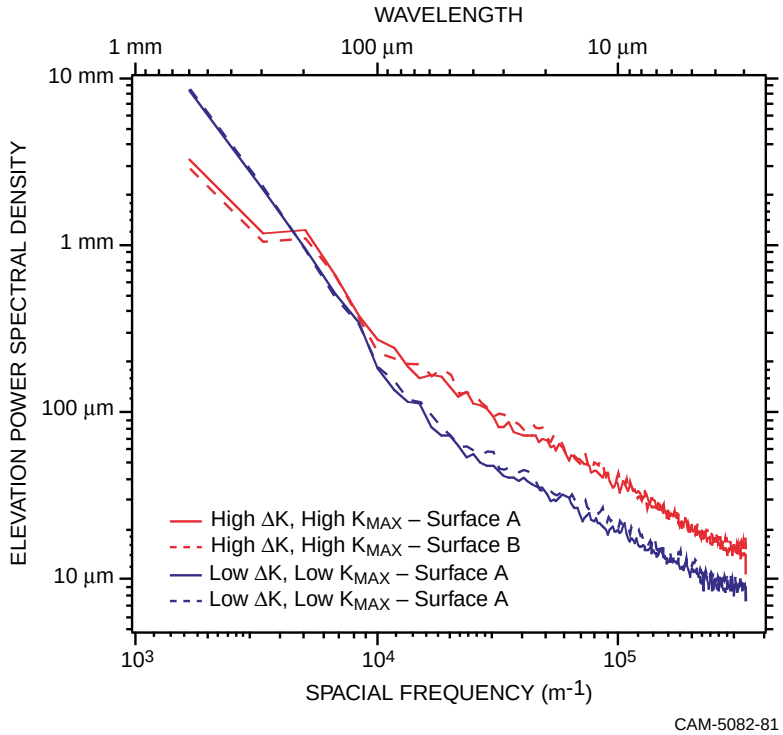

FIGURE 6. FAST FOURIER TRANSFORM ELEVATION POWER SPECTRAL DENSITY CURVES FOR CONJUGATE FATIGUE FAILURE SURFACES PRODUCED UNDER HIGH AND LOW ΔK AND K_{max} FATIGUE CONDITIONS.

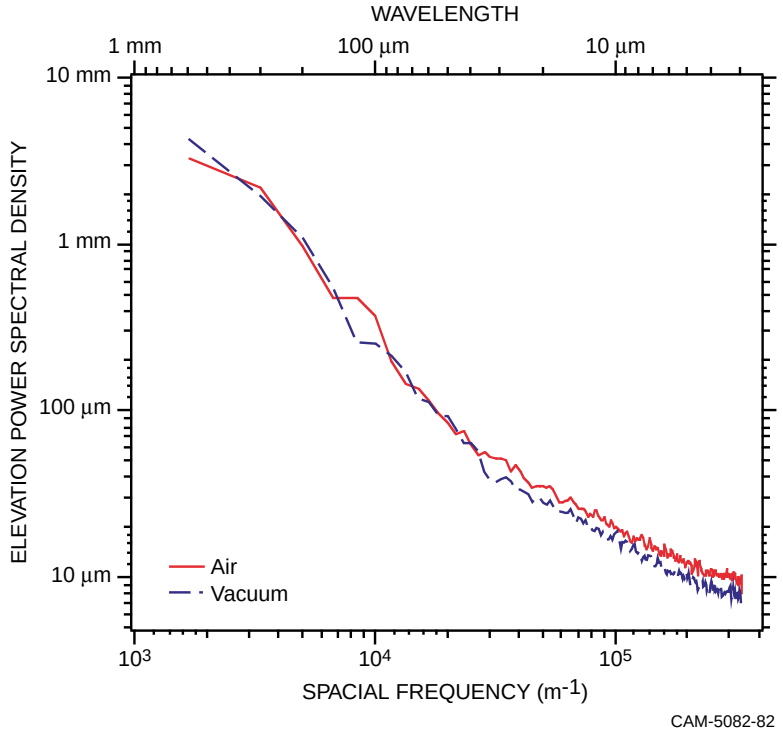

FIGURE 7. ELEVATION POWER SPECTRAL DENSITY CURVES FOR FATIGUE SURFACES PRODUCED IN AIR AND UNDER VACUUM.

the topographs are separated are shown in white and are taken as fractured material. The procedure of comparing fracture surface topographs to analyze fracture is known as FRASTA (fracture surface topography analysis) and has been described elsewhere.[10,11]

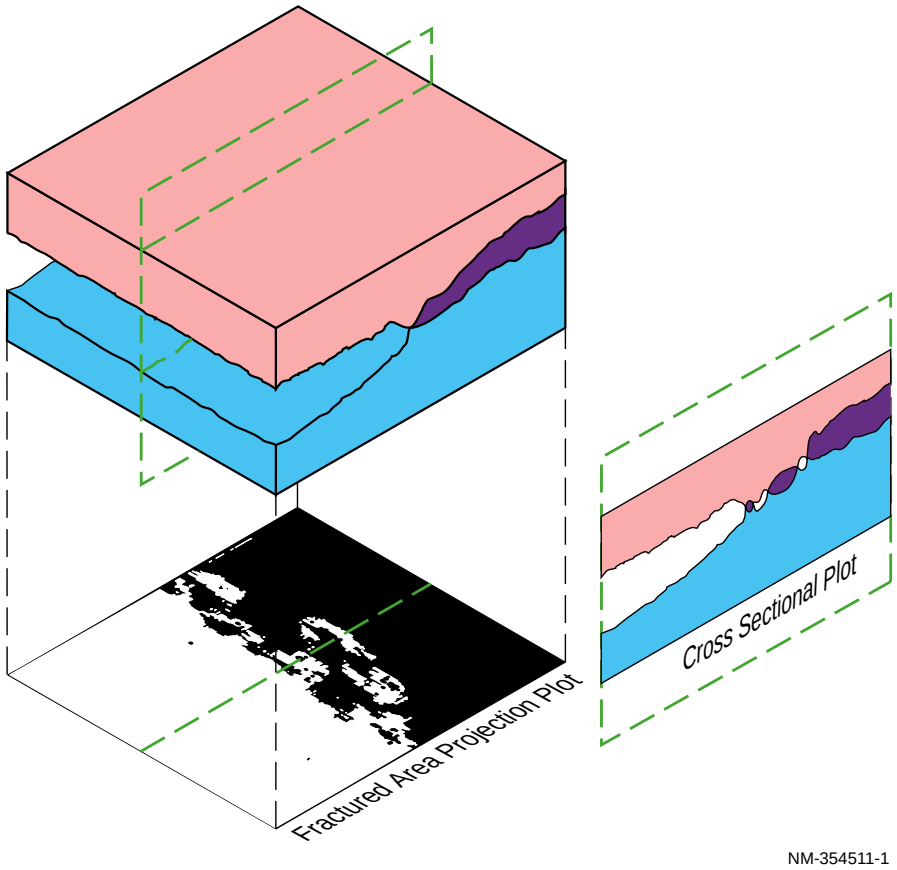

FIGURE 8. RECONSTRUCTION OF THE CRACK FRONT CONFIGURATION BY SUPERIMPOSING FRACTURE SURFACE TOPOGRAPHS.

When the topographs are displaced normal to the crack plane, the line of intersection moves and crack growth is simulated. Figure 9 is a series of plan projection views of the crack at increasing topograph displacements. The transition between the white area and black area is a zone, rather than a line, and results from our choice of a large elevation range to characterize a large area of fracture surface. Better crack front definition can be obtained if a smaller area with a concomitant smaller elevation range is selected. Nevertheless, an average crack front can be defined by calculating the percentage of white (fractured) area in a plot and dividing by the plot height, and an effective crack growth rate (with respect to topograph displacement) can be obtained by plotting the percent fractured area against topograph displacement. This curve may be thought of as a fracture progression curve (FPC), indicating the relative (to crack opening displacement) growth history of a crack.

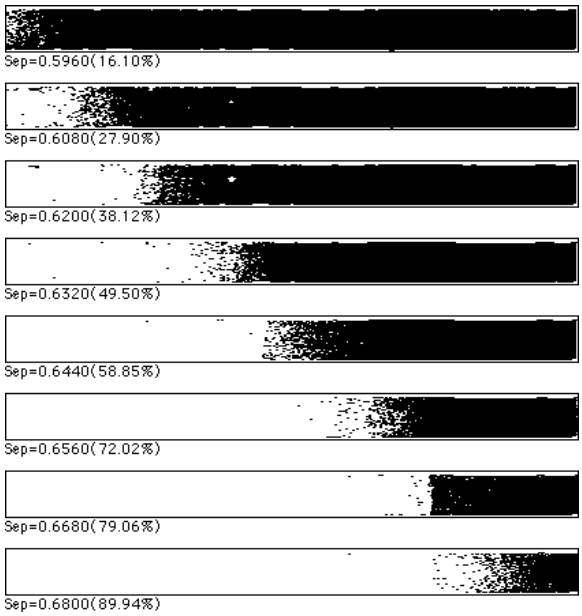

FIGURE 9. A SERIES OF PLAN VIEWS OF A CRACK FRONT AT INCREASING TOPOGRAPH DISPLACEMENTS. WHITE AREAS INDICATE SEPERATED MATERIAL; BLACK AREAS INDICATE INTACT MATERIAL

Results from the previous specimens showed that, under steady state fatigue loading, the area increase rate varies monotonically and the FPC is linear or a smoothly varying function without inflections. However, figure 10 shows that, when a change in environment is imposed (i.e., a change from vacuum to air back to vacuum), a deviation from the steady state slope is produced. The slopes for vacuum and air environments were measured to be 1.66%/μm** and 1.69%/μm in vacuum and air, respectively.

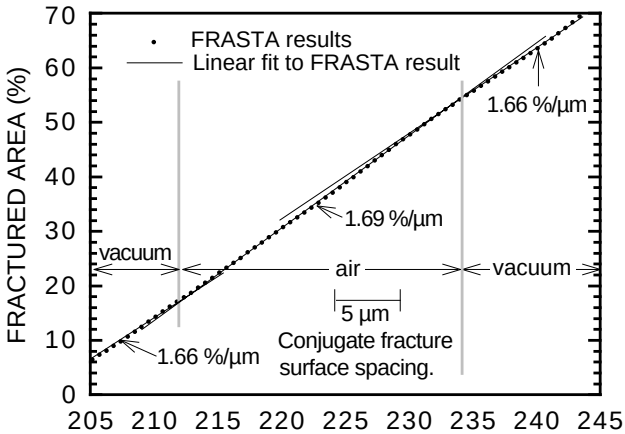

FIGURE 10. EFFECT OF ENVIRONMENT ON FRACTURE PROGRESSION CURVE (FPC).

**The unit %/μm refers to the percent of fractured area increase (assessed from the plan projection views) per unit increase in the conjugate fracture surface map spacing.

2.5 DISCUSSION.

These results show that certain parameters of the cyclic load spectrum and environment may be obtainable from the fracture surfaces of a broken component. Additional investigations are required to confirm the observations and refine the procedures. If relationships can be established between fracture surface topography, crack growth characteristics, and load/environment parameters, fracture surfaces will be of much greater value in analyzing damage and failures in fixed wing and rotary wing aircraft as well as in other structures subjected to cyclic loads. If relationships between elevation features and microstructure can be established, materials development efforts will be assisted.

Fundamental to success is a fast, accurate, high-resolution method for characterizing fracture surface topography. This prerequisite is fulfilled by software-automated stereoscopy and COSLM. Also necessary are three-dimensional analyses of the topography data; the Fourier technique and the FRASTA technique provide promising results.

Passoja and Psioda[12] were the first to apply Fourier analysis to fracture surfaces. Using a one-dimensional transform, they determined the spatial frequency spectra of the roughness profile revealed on a cross section. McSwain[13,14] applied Fourier analysis to in-plane features of fracture surfaces. By calculating the two-dimensional power spectrum of a digitized SEM micrograph of a fatigue surface, McSwain demonstrated that striation spacing could be determined quickly and accurately, even in cases where visual assessment was difficult or impossible. McSwain further showed that Fourier analysis could classify and quantitatively characterize fracture surface patterns and distinguish among ductile rupture, cleavage, fatigue, and intergranular failure.

The results reported here suggest a greatly extended role of Fourier analysis to quantitative assessment of load and environment parameters. Application of a Fourier algorithm to three-dimensional fracture surface topography data produced EPSD curves that were sensitive to load parameters and environment, and fatigue surfaces produced under equivalent conditions produced nearly identical EPSD curves. This raises the exciting prospect of determining the load and environment conditions that caused service failure by comparing EPSD curves from the field failure with EPSD curves from specimens fatigued under known conditions in laboratory tests.

From the FRASTA examination, the slope in the FPC is a sensitive indication of the plasticity associated with crack propagation. An increase in the slope (i.e., more crack extension per unit fracture surface map separation) reflects a decline in the crack tip plasticity required for crack extension. Thus, the high slope shown in figure 10 indicates that crack growth in an air environment requires less crack tip plasticity than required under vacuum.

At least two explanations for this effect are apparent. If the crack tip plasticity is significantly rate dependent, reduced crack tip plasticity would be expected at high crack growth rates. Under this scenario, environment controls crack growth rate by a mechanism not directly related to crack tip plasticity. The reduced crack tip plasticity in air is a consequence (not a cause) of the faster crack growth.

An alternative explanation is that the environment directly influences the total amount of plasticity at the crack tip. The hydrogen embrittlement mechanisms could explain the trend toward reduced crack tip plasticity in air whether hydrogen causes embrittlement or localizes the plasticity for fracture by the so called hydrogen induced localized plasticity (HELP) mechanism. The HELP mechanism reduces the total crack tip plasticity by localizing it near the fracture surface. FRASTA results are clearly sensitive to the total crack tip plasticity, although it is unclear whether FRASTA can characterize the distribution of plasticity beneath a fracture surface. The Fourier analysis might be offering some clarification. The results in figure 7 show that the elevation power spectral density at short wavelengths is greater for the fatigue fracture surface formed in air, which means that, on average, the air environment produces a more severely changing fracture surface topography. Thus, in air, the crack tip plasticity near the fatigue fracture surface varies substantially on a fine scale, which suggests that air enhances the localized plasticity, in keeping with the HELP mechanism.

Regardless of the precise mechanism of environmental enhancement of fatigue cracking, FRASTA is shown to distinguish between the topographies of fracture surfaces formed in different environments and, therefore, has the potential to describe how the plasticity associated with fatigue crack propagation is influenced by environment.

2.6 SUMMARY.

- Keys to extracting fracture surface topography information are a fast and accurate method for three-dimensional analysis of the fracture surfaces.

- Fourier analyses of fracture surfaces may provide the basis for a library of reference curves useful in determining the load spectrum and environment conditions that caused a service failure.

- Fourier analyses of fracture surfaces from cyclically loaded 2024-T3 aluminum fatigue crack growth specimens can detect variations in load and environmental conditions that are not easily detected by conventional SEM examination.

- FRASTA can distinguish between fracture surfaces formed in air and under vacuum in cyclically loaded 2024-T3 aluminum. Results suggest that an air environment reduces the total crack tip plasticity (compared with a vacuum environment).

3. CORRELATION OF FRACTURE SURFACE TOPOGRAPHY WITH FATIGUE LOAD HISTORY.

3.1 BACKGROUND.

Corrosion-fatigue crack growth rates in structural components are determined by material properties, load history, and environment history. Therefore, to predict the kinetics of corrosion-fatigue crack growth, we need a knowledge of load and environment conditions. Accurate information about load and environment history for field failures is particularly difficult to obtain because conditions change substantially over time and distance. Estimates of far field conditions are rarely adequate when analyzing failures that occur in structural features with complex geometries (e.g., the loads and environment in a fuselage skin lap splice). As a result, in many cases, the information required to analyze fractures must come from the immediate vicinity of the crack.

Qualitative fracture surface analysis can often provide the general mechanism responsible for fracture (e.g., ductile rupture, brittle fracture). Sometimes, a rough estimate of causative stresses can be associated with failure from this information. When fatigue striations can be seen, simple semiquantitative analyses of their spacing have been used to estimate crack extension per cycle under cyclic loads.[3,4] The stresses responsible for crack growth are obtained from such analyses by relating crack growth rate to ΔK with the Paris equation,[5] although this approach has pitfalls.[8]

Recently, instrumentation to rapidly map fracture surface topography has enabled the practical application of more quantitative analyses. FRASTA (fracture surface topography analysis) is a conjugate fracture surface matching procedure that can often detect and quantify the effect of variations in material properties, loading conditions, and environmental conditions on fatigue and fracture processes. In the present study, FRASTA and finite element simulations were used to estimate the magnitude of overloads applied during fatigue crack propagation.[15] Results indicate that FRASTA is effective in quantifying the local stress histories that influence crack propagation rates.

3.2 EXPERIMENTAL PROCEDURE.

To produce fracture surfaces for topographic analysis, we performed a fatigue experiment on a 75-mm-wide, center-cracked, panel specimen of 1-mm-thick 2024-T3 aluminum sheet typical of that used for aircraft fuselage skin. A sinusoidal load was applied to the specimen so that the crack was propagated several millimeters at a maximum stress intensity (K_{max}) of about 11 MPa$\sqrt{m}$, an R (= K_{min} / K_{max}) of 0.6, and a frequency of 5 Hz. At 2- to 5-mm intervals, cyclic loading was stopped at K_{min}, and an overload was applied for about 30 seconds. After each overload, the load level was reduced to K_{min} and cyclic loading was continued until the next overload, or ultimately, until the specimen failed.

After specimen failure, elevation maps of selected areas of the conjugate fracture surfaces were made using the FRASTAscope, a system consisting of a confocal optics scanning laser microscope (COSLM); a precision, computer-controlled x-y-z stage, and computer programs to control data acquisition, manipulation, and display. FRASTA entails quantifying the topographies of conjugate fracture surfaces, inverting one topograph and aligning it with respect to the other (so that the two topographs are in the same relative position as the fracture surfaces were when the surfaces separated in the fatigue test) and then examining the matches and mismatches between the topographs at various relative displacements (shown schematically in figure 8). A more detailed description of FRASTA is given by Kobayashi and Shockey in references 10 and 11.

3.3 EXPERIMENTAL RESULTS.

The positions of the overloads, as a function of half crack length, are shown by data points corresponding to the left ordinate of figure 11. The figure compares K_{max} during the cyclic loading intervals with K_{max} imposed by the overload. The small variations in K_{max} during the cyclic loading are a consequence of small amounts of crack growth under intervals of constant load cycling. Fatigue crack propagation could not be reinitiated at 11 MPa√m after the overload to 25.5 MPa√m, so higher stress intensity levels (17 and 14 MPa√m) were used to restart fatigue crack growth.

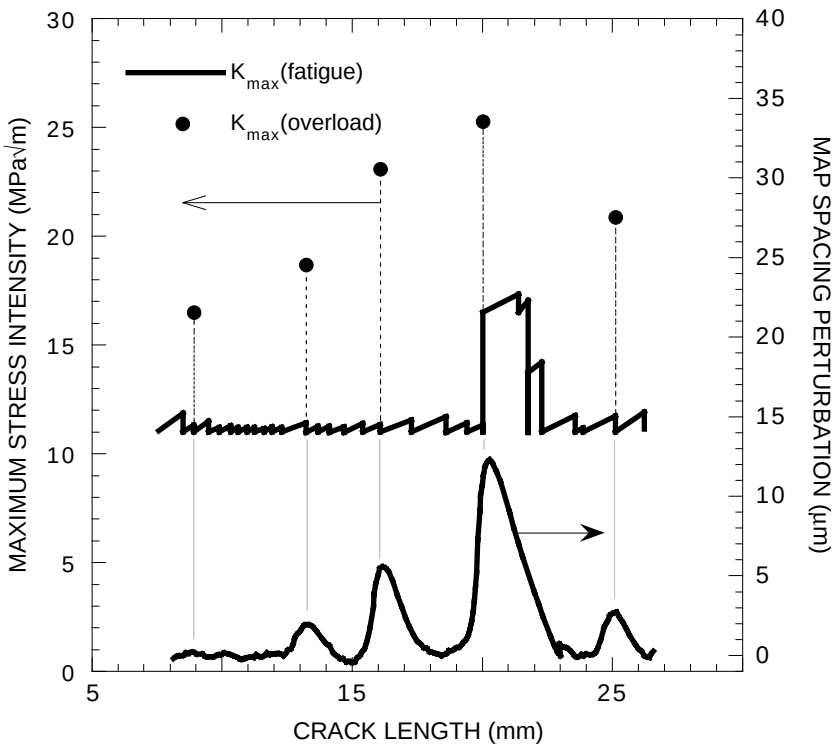

FIGURE 11. COMPARISON OF OVERLOAD HISTORY TO PERTURBATIONS IN FRACTURE PROGRESSION CURVE (FPC).

FRASTA results were obtained from topographs from a 0.58-mm-thick strip centered on the midplane of the specimen thickness. Figure 8 shows schematically a plan projection view of the crack at a fixed topograph displacement (i.e., a fractured area projection plot). The crack propagation history was deduced by incrementally displacing the topographs normal to the crack plane so that the line of intersection moves and crack growth is simulated. An average crack front can be defined by calculating the percentage of white (fractured) area in a plot and dividing by the plot height, and an effective crack growth rate (with respect to topograph displacement) can be obtained by plotting the percent fractured area against topograph displacement. This curve may be thought of as a fracture progression curve (FPC) indicating the relative (to crack opening displacement) growth history of a crack.

Results from experimental data[16] have shown that, for constant fatigue loading and environmental conditions, the FPC increases without inflections or perturbations. However, the FPC for the present experiment shows distinct perturbations that are a result of the overloads imposed during fatigue crack propagation, as shown in figure 12. By subtracting the expected FPC for fatigue crack without overloads (i.e., a baseline FPC), we can estimate the position, shape, and magnitude of the perturbations resulting from the overloads (see the data points corresponding to the right ordinate of figure 11). The process of selecting a baseline FPC has not yet been formalized; however, a reasonable estimate was obtained by inspection.

Figure 12 shows that overloads above 16.5 MPa√m produce a perturbation from the steady-state slope. The FPC slope initially decreases, then increases, and then returns to the baseline slope. The positions of the peaks in the perturbations correspond to the crack lengths at which the overloads were applied. These deviations begin before the overload is applied, as shown in figure 11.

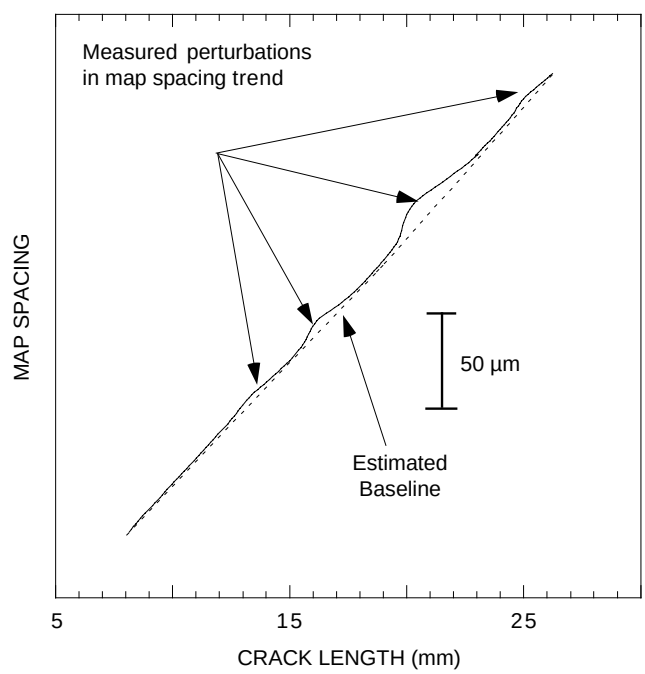

FIGURE 12. FRACTURE PROGRESSION CURVE (FPC) WITH BASELINE.

3.4 FINITE ELEMENT SIMULATIONS.

The FRANC2D code[17] was used to compute the plastic displacements near a crack tip as a function of load. FRANC2D provides a relatively convenient interactive platform for two-dimensional crack propagation simulations and, most important, it can simulate elastic-plastic material response. This ability is crucial for computing the residual crack tip opening (i.e., the crack tip opening after unloading) and relating it to FRASTA results.

Finite element method simulations of the crack tip response require appropriate constitutive models that describe the nonelastic deformation behavior. Figure 13 compares the cyclic stress-strain response with the monotonic stress-strain response at low strain levels. These results show substantial cyclic strain hardening. The results in figure 13 formed the basis of the constitutive equations used in the finite element method (FEM) calculations described in section 3.5.

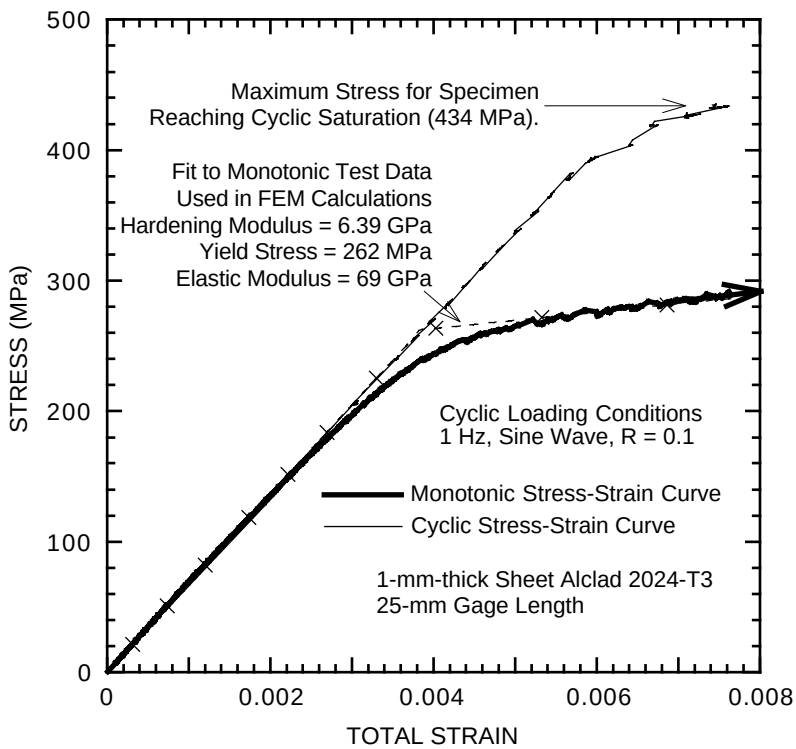

FIGURE 13. MONOTONIC AND CYCLIC STRESS-STRAIN BEHAVIOR OF 2024-T3 ALUMINUM ALLOY.

The simulations used a half-space, two-dimensional, plane-stress mesh with dimensions consistent with the center cracked panel used in the crack growth experiments (see figure 14). An initial set of simulations was performed to determine the size of the plastic zone created by the maximum fatigue load and the distribution of plastic strains within the plastic zone. The monotonic stress-strain curve in figure 13 was used for these simulations. The distribution of plastic strain in the plastic zone was estimated from the maximum stress levels reached in the plastic zone. The corresponding strain levels were obtained using the monotonic stress-strain curve in figure 13.

The influence of cyclic strain hardening in the plastic zone ahead of the crack tip before overloading was included in some of the simulations by elevating the local yield stresses within the plastic zone to levels consistent with the strain levels computed in the initial set of simulations described above. The amount of increase in the yield stress was determined by the strain level at the maximum fatigue load and the corresponding stress from the cyclic stress-strain curve. As the crack propagates, the tip of the crack leaves material formerly in the plastic zone in its wake. These regions were also cyclically hardened as shown in figure 15.

The effect of an overload on crack tip shape was determined by loading the model with a cyclically hardened crack tip region to the overload stress and unloading. The maximum residual displacement of the fracture surfaces from the overload ($\delta_{overload}$) was measured from these simulations. Figure 16 shows the computed crack tip geometries. The maximum residual displacement of the fracture surfaces from the fatigue load ($\delta_{fatigue}$) was determined in a similar manner except that the maximum fatigue load was applied. The difference in residual displacements ($\delta_{overload} - \delta_{fatigue}$) was computed over a range of overload conditions and compared with the perturbations in the FPC obtained from FRASTA.

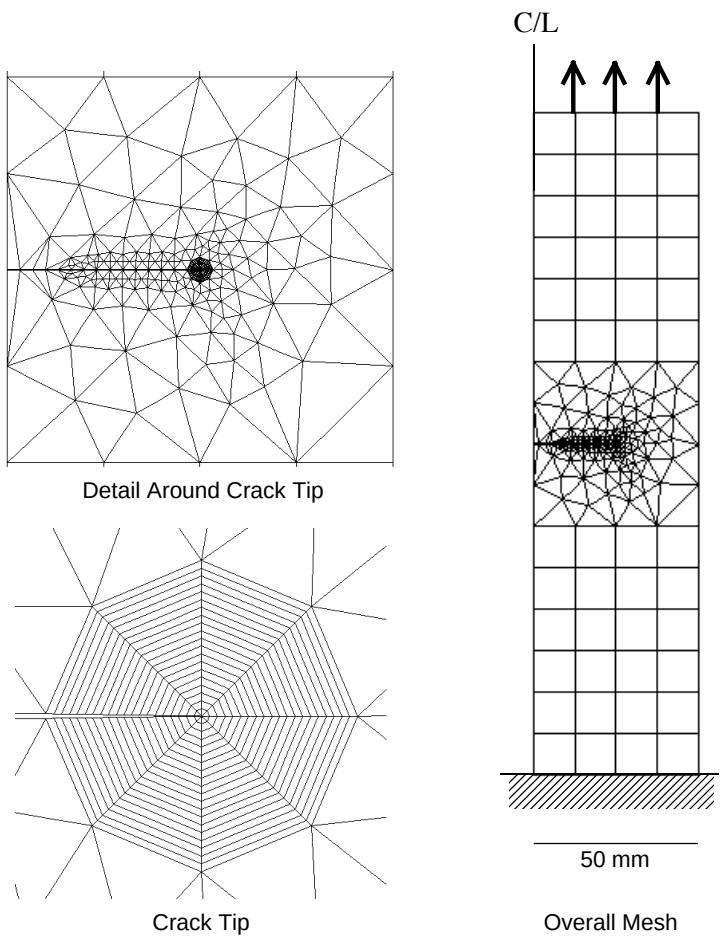

FIGURE 14. FINITE ELEMENT MESH AROUND CRACK TIP IN CENTER-CRACKED PANEL SPECIMEN.

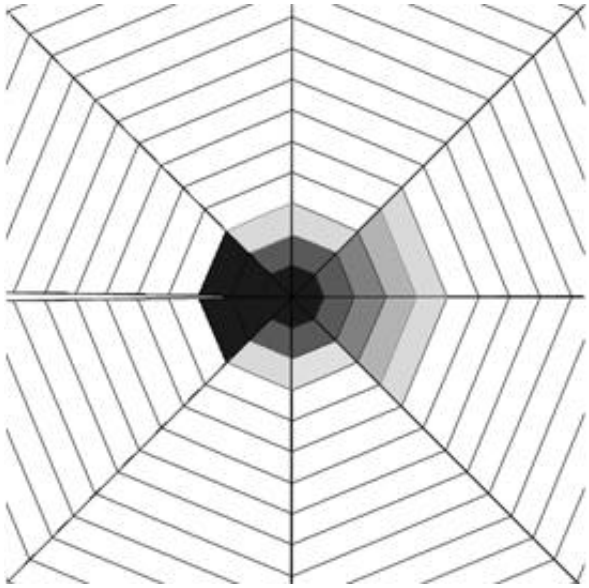

Elastic Modulus = 710 GPa
ν = 0.33
Hardening Modulus = 6.4 GPa

Cell Designation	Cyclically Hardened Yield Stress (MPa) Partially Hardened	Fully Hardened
□	262	262
▒	290	379
▓	317	434
▓	335	434
▓	359	434
■	372	434

0.2 mm

FIGURE 15. CYCLICALLY HARDENED AREAS NEAR CRACK TIP.

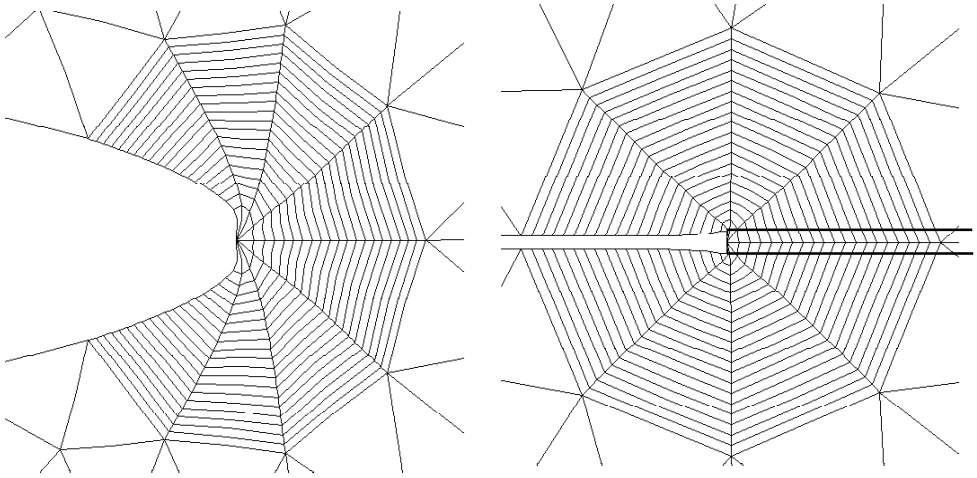

Loaded to K = 11 MPa√m.

Loaded to K = 11 MPa√m
and unloaded.

Displacements magnified 100 times.

FIGURE 16. COMPUTED CRACK TIP GEOMETRIES.

3.5 DISCUSSION.

The magnitude and location of perturbations in the FPC show considerable promise for characterizing overloads that occur during fatigue crack propagation. The magnitude of the FPC perturbations increased with increasing overload, and the location on the fracture surface of the perturbation peaks correlated closely with the crack length at which the overload was applied (see figure 11). The consistency and sensitivity of the perturbations suggest that an analysis of FPC perturbations provides a way to characterize overloads imposed during crack growth. Fracture surface analysis techniques have been used to determine J_{IC} from the dimensions of the stretch zone created by the nucleation of ductile crack growth and measured by SEM.[18] The present analysis demonstrates that overloads below J_{IC} can be quantified from fracture surface topography analysis.

The FEM calculations of FPC perturbations based on residual crack tip displacements exhibit a dependence on overload stress intensity that is similar in magnitude to FRASTA measurements (see figure 8); however, the differences are significant. The perturbations determined from FEM simulations did not exhibit an overload stress intensity threshold. Instead, they showed a monotonically increasing perturbation height with increasing overload stress intensity. Simulations of the overload threshold were attempted (unsuccessfully) by assuming that the threshold was determined by cyclic strain hardening at the crack tip. To estimate the maximum effect of cyclic hardening on crack tip geometry, simulations were performed with the entire crack tip plastic zone produced by the fatigue load (about 0.56 mm in diameter) hardened to the maximum exhibited by the cyclic stress-strain curve (434 MPa as shown in figure 13). The pattern of cyclic hardening used for these simulations is shown in figure 15. The size of the plastic zone, r_p, determined from the FEM simulations was in good agreement with an estimate obtained from the following equation by Irwin.[19]

$$2r_p = \frac{1}{\pi}\left(\frac{K}{\sigma_{ys}}\right)^2 \qquad (1)$$

Alternative simulations were performed to determine the effect of overloads on crack tip geometry with the crack tip plastic zone partially cyclically hardened. The appropriate levels of partial cyclic hardening were determined from a simulation of the plastic strain levels achieved in a simulation of the unhardened crack tip response. In that simulation, loading and unloading was applied in accord with the maximum cyclic load used in the experiments (K_{max} = 11 MPa$\sqrt{m}$). Modeling partial hardening of the plastic zone recognizes that much of the crack tip plastic zone experiences small cyclic plastic strains that will produce less than the maximum cyclic hardening level shown in the experimental data in figure 13 (i.e., the cyclically hardened yield stress will be less than 434 MPa). Figure 15 shows the pattern of cyclic hardening used in the simulation with a partially hardened crack tip.

The simulated FPC perturbation height is reduced when the level of cyclic hardening of the crack tip plastic zone is increased. However, even the simulation with a fully cyclically hardened crack tip did not produce a threshold in the stress intensity dependence of perturbation height, nor were the simulation results within the estimated uncertainty of the measured results (see figure 17). Although the simulated perturbation heights are close to the measured results, agreement might be improved if the crack tip plastic zone was cyclically hardened to higher levels. Justification for such an approach is not currently apparent and will require more direct determination of the extent of crack tip plastic zone cyclic hardening.

Uncertainties in the FRASTA measurements also come from different placements of the baseline shown in figure 12. Baselines were selected by connecting regions of the FPC that lie between the perturbations with a smoothly varying curve. At present, an unequivocal method of fitting the baseline has not been established. Variations in the perturbation heights produced by baseline fits that appear reasonable to the authors produced the variations in the perturbation height shown by the error bars in figure 17.

The computational procedure and the interpretation of computational results must be refined to more accurately predict the effect of overloads on fracture surface topography. Nevertheless, when the measurement and computational difficulties created by the small magnitude (≤ 10 μm) of fracture surface topography perturbations are considered, the present computational results show remarkable agreement with the measurements of fracture surface topography.

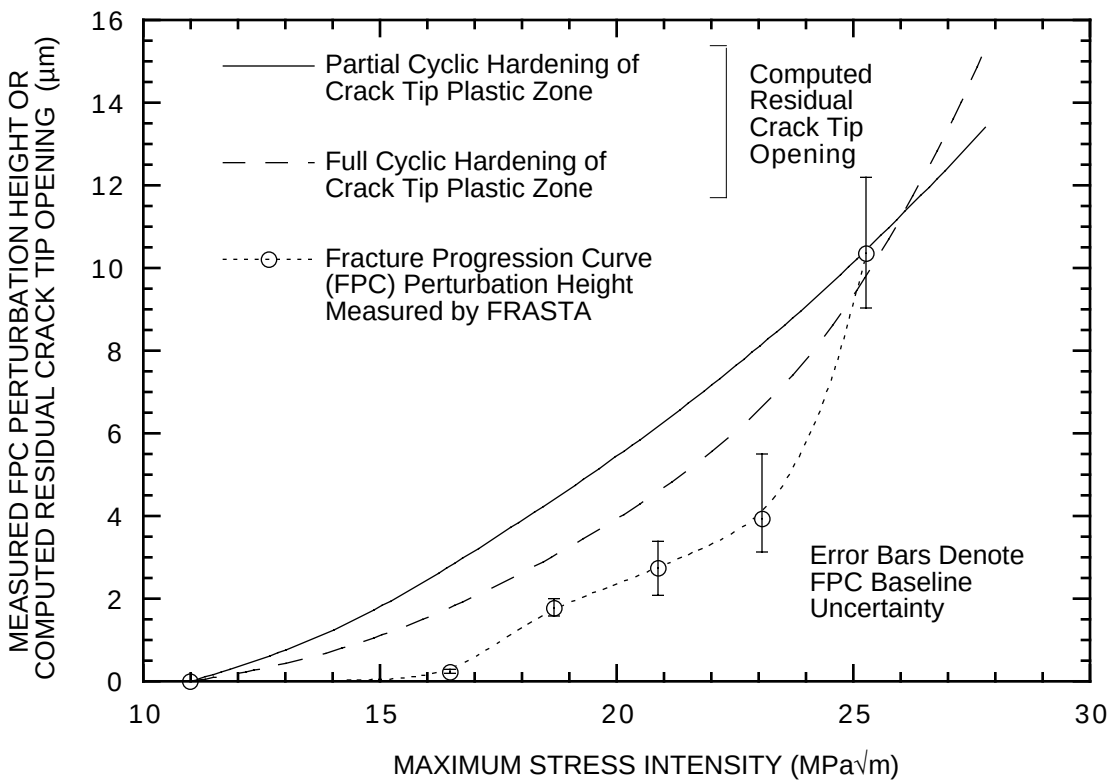

FIGURE 17. COMPARISON OF COMPUTED AND MEASURED FPC PERTURBATION HEIGHTS RESULTING FROM OVERLOADS.

3.6 SUMMARY.

- FRASTA was shown to be an effective method for measuring the magnitude and location of perturbations in fracture surface topography created by overloads applied during fatigue crack propagation in 2024-T3 aluminum alloy.
- The location and magnitude of fracture surface perturbations from overloads were closely correlated with the overload magnitude and fatigue crack length at the time of the overload. This finding indicates that FRASTA can be effective in quantifying variations in local stress histories that influence crack propagation rates.
- Experimental results exhibit an apparent overload threshold that must be exceeded to produce topographic fatigue fracture surface perturbations.
- Finite element simulations of the unloaded crack tip shape created by overloads were in reasonable agreement with measured results. Differences were only partially explained by uncertainties in measurement consistency and in the extent of cyclic hardening of the crack tip plastic zone.

4. DETAILED FRACTURE SURFACE ANALYSIS OF THE EARLY STAGES OF A CORROSION FATIGUE CRACK.

To analyze the early stages of corrosion fatigue cracking in clad 2024-T3 aluminum alloy, we performed a step-by-step characterization of early crack growth by fracture surface topography analysis (FRASTA). Results from the analysis show the location and sequence of events in the early stages of crack formation, the crack front structure and position evolution, and the crack propagation directions. These results describe the changing nature of crack propagation in the early stages of crack growth, which provides a framework for a physically based predictive capability.

4.1 EXPERIMENTAL PROCEDURES.

A tapered tensile coupon was cut from Section 360 (above the windows) of a Boeing 737 aircraft that had been retired from service in 1992 after 56,228 flight hours. The skin consisted of a 0.81-mm-thick (0.032-in.) core of 2024-T3 aluminum alloy, clad layers on both sides that were about 0.06 mm thick (0.002 in.), a paint layer on the outer surface about 0.08 mm thick (0.003 in.), and a corrosion inhibitor layer on the inside that was about 0.10 mm thick (0.004 in.), as sketched in figure 18. Microhardness tests showed that the core and the clad had Vickers hardnesses of 120.4 ± 1.5 and 32.2 ± 2.3 kg/mm^2, respectively.

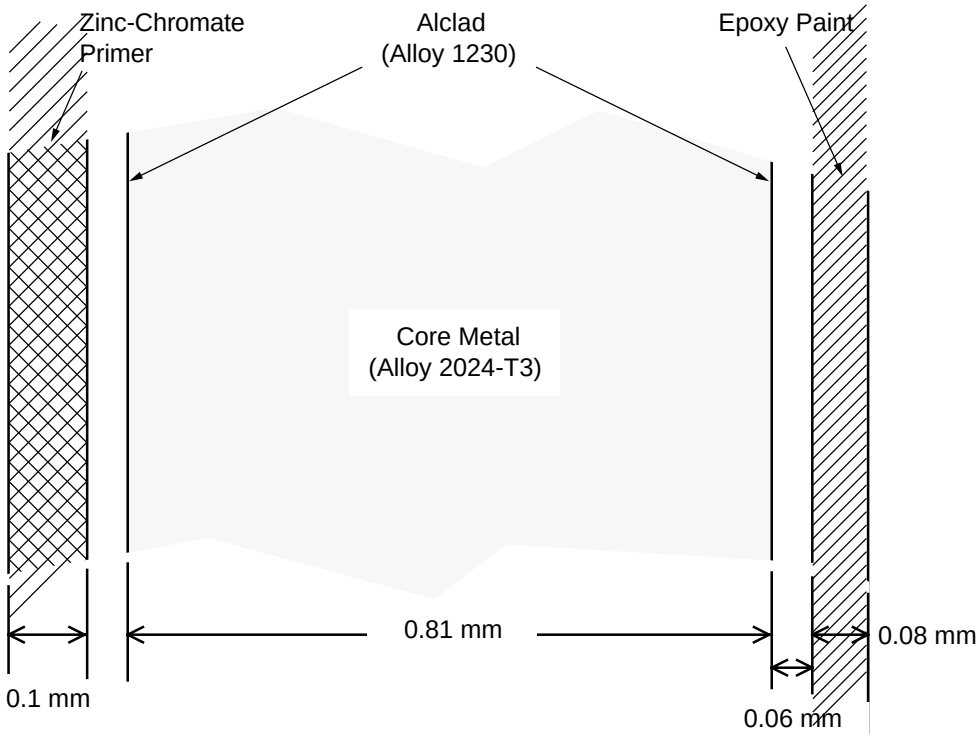

FIGURE 18. CROSS SECTION OF REPRESENTATIVE AIRCRAFT SKIN.

The specimen was fatigue loaded at 5 Hz with a sinusoidal waveform to a maximum stress of 276 MPa and an R value (the ratio of minimum to maximum stress in a fatigue cycle) of 0.1. The

specimen was pretreated by soaking in a stagnant, 0.5 M NaCl aerated solution for 3 days before mechanical loading. Fatigue testing of the specimen was done in air. Failure occurred after 75,460 cycles.

Figure 19 shows a scanning electron microscope (SEM) photograph of one of the two fracture surfaces. Crack nucleation occurred at the lower left corner. Figure 20 shows higher-magnification photographs of the conjugate surfaces in the vicinity of crack nucleation. The fracture surfaces in the clad are smooth and crystallographic. The markings on the surface of the 2024-T3 core material indicate the crack propagation directions. The photograph of the corner area in Figure 20 shows a corrosion pit at the outer edge near the corner and two inadvertently damaged areas on Surface B that occurred after the test. These damaged areas do not reflect microfailure activity during the fracture process and must be omitted in analyzing the fracture surface topography.

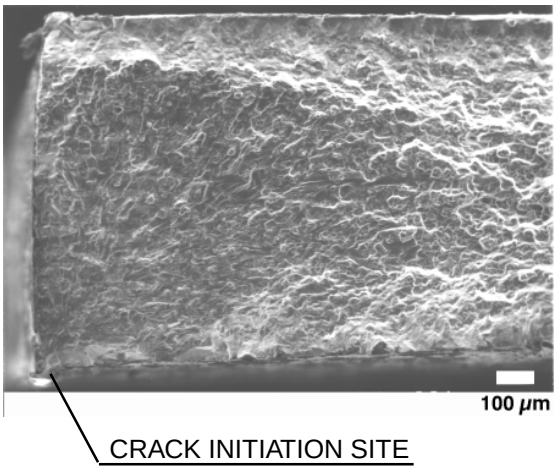

FIGURE 19. SEM MICROGRAPH OF FRACTURE SURFACE SHOWING AREA WHERE CRACK INITIATED.

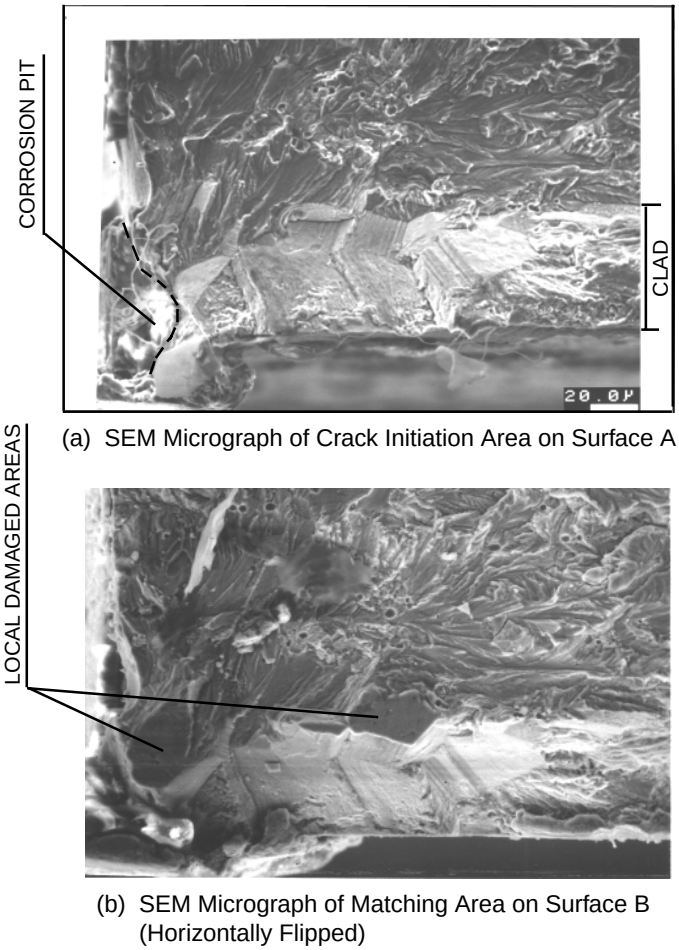

(a) SEM Micrograph of Crack Initiation Area on Surface A

(b) SEM Micrograph of Matching Area on Surface B (Horizontally Flipped)

FIGURE 20. CONJUGATE SURFACES OF THE CRACK INITIATION AREA.

4.2 FRACTURE SURFACE TOPOGRAPHY ANALYSIS (FRASTA).

We attempted to reconstruct the corrosion fatigue cracking process by applying the FRASTA technique to the two conjugate fracture surfaces. A description of the confocal optics scanning laser microscope (COSLM) used to measure the topography of fracture surfaces is given in Section 2.2 and a description of the FRASTA technique is given in Section 2.4 and references 10 and 11.

Figure 21 shows the contrast and gray-scale topography images obtained from the COSLM. The images for Surface B have been horizontally inverted to facilitate comparison of the fracture surface features. When the conjugate surface topography profiles are superimposed, aligned, and viewed at different displacements, gaps between the topographic surfaces exist at some areas and overlapping occurs at other areas. These areas are identified and differentiated in FAPPs (Fractured Area Projection Plots), which are like x-radiographs of the specimen looking normal to the nominal crack plane. Figure 22 shows FAPPs for a series of topograph displacements. The white areas are gaps between the topographs and represent separated material in the specimen. The black areas are areas where the topographs overlap and indicate unbroken material.

The series of FAPPS in figure 23 shows the effect of increasing the topograph displacement and, hence, approximates the effect of increasing tensile strain. The progress of the corrosion fatigue failure is indicated by the evolution of the white areas. Below a separation of 0.635, the white areas change very little. The separation is measured in arbitrary units used for comparison between different locations along the fracture surface. At the spacing of 0.640, a wedge-shaped white area begins to form next to the corrosion pit. As shown in figure 20(b), this is the exact spot where extraneous damage was found on Surface B; thus, we cannot conclude that the crack nucleated here. Clear microcrack formation is indicated at a separation of 0.645, where a triangular crack appears adjacent to the pit. Later spread of the crack through the adjacent grain is apparent at spacings of 0.650 and 0.655. The crack then spreads in the cladding.

Somewhat later, the failure propagates into the core aluminum alloy (see FAPP at spacing of 0.660). Although the FAPPs do not show a sharp crack front (the diffuseness of the crack front zone is attributed to noise in the topographic data taken by the confocal laser microscope), the movement of the crack front in FAPPs agrees well with the markings on the fracture surfaces. By the spacing of 0.670, a major segment of the crack front is in the core material, and the later FAPPs show the movement of the crack in the core material.

By superimposing the FAPPs on the SEM photograph of the fracture surfaces, we can identify fracture surface and microstructure features associated with microfracture nucleation, microfailure growth paths, and late-breaking ligaments. The resulting plots in figure 23 suggest microstructural sites where the microcracks were formed and indicate how crack growth occurred. The locations of isolated microcracks relate well with the grain boundaries and triple points [see figures 23(b) and 23(c)]; thus, we speculate that the grain boundaries and triple points are preferred sites for microfailure nucleation.

FAPPs also provide the relative crack propagation rate when the amount of white area in each FAPP in a series is plotted versus topograph displacement. Figure 24 provides such a plot from the information in figure 22. Above a spacing of 0.677, the crack attains a constant growth rate and, as can be seen in figure 22, an apparent steady state thumbnail shape. When the crack has reached this (relatively large) size and

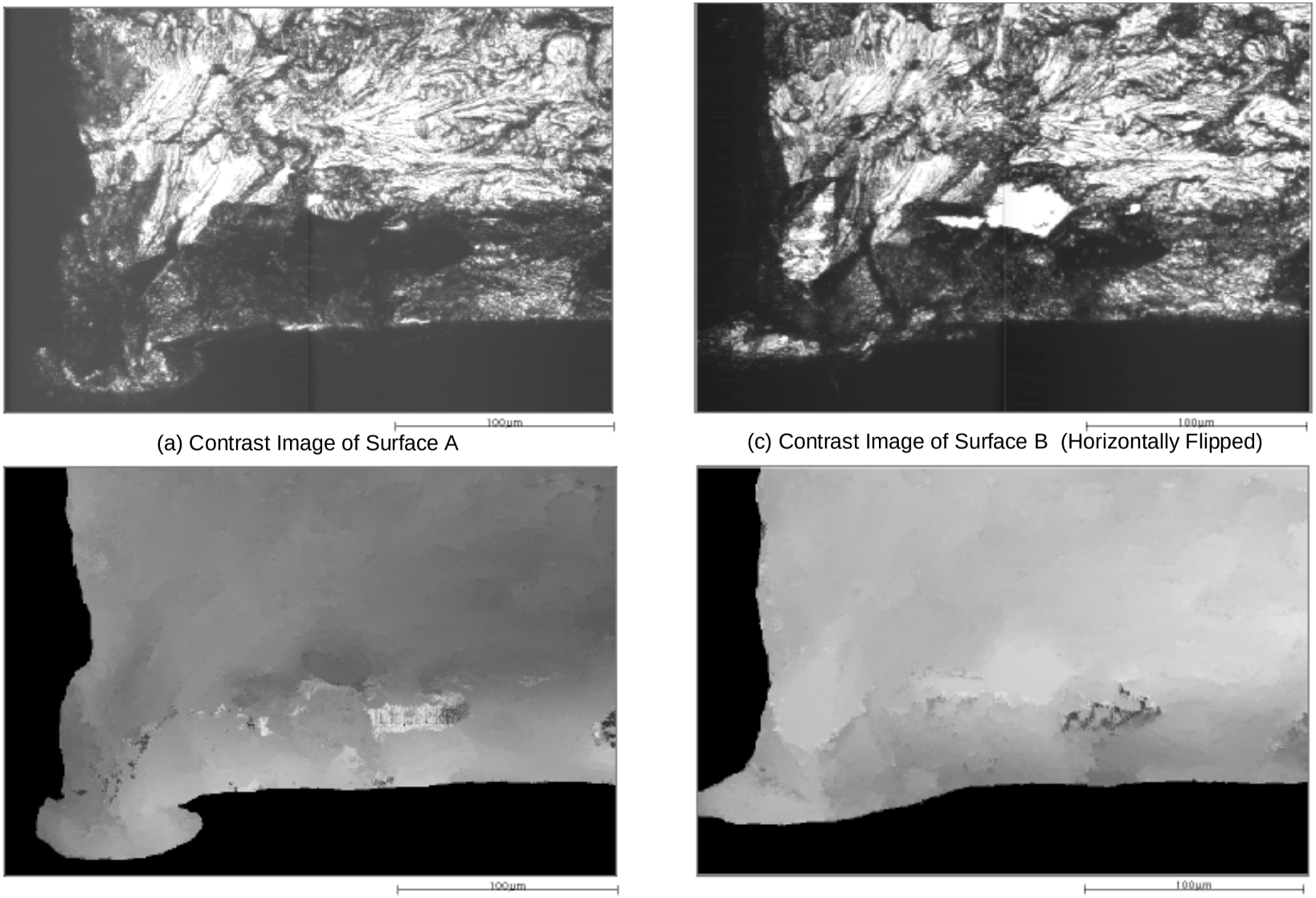

(a) Contrast Image of Surface A

(c) Contrast Image of Surface B (Horizontally Flipped)

(b) Gray-scale Topography Image of Surface A

(d) Gray-scale Topography Image of Surface B (Horizontally Flipped)

FIGURE 21. CONTRAST AND GRAY-SCALE TOPOGRAPHY IMAGES OF CONJUGATE SURFACES OF THE CRACK INITIATION SITE. (IMAGES OF SURFACE B WERE HORIZONTALLY FLIPPED TO SHOW THE CORRESPONDENCE BETWEEN THE CONJUGATE SURFACES.)

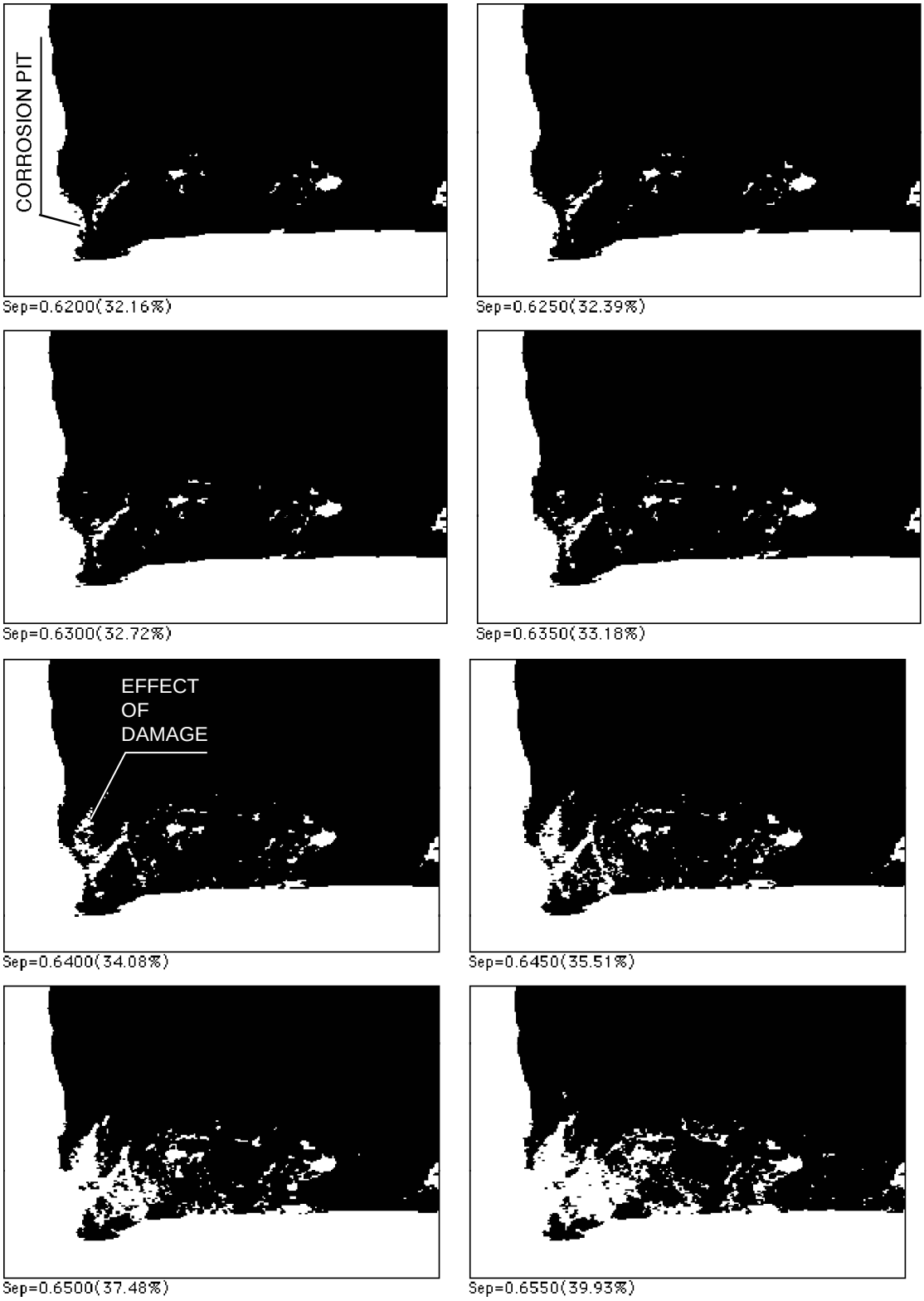

FIGURE 22. A SERIES OF FAPPS PRODUCED BY FRASTA SHOWING CRACK FORMATION AND GROWTH PROCESS (CONTINUED).

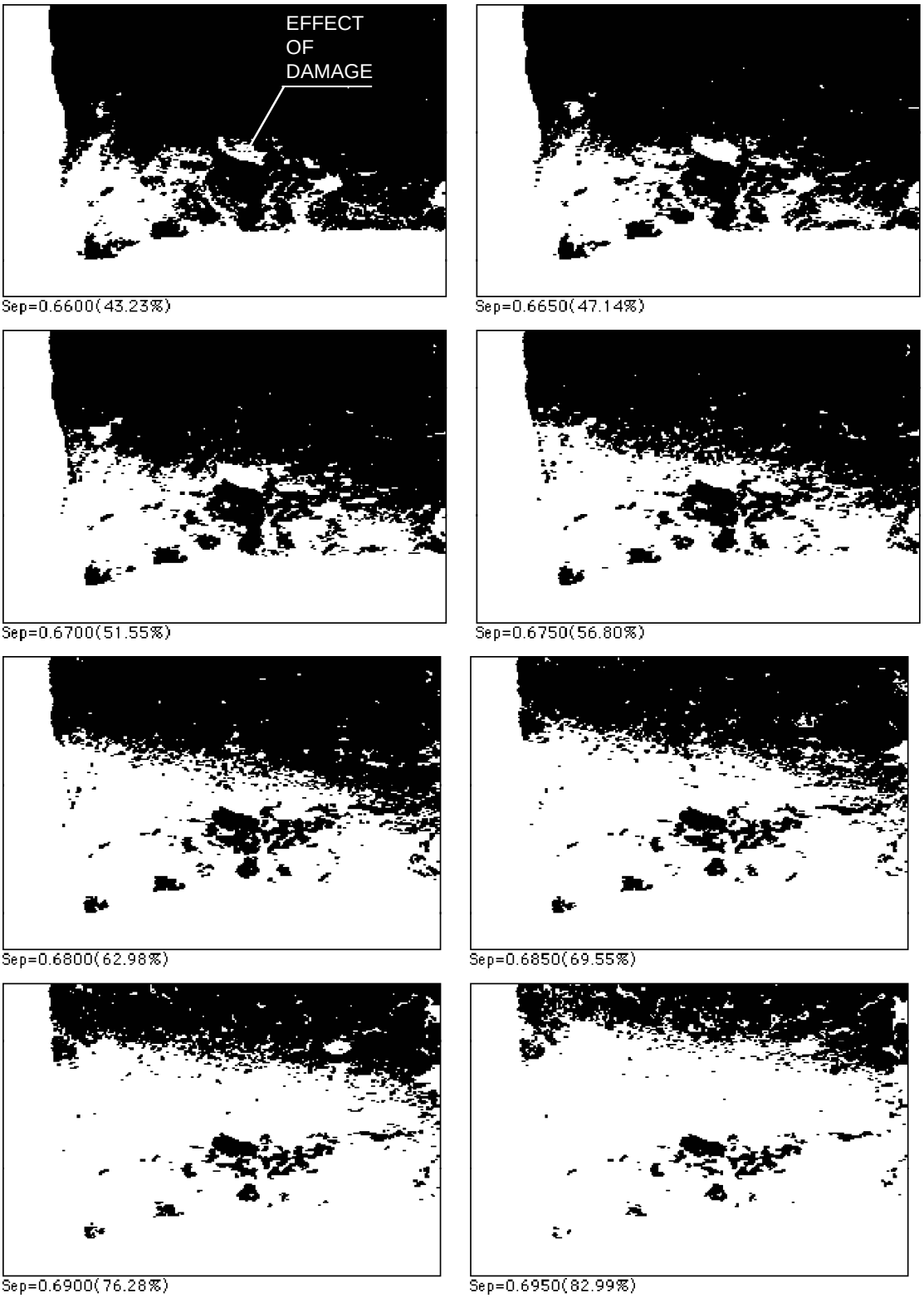

FIGURE 22. A SERIES OF FAPPS PRODUCED BY FRASTA SHOWING CRACK FORMATION AND GROWTH PROCESS (CONCLUDED).

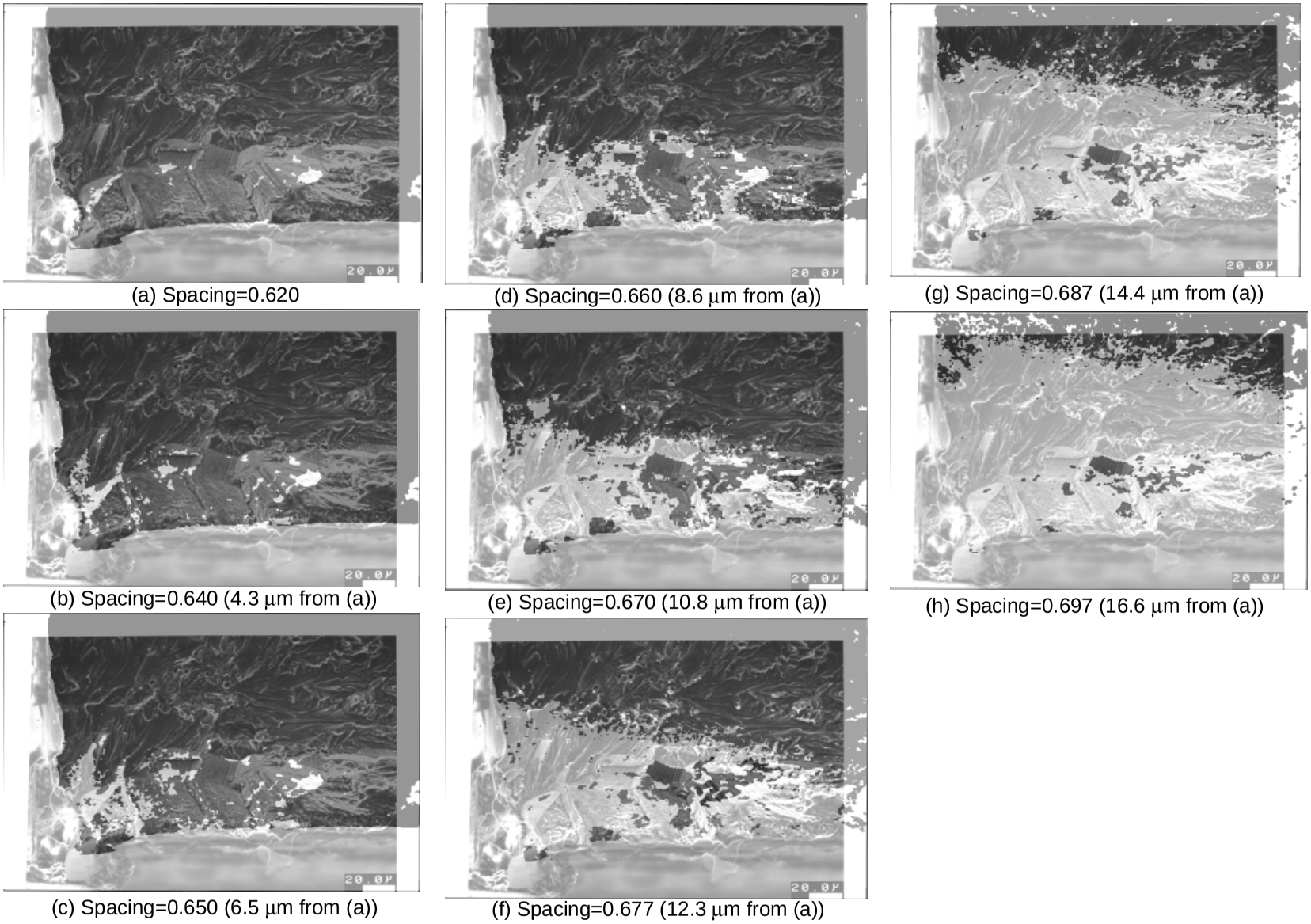

(a) Spacing=0.620

(b) Spacing=0.640 (4.3 μm from (a))

(c) Spacing=0.650 (6.5 μm from (a))

(d) Spacing=0.660 (8.6 μm from (a))

(e) Spacing=0.670 (10.8 μm from (a))

(f) Spacing=0.677 (12.3 μm from (a))

(g) Spacing=0.687 (14.4 μm from (a))

(h) Spacing=0.697 (16.6 μm from (a))

FIGURE 23. SUPERPOSITION OF FAPPS ON SEM MICROGRAPH RELATING FRACTURE PROCESSES TO MICROSTRUCTURAL FEATURES.

(mature, thumbnail) shape, its behavior may be describable by fracture mechanics equations. Below 0.677 to a spacing of about 0.628, the growth rate is nonlinear, suggesting the transition from local microcrack formation, growth, and coalescence to become a long crack that is possibly describable by the Paris law. Below a spacing of 0.628, the rate of increase in separated area is much lower; however, these states may not be realistic because they are created by overclosing of the spacing between conjugate surfaces. These results suggest that the plot of fractured area increases as a function of conjugate surface spacing may provide a means to define the boundary between an engineering crack whose behavior can be described by fracture mechanics and a small crack where continuum fracture mechanics may not apply.

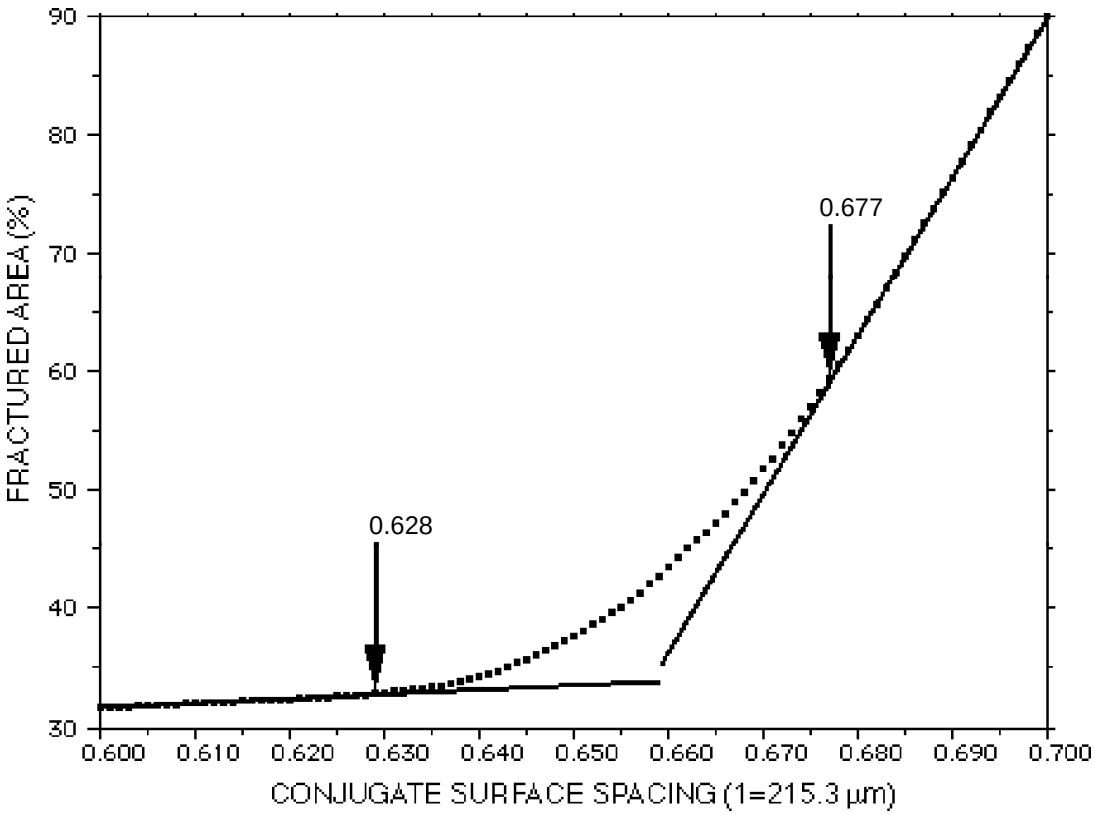

FIGURE 24. FRACTURED AREA INCREASE RATE AS A FUNCTION OF CONJUGATE SURFACE SPACING. CRACK FORMATION PERIOD IS BETWEEN THE SPACING OF 0.628 AND 0.677. BEYOND THE SPACING OF 0.677, FATIGUE CRACK GROWTH APPEARS TO BE DOMINANT.

Cross-sectional views of topograph pairs show the out-of-plane path of the crack, the crack front profile, and the crack tip opening displacement and angle. Figures 25 and 26 provide cross-sectional views along lines A-A and B-B, respectively. Figure 25 shows that the crack propagates through the clad at roughly 30 degrees to the tensile axis and that, in this initial phase of growth, the crack surfaces are quite smooth. Such observations are consistent with Stage I fatigue.[20] After reaching the core material, the crack path changes to be normal to the nominal tensile direction and the crack tip remains sharp and constant. (The large spikes near the position of the interface between the cladding and the core alloy are probably artifacts caused by noise in the elevation data due to lack of reflected light at that particular spot.)

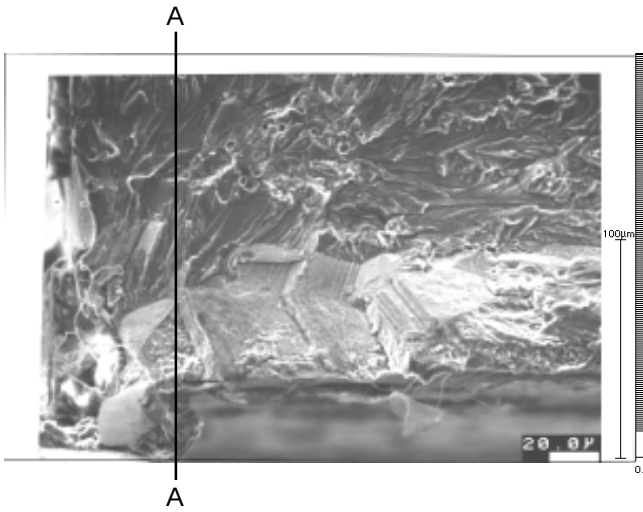

(a) SEM Micrograph Showing the Line of Sectioning.

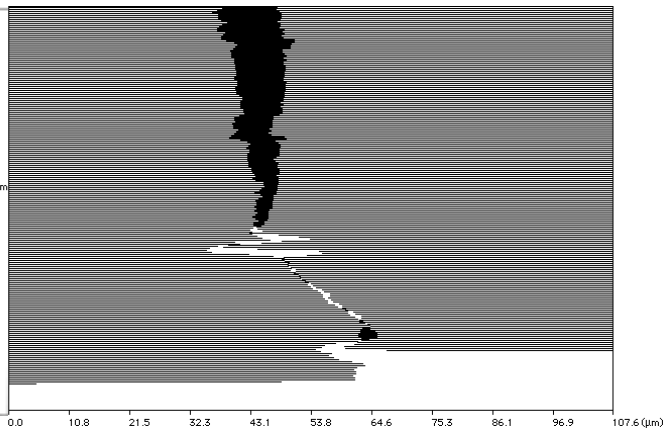

(b) XSP at Spacing=0.650

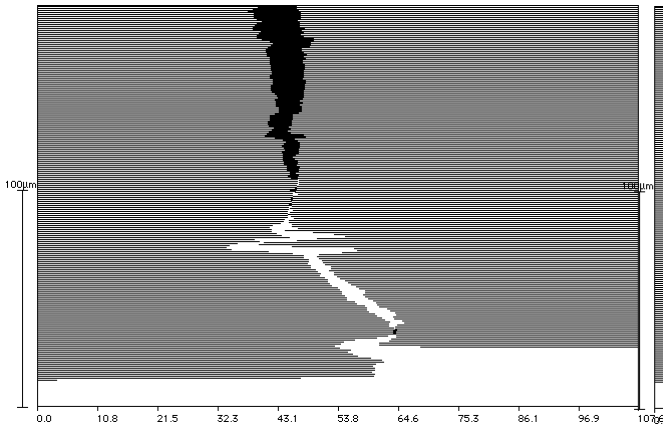

(c) XSP at Spacing=0.663

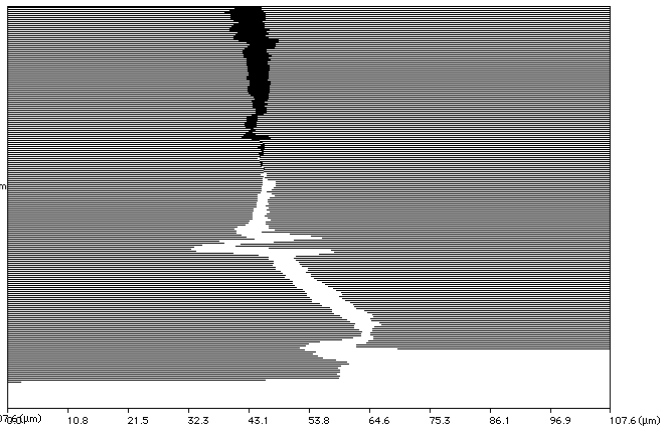

(d) XSP at Spacing=0.673

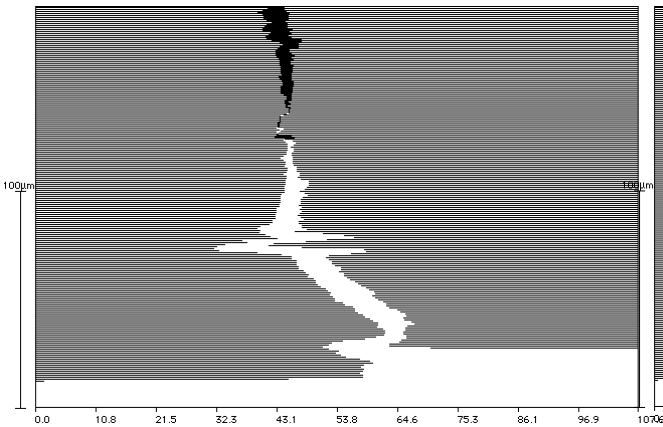

(e) XSP at Spacing=0.681

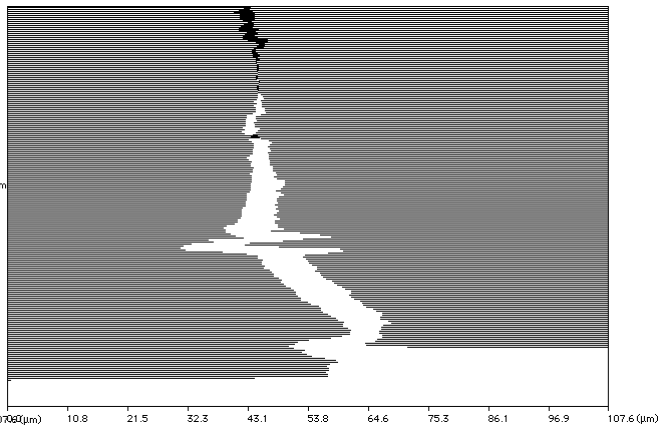

(f) XSP at Spacing=0.690

FIGURE 25. A SERIES OF XSPS MADE ALONG THE LINE A-A IN THE THICKNESS DIRECTION. CRACK TIP MOVEMENT SEEMS TO BE STEPWISE WITH A NEARLY FIXED CRACK TIP OPENING DISPLACEMENT.

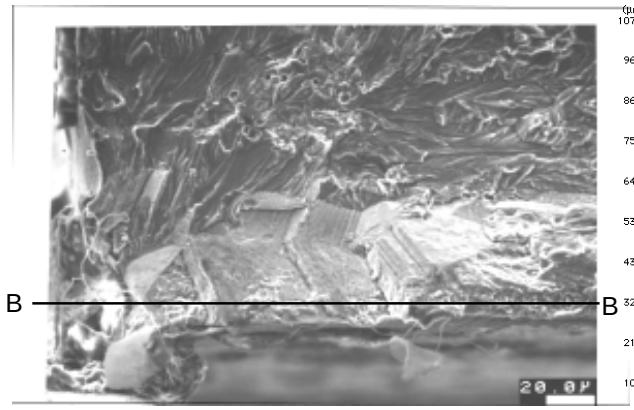

(a) SEM Micrograph Showing the Line of Sectioning.

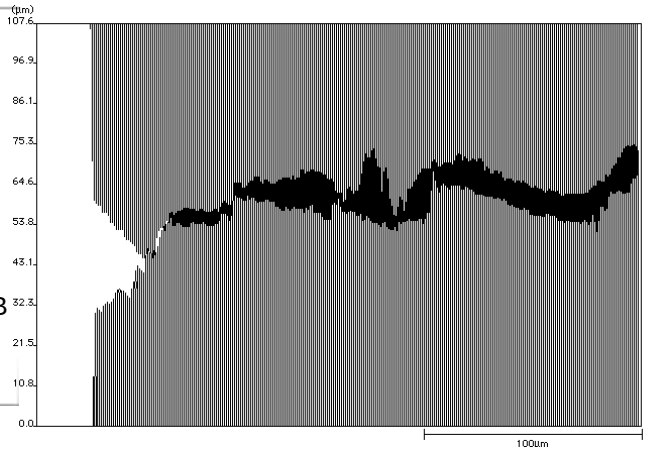

(b) XSP at Spacing=0.628

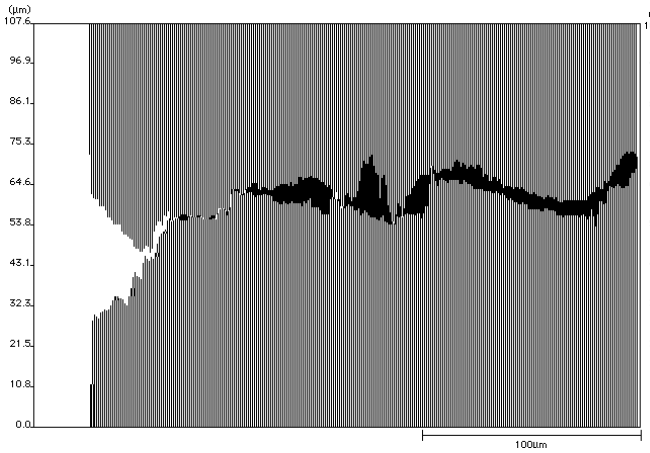

(c) XSP at Spacing=0.644

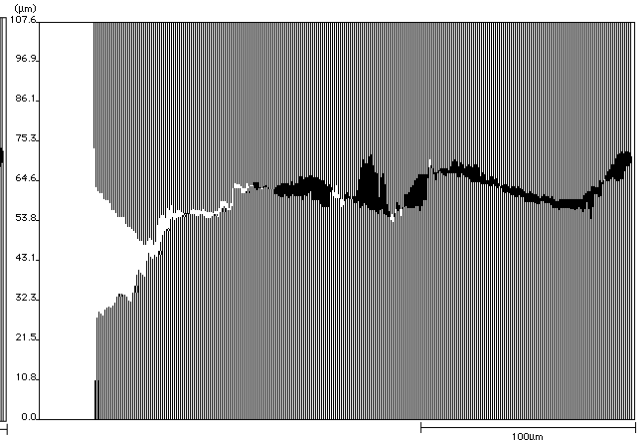

(d) XSP at Spacing=0.650

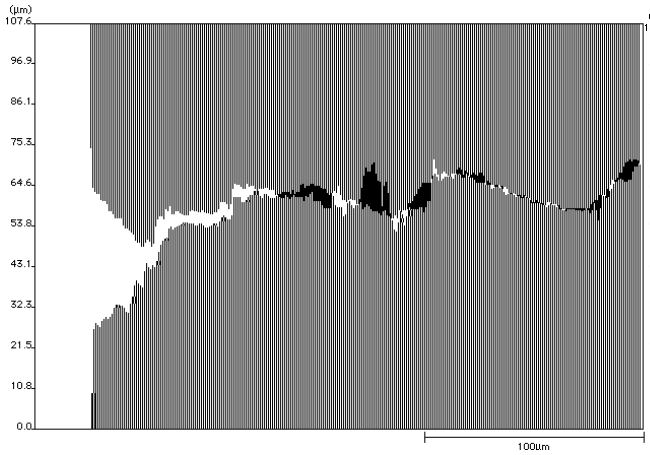

(e) XSP at Spacing=0.661

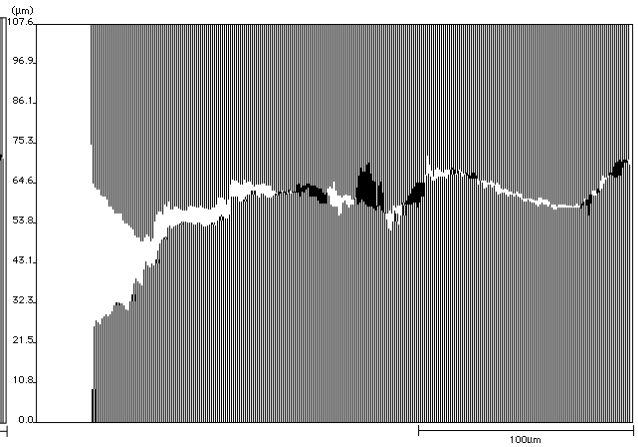

(f) XSP at Spacing=0.666

FIGURE 26. A SERIES OF XSPS MADE ALONG THE LINE B-B THAT IS PARALLEL TO THE EXTERIOR SURFACE OF THE PLATE.

Figure 25 also shows that crack extension in the core alloy is incremental as indicated by the crack front movement from (c) to (d), (d) to (e), and (e) to (f). Furthermore, the crack tip opening displacement to cause this incremental growth was about 1.94 μm (= incremental spacing of 0.009 times 215.3 μm). Using this value as the critical crack tip opening displacement, we can calculate the stress intensity factor as follows

$$K = \sqrt{\frac{d\sigma_o E}{1-\nu^2}} \qquad (2)$$

where d is the crack tip opening displacement, σ_o is the flow stress (440 MPa), E is the modulus of elasticity (72.4 GPa), and ν is Poisson's ratio. We obtain a value of 8.2 MPa√m, which is a reasonable value for the stress intensity factor for fatigue crack growth.

The cross section in figure 26, which is parallel to the clad interface and perpendicular to the cross section in figure 25, shows the crack opening profiles at different areas in the clad at different times. The profile suggests a conical pit at the specimen surface and the emergence of a crack from the pit on a plane lying at 45 degrees to the tensile axis. The persistence of black areas in the growing white field suggests local tough spots that elongated more than other areas.

4.3 DISCUSSION.

The FRASTA results provide insight into a frequently asked question: When does a small local crack become an engineering crack whose behavior can be described by fracture mechanics? Our experience with many applications of FRASTA is that the plot of fractured area versus conjugate surface spacing (figure 24) is sensitive to changes in testing conditions and environment during fracturing. Slope changes in this plot thus appear to provide an objective criterion for this boundary. However, its validity should be confirmed by examining additional samples.

Detailed microfracture process information was obtained and microfailure was related with microstructure. We could observe the grain-by-grain progress of the failure process. This detailed microfailure information can be used in various ways. For example, the FRASTA results pinpoint the problem spots in the structure, and these spots can be examined by analytical chemistry methods such as x-ray energy dispersive spectroscopy or surface analysis by laser ionization (SALI) to identify what chemical elements were associated with early microcracking.

Furthermore, detailed microfracture information can be used to develop microstructure-based computational fracture models that can evaluate the effect of changes in material properties and microstructural parameters (such as grain boundaries).

Finally, the quantitative information on deformation that FRASTA generates provides a unique method to assess local and average toughness. Additional study will develop these capabilities and lead to other interpretive methodologies.

4.4 SUMMARY.

- Analysis of the topographies of conjugate corrosion fatigue failure surfaces showed the locations and sequence of microcrack nucleation, the crack front structure and position evolution, and the crack propagation directions in clad 2024-T3 aluminum aircraft skin.

- Grain boundaries and grain boundary triple points were indicated as preferred microstructural features for crack nucleation.

- Stage I fatigue fracture occurs initially in the cladding at 30-45 degrees to the tensile axis, producing smooth crystallographic failure surfaces perhaps influenced by hydrogen. The crack growth rate increases steadily as the initially rather diffuse crack front zone attains a steady-state shape, at which point the crack begins to grow at a constant rate.

5. FACTORS AFFECTING FATIGUE CRACK NUCLEATION.

Accurate assessment of the effects of environment, stress, and material condition on the early stages of corrosion-fatigue cracking requires an extensive investigation involving many variables. Early in this research program,[1] a broad-based evaluation was launched to assess the conditions that affect nucleation and early propagation kinetics of corrosion-fatigue cracks in clad 2024-T3. Detrimental effects of hydrogen were implicated in that investigation. The present investigation extends the previous one by examining the effects of environment, stress, and material condition (i.e., clad or bare 2024-T3 aluminum sheet) on the corrosion-fatigue crack nucleation characteristics.

5.1 EXPERIMENTAL PROCEDURES.

Corrosion-fatigue tests were conducted in four environments (vacuum, laboratory air, 0.5 M NaCl solution, and 0.5 M NaCl + 0.13 M As_2O_3) using tensile coupons that were machined from commercially available clad 2024-T3 sheet and bare 2024-T3 sheet. The clad sheet material simulates the thickness and material condition of material commonly used for commercial aircraft skin. It consisted of a core of 2024-T3 aluminum alloy that was about 0.88 mm thick and clad layers on both sides that were about 0.06 mm thick. Arsenic additions were made to the salt water solutions in some tests in an effort to enhance hydrogen effects on material behavior (i.e., promote hydrogen embrittlement). Arsenic retards the formation of diatomic hydrogen, which can enhance hydrogen uptake into the metal matrix. Tensile coupons used the full thickness of the sheet material (about 1.0 mm for the clad and bare materials), with a reduced section width and length of 7 mm and 25 mm, respectively.

Specimens were fatigue loaded with a sinusoidal waveform and an R value (the ratio of minimum to maximum stress in a fatigue cycle) of 0.1. Test conditions for each experiment are listed in table 1. One of five maximum stress levels was chosen for each test (103 MPa, 138 MPa, 172 MPa, 207 MPa, or 255 MPa). Tests in aqueous solution environments were preceded by a soak in the test environment for approximately one day. The aqueous solutions were stagnant and open to the air throughout the presoak and fatigue tests. The vacuum tests were conducted at a pressure of approximately 10^{-6} torr. Fracture surfaces from specimens recovered from each experiment were examined with a scanning electron microscope.

5.2 RESULTS.

Figure 27 shows the effects of environment, stress, and material cladding on cycles to failure. The relative fatigue life was examined for each environment and material combination to evaluate the influence of these factors on corrosion fatigue life. For bare material, the fatigue life in salt water was a factor of 30 to 100 less than the life under vacuum. Tests in salt water with arsenic additions exhibited fatigue lives that were similar to those in pure salt water. A crossover was observed in

TABLE 1. CORROSION-FATIGUE TEST RESULTS

Test Number	Coating	Max Stress (MPa)	Environment	Frequency (Hz)	Cycles to Failure
B1	Clad	255	Air	10	95,928
B2	Clad	255	Vacuum	10	405,402+
C1	Bare	255	Air	10	69,891
B3	Clad	255	Vacuum	10	414,787+
B4	Clad	255	0.5 M NaCl	5	48,477
C2	Bare	255	Vacuum	5	544,478+
B5	Clad	255	0.5 M NaCl + 0.13 M As_2O_3	5	32,804
B6	Clad	207	Vacuum	15	1,026,405
C3	Bare	207	Vacuum	15	1,650,854
C4	Bare	255	Vacuum	10	645,519
B7	Clad	255	Air	10	128,205
C5	Bare	255	Air	10	202,362
C6	Bare	255	Air	10	163,866
B8	Clad	172	Vacuum	15	3,891,143
C7	Bare	172	Vacuum	15	12,554,739+
C8	Bare	255	0.5 M NaCl	5	31,098
C9	Bare	255	0.5 M NaCl + 0.13 M As_2O_3	5	26,282
C10	Bare	172	Air	15	772,535+
B9	Clad	207	Air	15	253,201
B10	Clad	172	Air	15	344,564
B11	Clad	138	Air	15	949,745
B12	Clad	172	0.5 M NaCl	5	120,649
B14	Clad	207	0.5 M NaCl	5	68,963
B15	Clad	103	Air	15	3,249,569+
C11	Bare	207	Air	5	380,934+
B16	Clad	207	0.5 M NaCl + 0.13 M As_2O_3	5	47,329
C12	Bare	207	Air	15,20	5,600,171+
B17	Clad	255	Air	10	127,495
C13	Bare	207	Vacuum	15	2,638,930
C14	Bare	255	Vacuum	10	499,773
B18	Clad	255	Vacuum	10	226,126
B19	Clad	207	Vacuum	10	718,130
C15	Bare	255	Air	10	464,894
C16	Bare	207	Air	15	7,214,982+
B-20	Clad	172	0.5 M NaCl + 0.13 M As_2O_3	5	133,278
B-21	Clad	138	0.5 M NaCl	5	128,459
B-22	Clad	138	0.5 M NaCl + 0.13 M As_2O_3	5	214,108
C-19	Bare	207	0.5 M NaCl	5	33,975
C-20	Bare	207	Air	15	15,894,008+
C-21	Bare	255	Air	15	225,145
C-22	Bare	255	Vacuum	15	390,147+
C-23	Bare	255	Vacuum	15	940,206+
C-24	Bare	255	Vacuum	15	716,658
C-25	Bare	207	Vacuum	15	1,462,691+
C-27	Bare	207	Vacuum	15	3,816,793

the trends of the stress dependence of fatigue life of bare material in air and under vacuum. The fatigue life in air was a factor of 3 less than the fatigue life under vacuum at a maximum fatigue stress of 255 MPa; however, at 207 MPa, the relative magnitudes of the fatigue life were reversed.

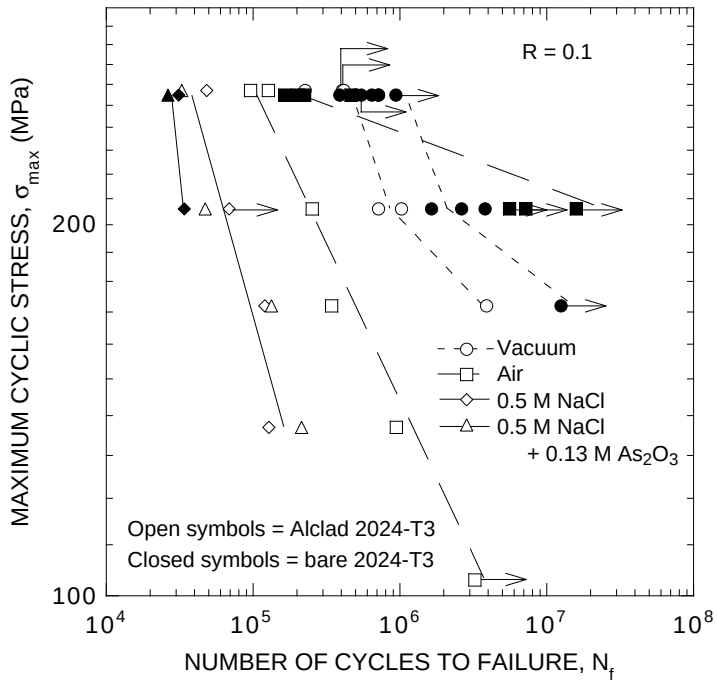

FIGURE 27. EFFECTS OF STRESS, CLADDING, AND ENVIRONMENT ON THE FATIGUE LIFE OF 2024-T3 ALUMINUM.

Clad material tested in salt water exhibited fatigue lives that were a factor of about 7 to 30 less than the fatigue lives under vacuum. Fatigue life in air was a factor of 2 to 10 less than the fatigue life under vacuum.

Comparing clad and bare materials in the same environment shows that the clad material exhibits a longer fatigue life in salt water and arsenated salt water than the bare material by a factor of about 2. In air and vacuum, the opposite trend was observed: the fatigue life of the clad material was shorter than that of the bare material by a factor of 2 to over 70 for the air environment and by a factor of 4 or more for the vacuum environment.

Examination of the fracture surfaces revealed that the nucleation site differed depending on the environment and the presence of material defects or inhomogeneities. Figures 28 through 32 show sections of the fracture surfaces near the crack nucleation sites for clad material tested under vacuum, in air, in 0.5 M NaCl, and in 0.5 M NaCl + 0.13 M As_2O_3. The failure nucleation sites for specimens tested under vacuum appear in the 2024-T3 core material near the corner of the fracture surface in most cases [see figure 28(a), (b), and (d)]. However, crack nucleation near the corner did not occur in Specimen B-18 where failure appears to have nucleated at a defect in or near the clad away from the specimen corner [see figure 28(c)]. This failure appears to have occurred prematurely because Specimen B-18 failed after less than half the number of cycles of other

specimens tested under the same conditions (compare the cycles to failure of Specimen B-18 with the cycles for Specimen B-2 and B-3 in figure 32).

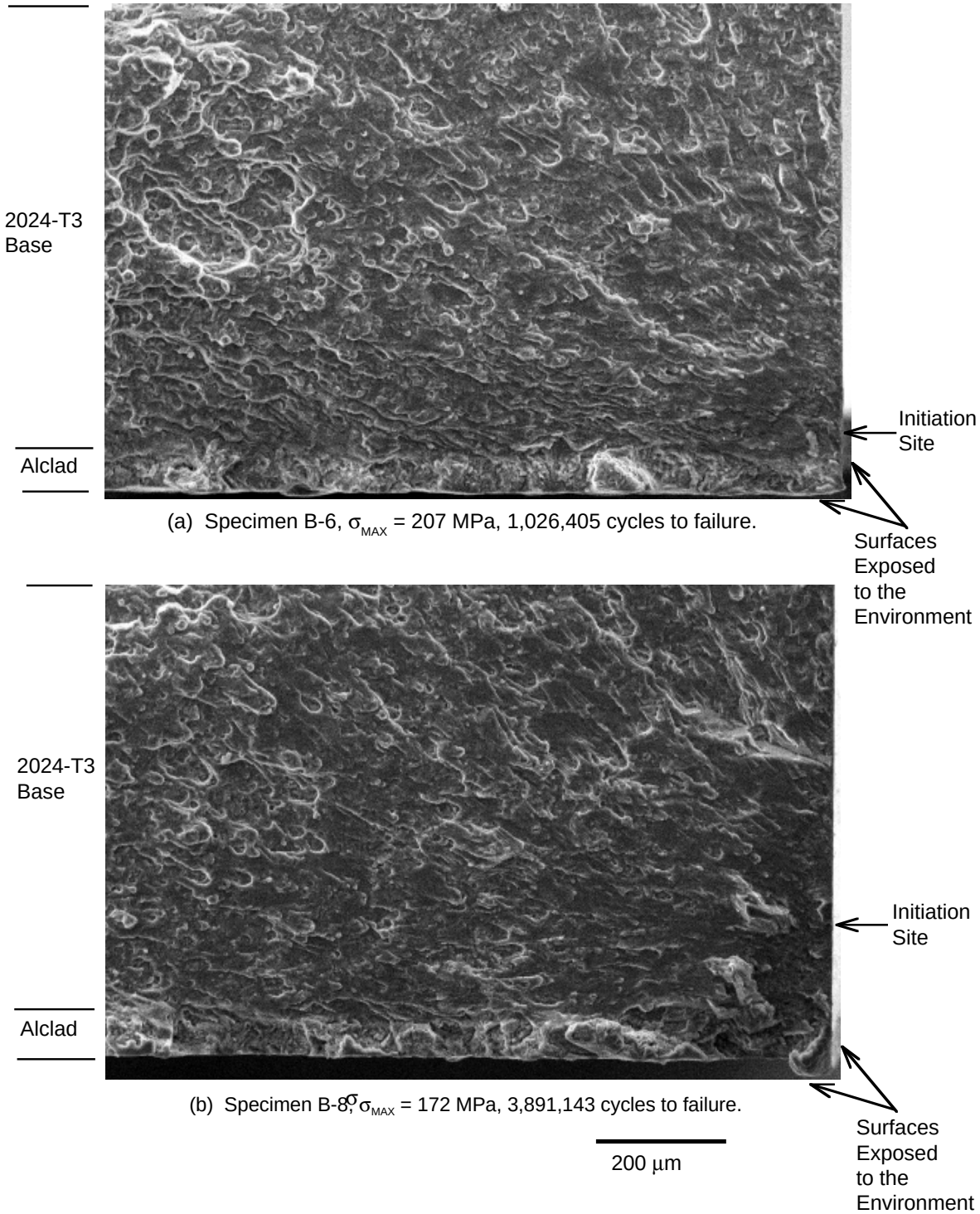

(a) Specimen B-6, σ_{MAX} = 207 MPa, 1,026,405 cycles to failure.

(b) Specimen B-8, σ_{MAX} = 172 MPa, 3,891,143 cycles to failure.

FIGURE 28. FRACTURE SURFACE APPEARANCE OF ALCLAD 2024-T3 FATIGUE SPECIMENS TESTED IN VACUUM.

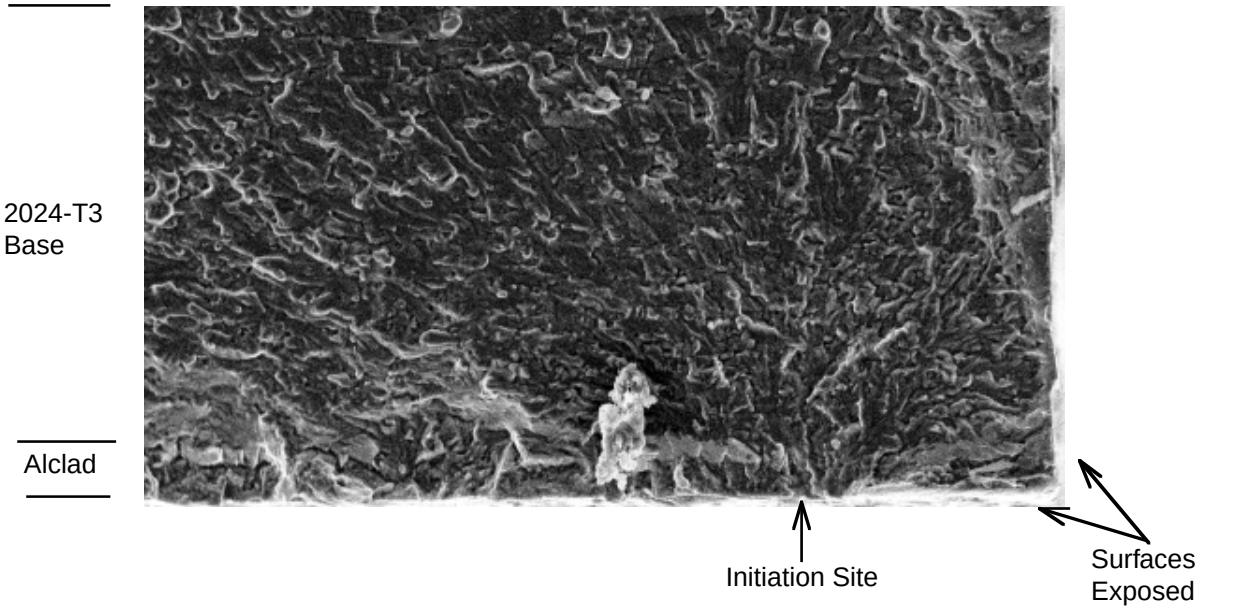

(c) Specimen B-18, σ_{MAX} = 255 MPa, 226,126 cycles to failure.

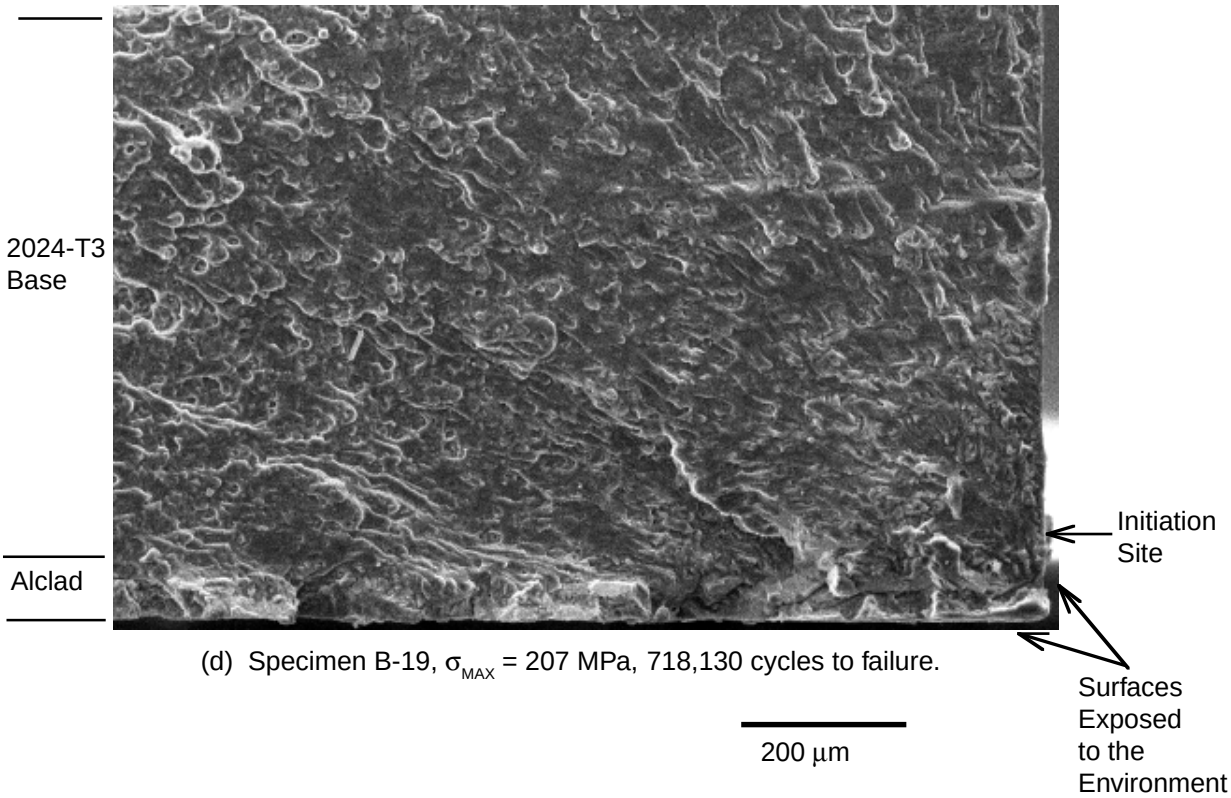

(d) Specimen B-19, σ_{MAX} = 207 MPa, 718,130 cycles to failure.

FIGURE 28. FRACTURE SURFACE APPEARANCE OF ALCLAD 2024-T3 FATIGUE SPECIMENS TESTED IN VACUUM. (CONCLUDED)

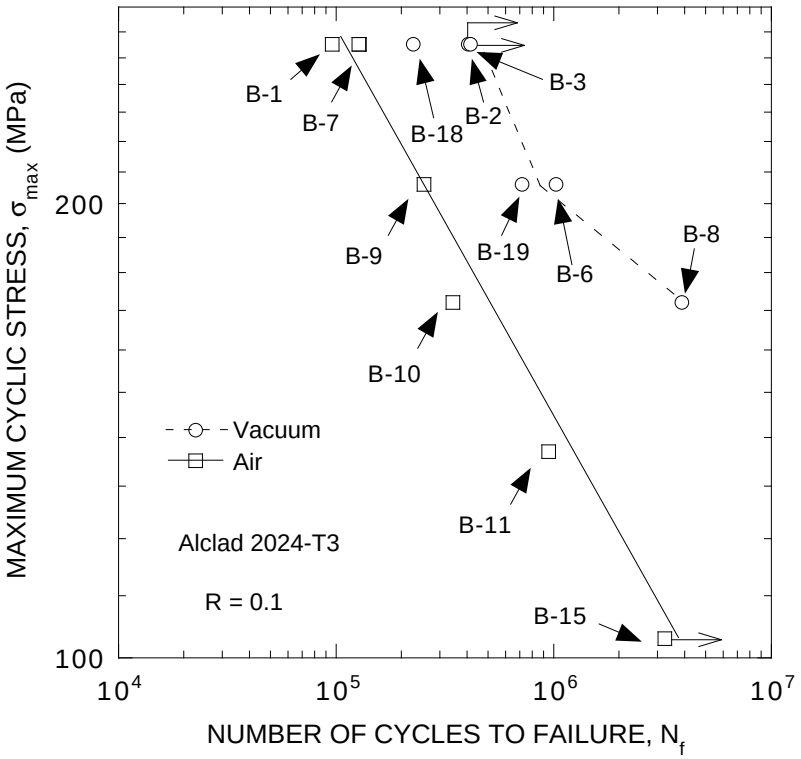

FIGURE 29. COMPARISON OF FATIGUE LIFE OF ALCLAD 2024-T3 ALUMINUM UNDER VACUUM AND IN AIR.

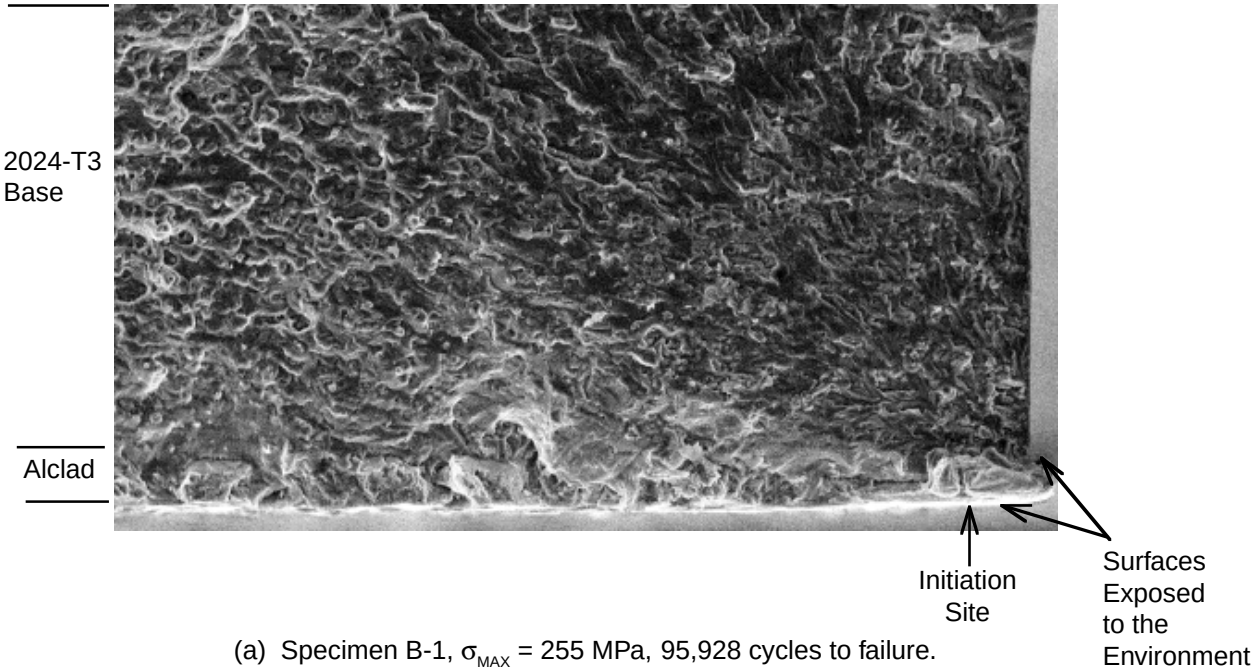

(a) Specimen B-1, σ_{MAX} = 255 MPa, 95,928 cycles to failure.

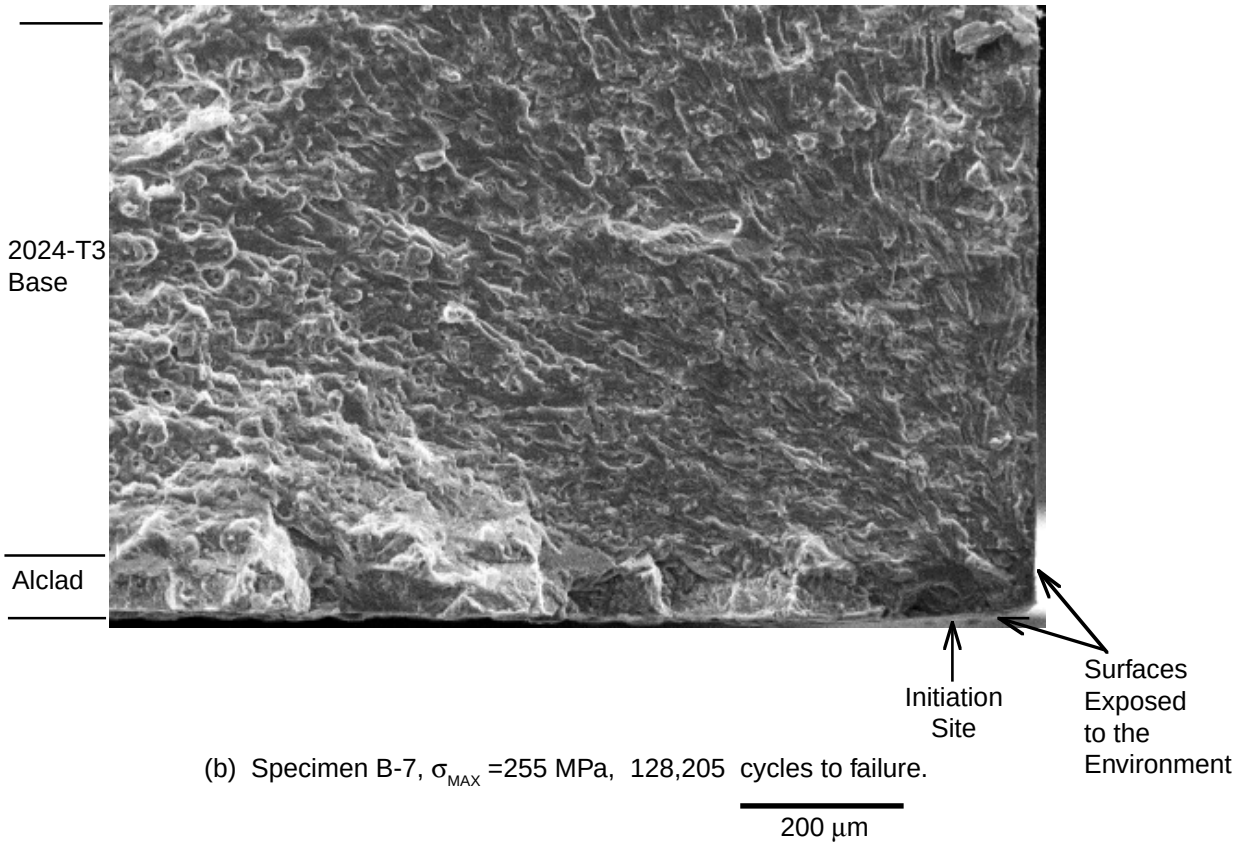

(b) Specimen B-7, σ_{MAX} =255 MPa, 128,205 cycles to failure.

FIGURE 30. FRACTURE SURFACE APPEARANCE OF ALCLAD 2024-T3 FATIGUE SPECIMENS TESTED IN AIR.

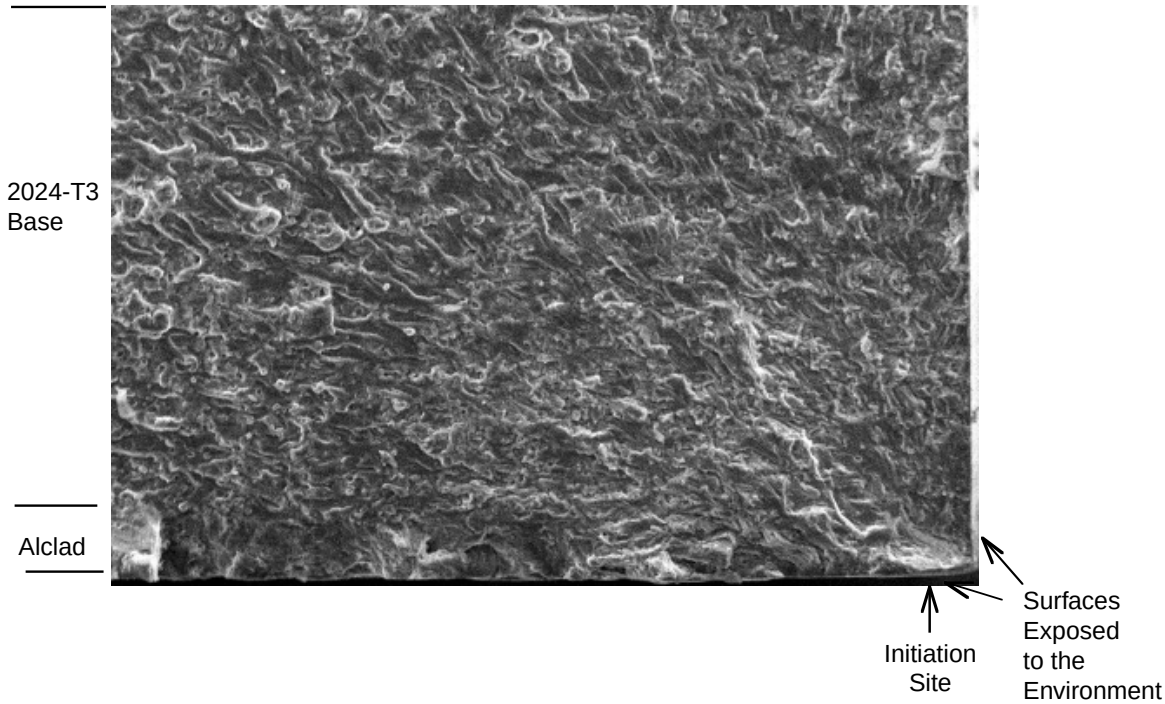

(c) Specimen B-9, σ_{MAX} = 207 MPa, 253,201 cycles to failure.

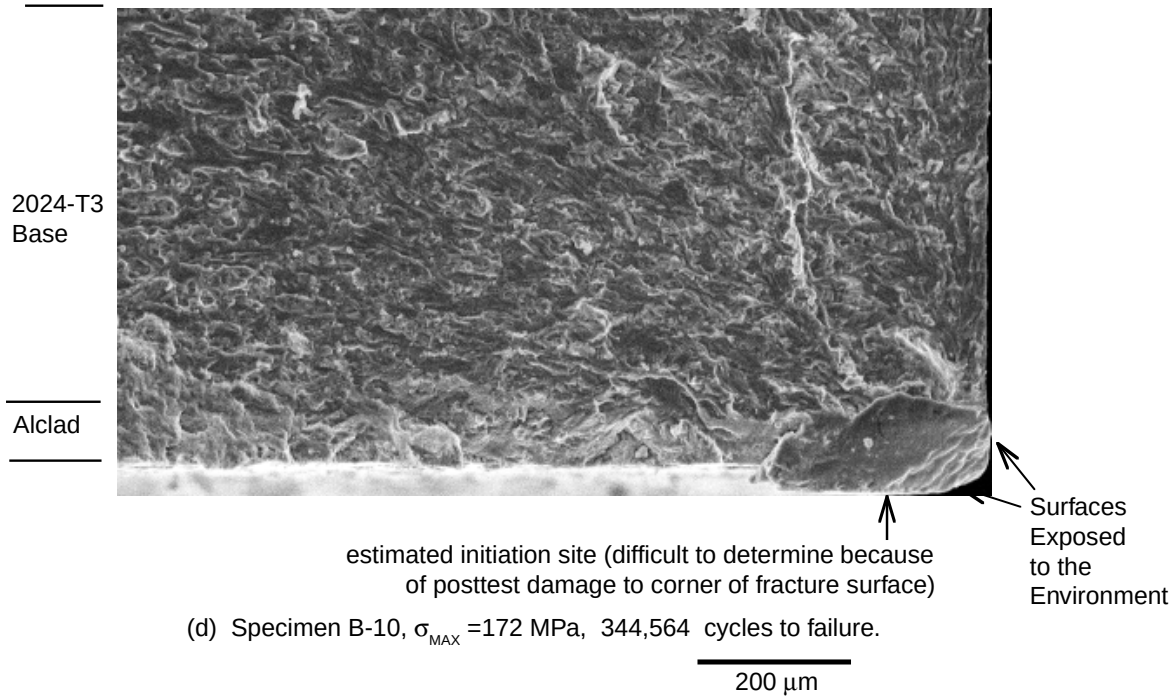

(d) Specimen B-10, σ_{MAX} =172 MPa, 344,564 cycles to failure.

FIGURE 30. FRACTURE SURFACE APPEARANCE OF ALCLAD 2024-T3 FATIGUE SPECIMENS TESTED IN AIR. (CONCLUDED)

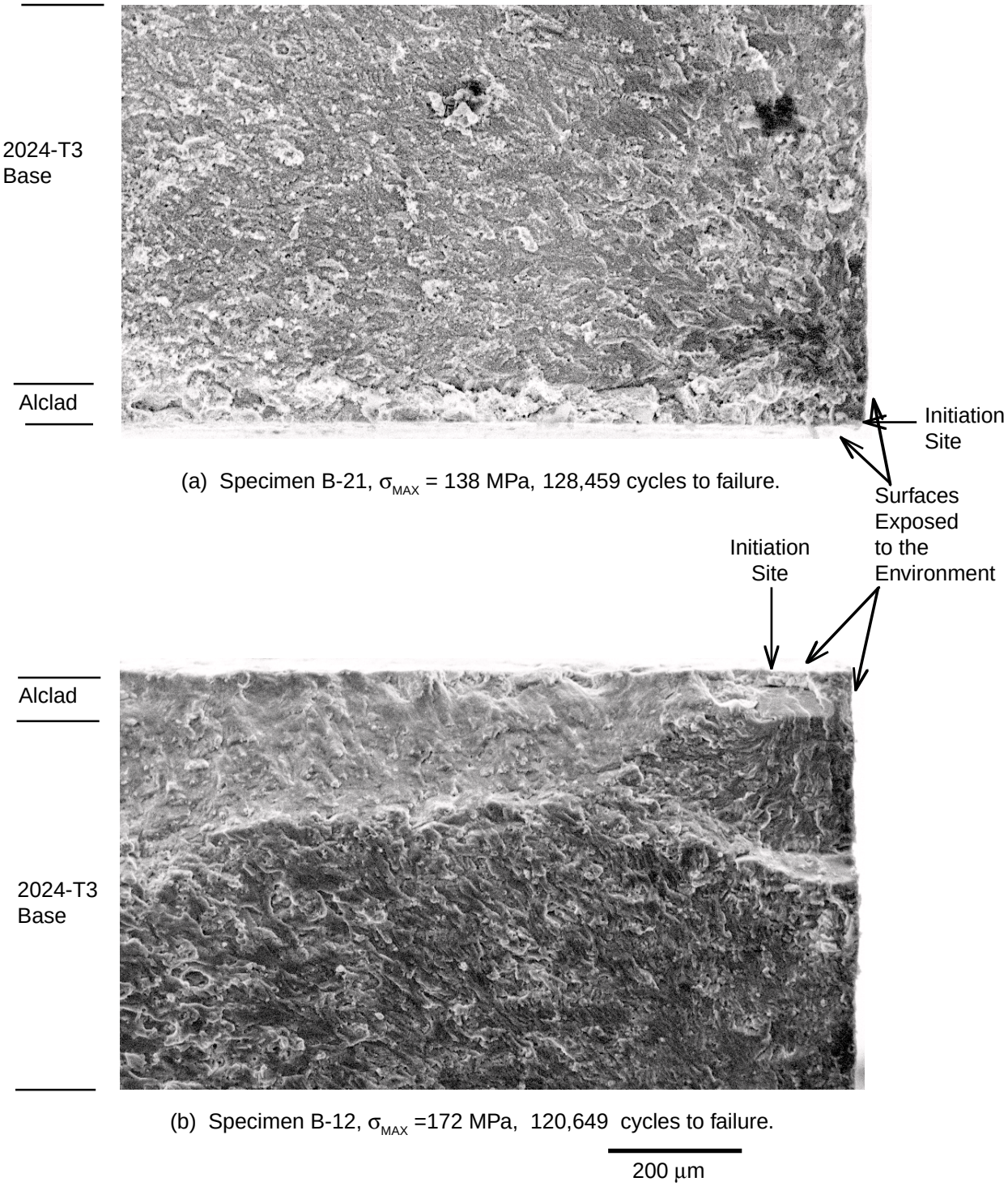

(a) Specimen B-21, σ_{MAX} = 138 MPa, 128,459 cycles to failure.

(b) Specimen B-12, σ_{MAX} =172 MPa, 120,649 cycles to failure.

FIGURE 31. FRACTURE SURFACE APPEARANCE OF ALCLAD 2024-T3 FATIGUE SPECIMENS TESTED IN 0.5 M NaCl SOLUTION.

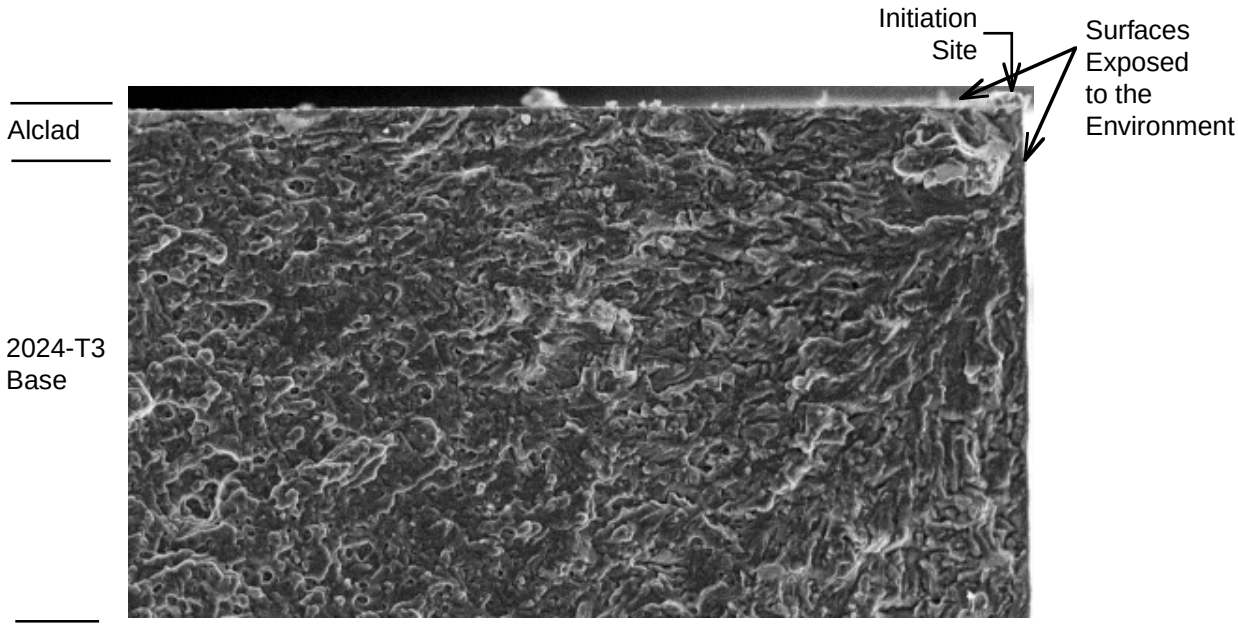

(c) Specimen B-14, σ_{MAX} = 207 MPa; 68,963 cycles to failure.

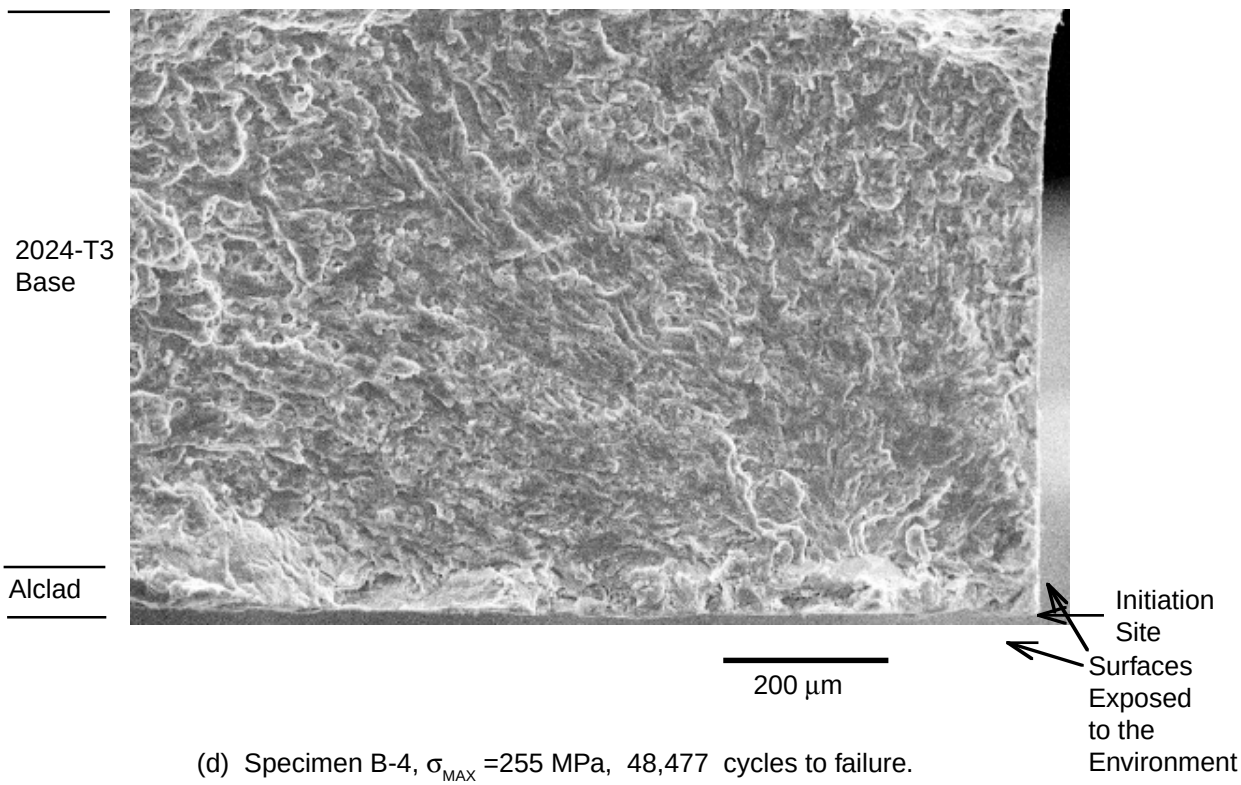

(d) Specimen B-4, σ_{MAX} =255 MPa, 48,477 cycles to failure.

FIGURE 31. FRACTURE SURFACE APPEARANCE OF ALCLAD 2024-T3 FATIGUE SPECIMENS TESTED IN 0.5 M NaCl SOLUTION. (CONCLUDED)

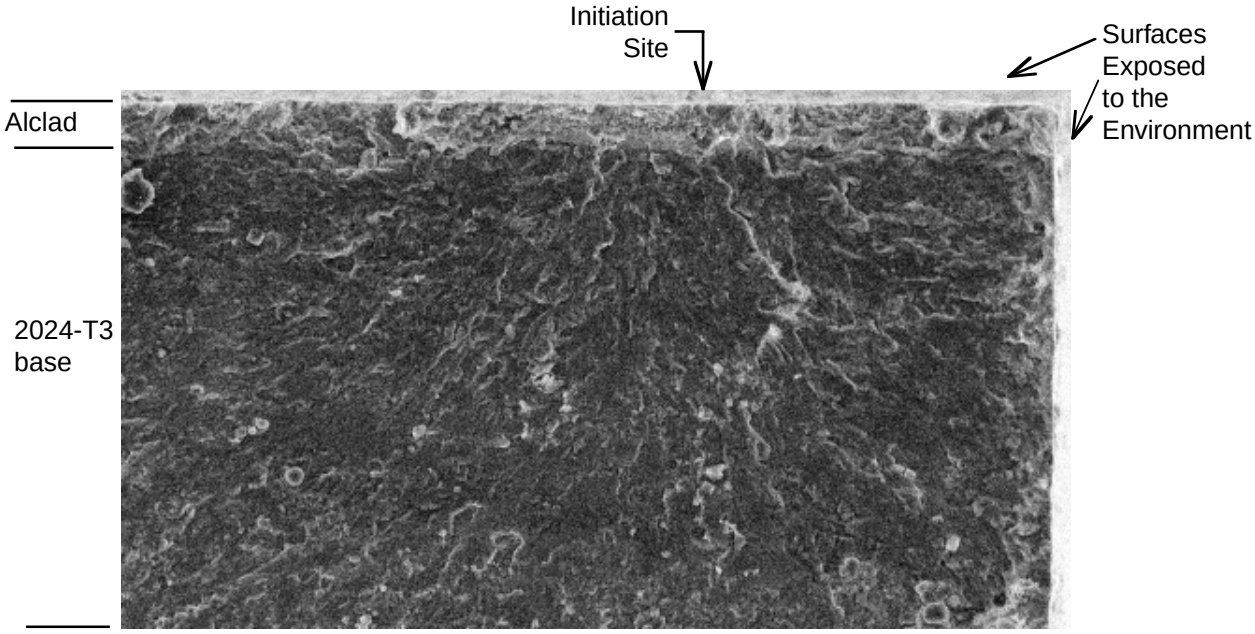

(a) Specimen B-22, σ_{MAX} = 138 MPa, 214,108 cycles to failure.

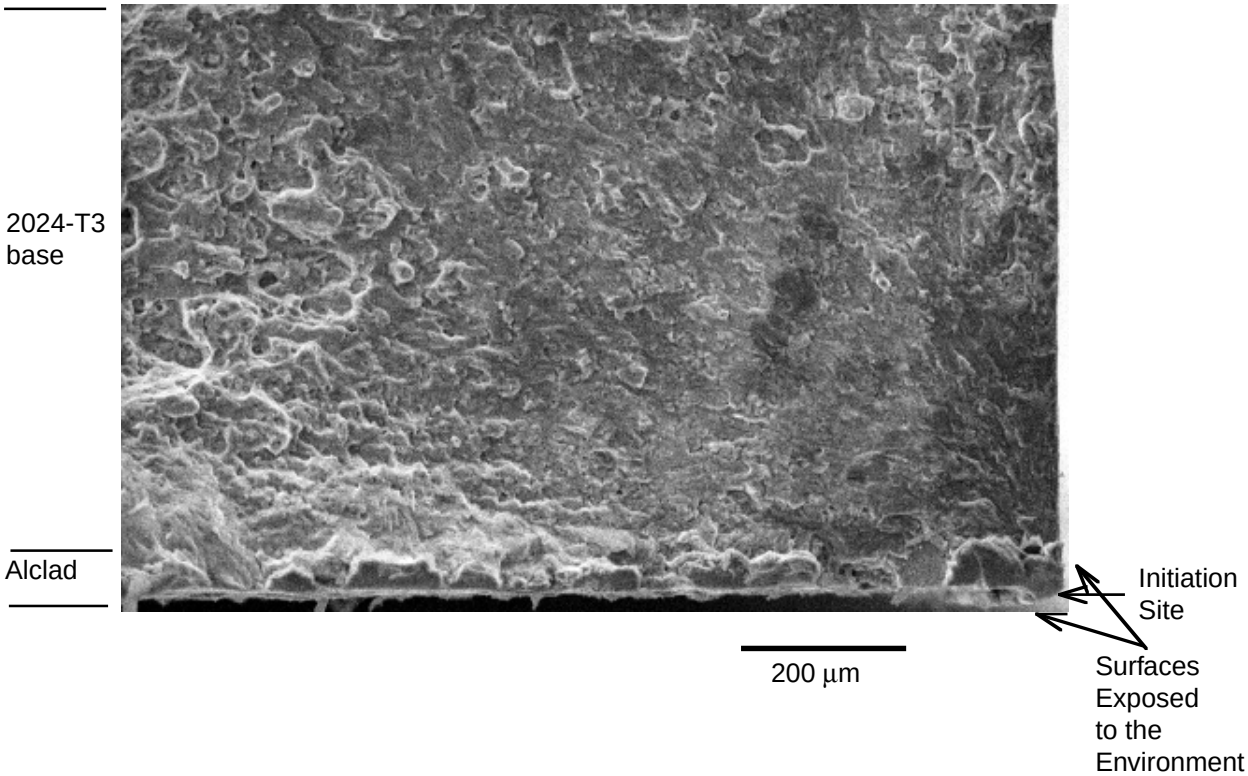

(b) Specimen B-20, σ_{MAX} =172 MPa, 133,278 cycles to failure.

FIGURE 32. FRACTURE SURFACE APPEARANCE OF ALCLAD 2024-T3 FATIGUE SPECIMENS TESTED IN 0.5 M NaCl SOLUTION + 0.13 M As_2O_3.

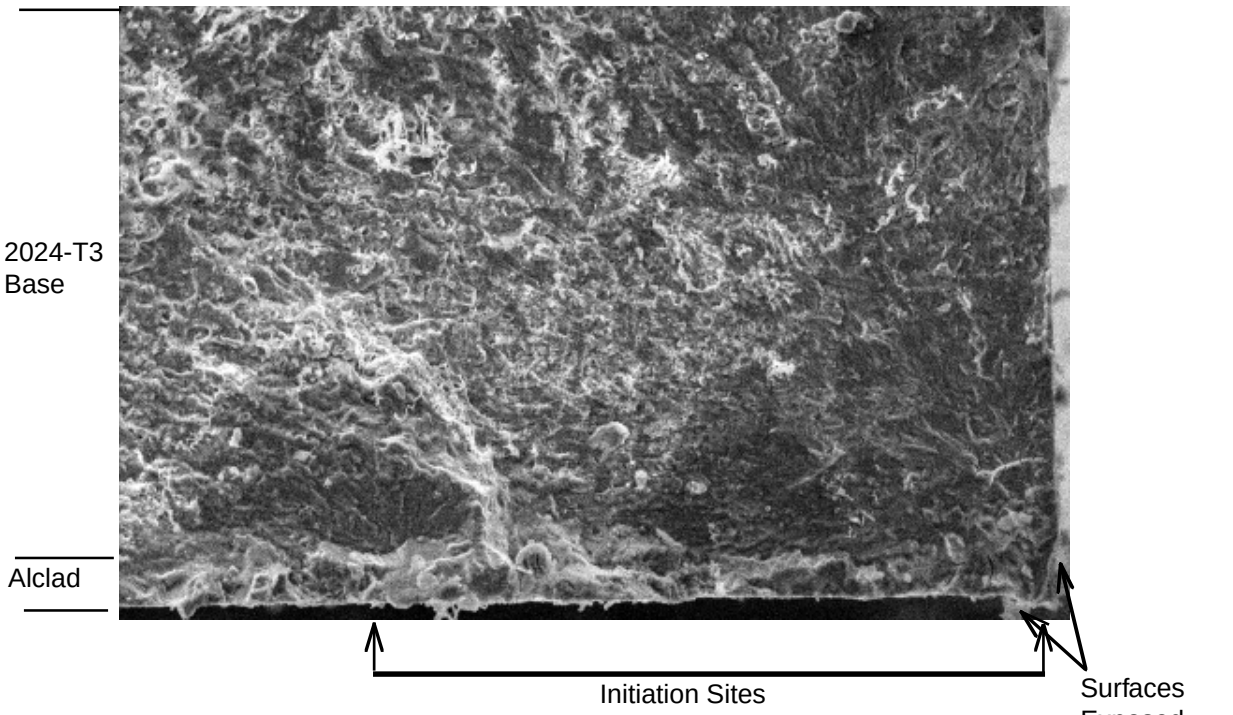

(c) Specimen B-16, σ_{MAX} = 207 MPa, 47,329 cycles to failure.

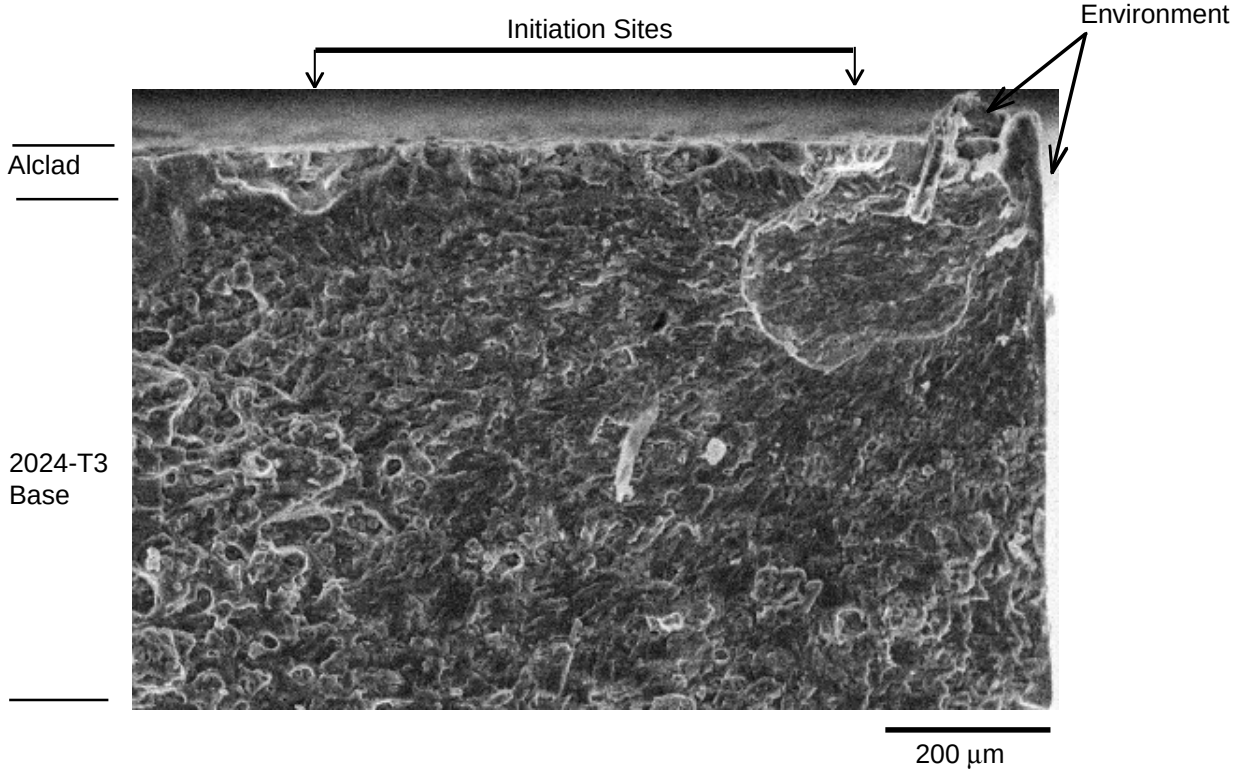

(d) Specimen B-5, σ_{MAX} =255 MPa; 32,804 cycles to failure.

FIGURE 32. FRACTURE SURFACE APPEARANCE OF ALCLAD 2024-T3 FATIGUE SPECIMENS TESTED IN 0.5 M NaCl SOLUTION + 0.13 M As_2O_3. (CONCLUDED)

Figures 33 through 35 show the results of tests on bare material.

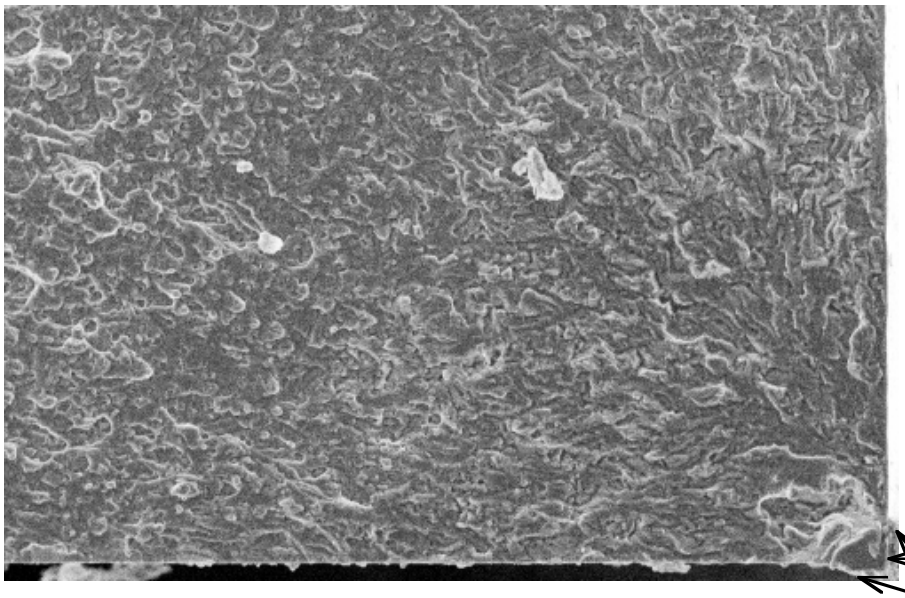

Initiation Site

Surfaces Exposed to the Environment

(a) Specimen C-13, σ_{MAX} = 207MPa; 2,638,930 cycles to failure.

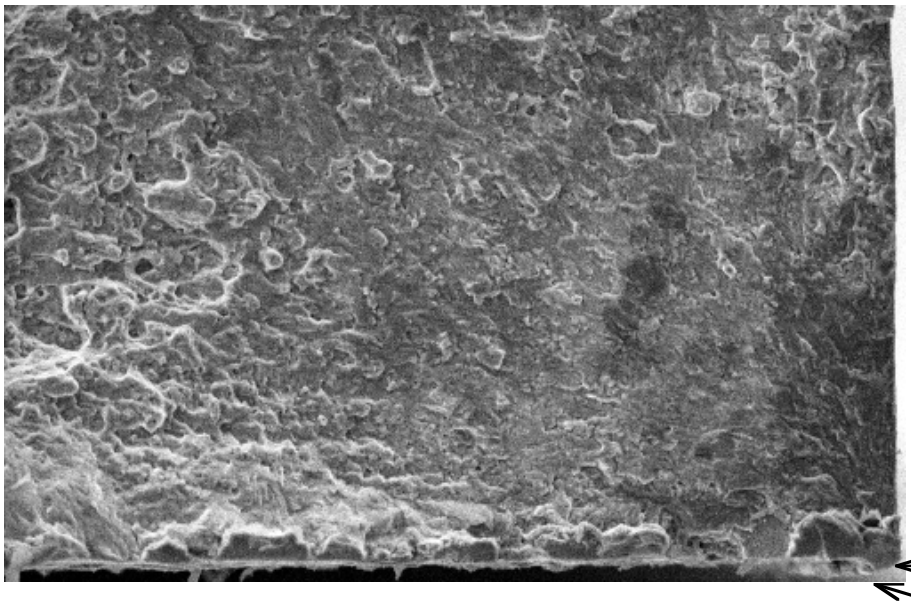

Initiation Site

Surfaces Exposed to the Environment

(b) Specimen C-3, σ_{MAX} = 207 MPa; 1,650,854 cycles to failure.

200 µm

FIGURE 33. FRACTURE SURFACE APPEARANCE OF BARE 2024-T3 FATIGUE SPECIMENS TESTED IN VACUUM.

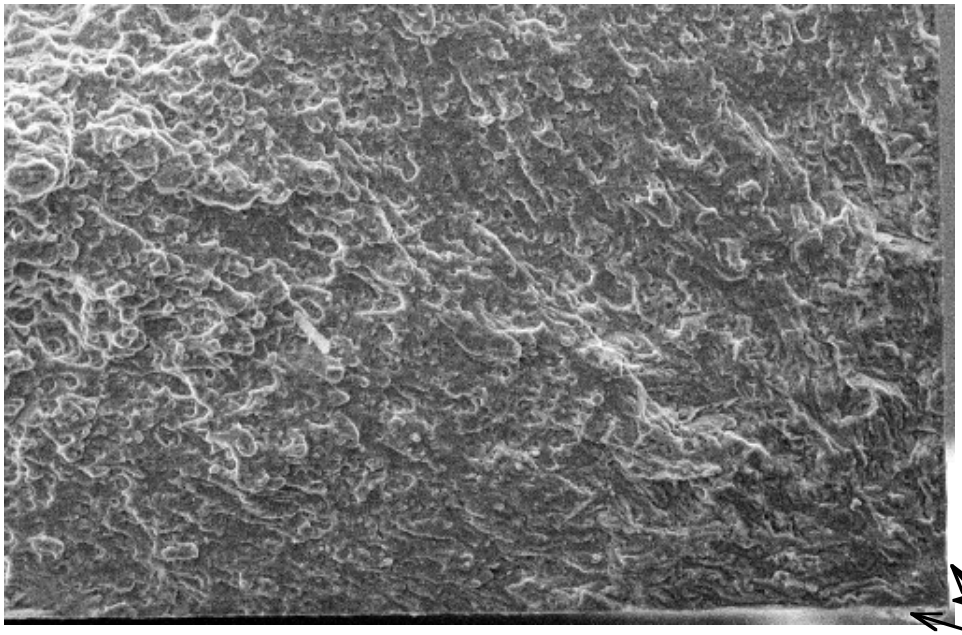

Initiation Site

Surfaces Exposed to the Environment

(c) Specimen C-14, σ_{MAX} = 255 MPa; 499,773 cycles to failure.

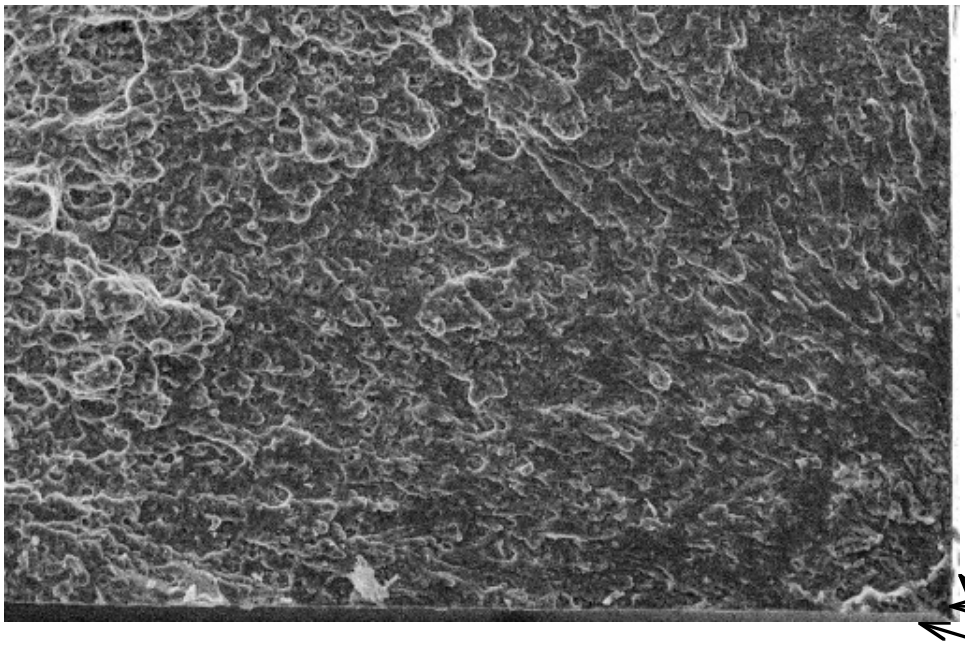

Initiation Site

Surfaces Exposed to the Environment

(d) Specimen C-4, σ_{MAX} = 255 MPa; 645,519 cycles to failure.

200 μm

FIGURE 33. FRACTURE SURFACE APPEARANCE OF BARE 2024-T3 FATIGUE SPECIMENS TESTED IN VACUUM. (CONCLUDED)

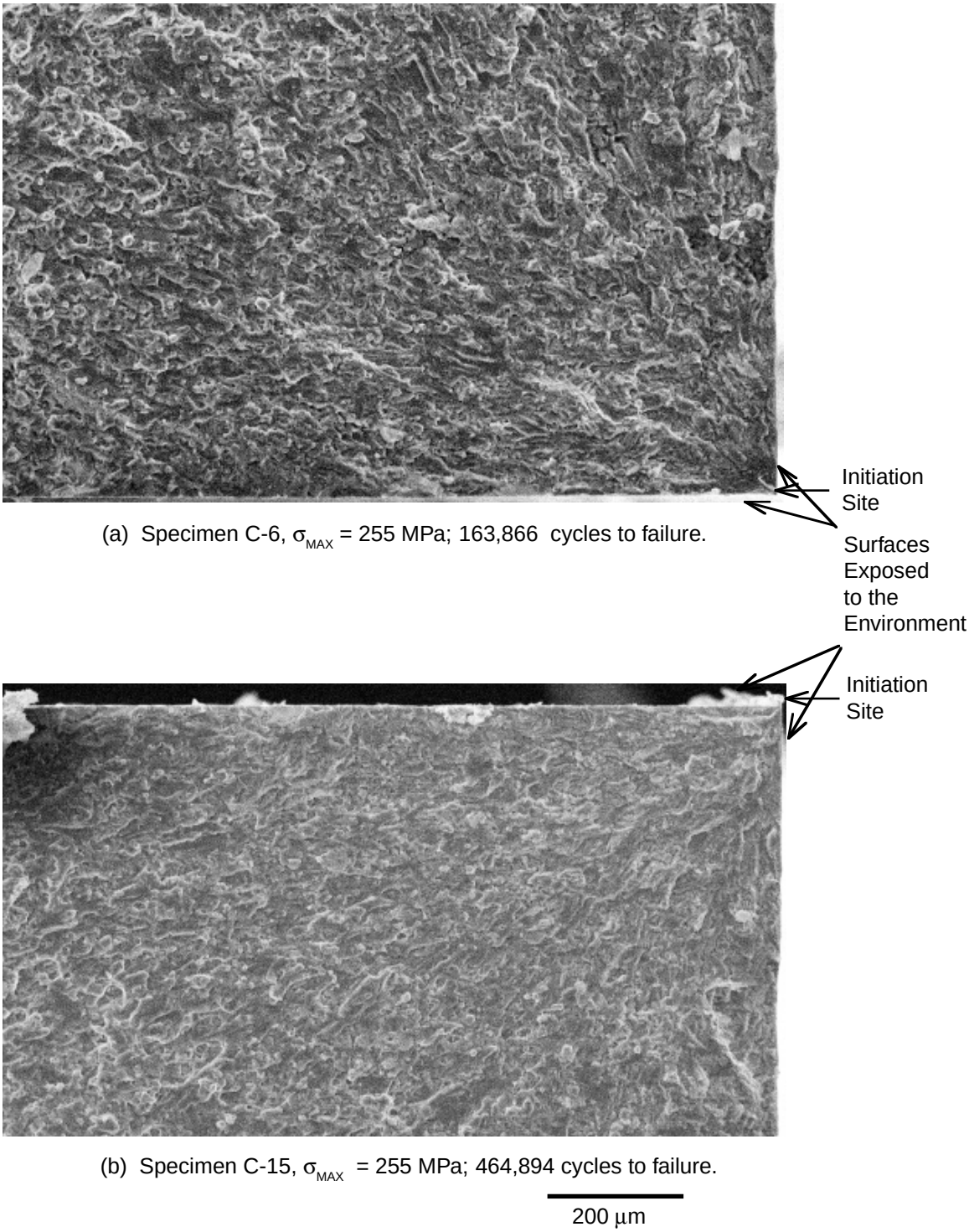

(a) Specimen C-6, σ_{MAX} = 255 MPa; 163,866 cycles to failure.

(b) Specimen C-15, σ_{MAX} = 255 MPa; 464,894 cycles to failure.

FIGURE 34. FRACTURE SURFACE APPEARANCE OF BARE 2024-T3 FATIGUE SPECIMENS TESTED IN AIR.

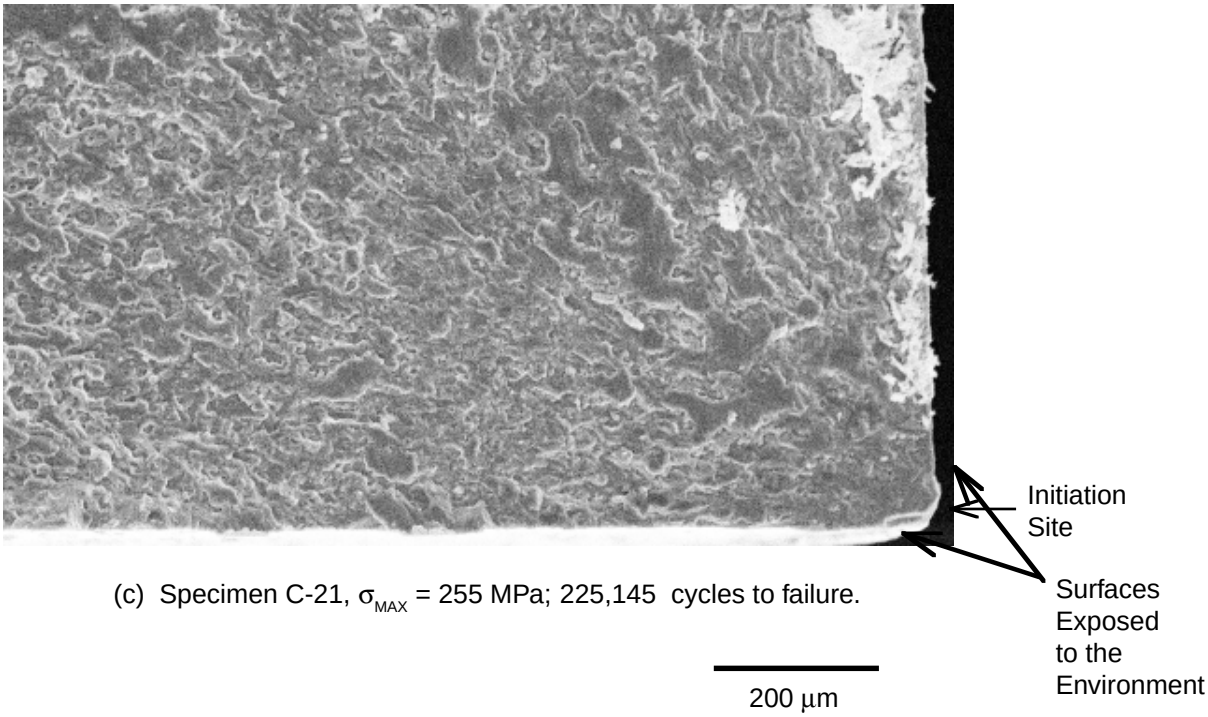

(c) Specimen C-21, σ_{MAX} = 255 MPa; 225,145 cycles to failure.

FIGURE 34. FRACTURE SURFACE APPEARANCE OF BARE 2024-T3 FATIGUE SPECIMENS TESTED IN AIR. (CONCLUDED)

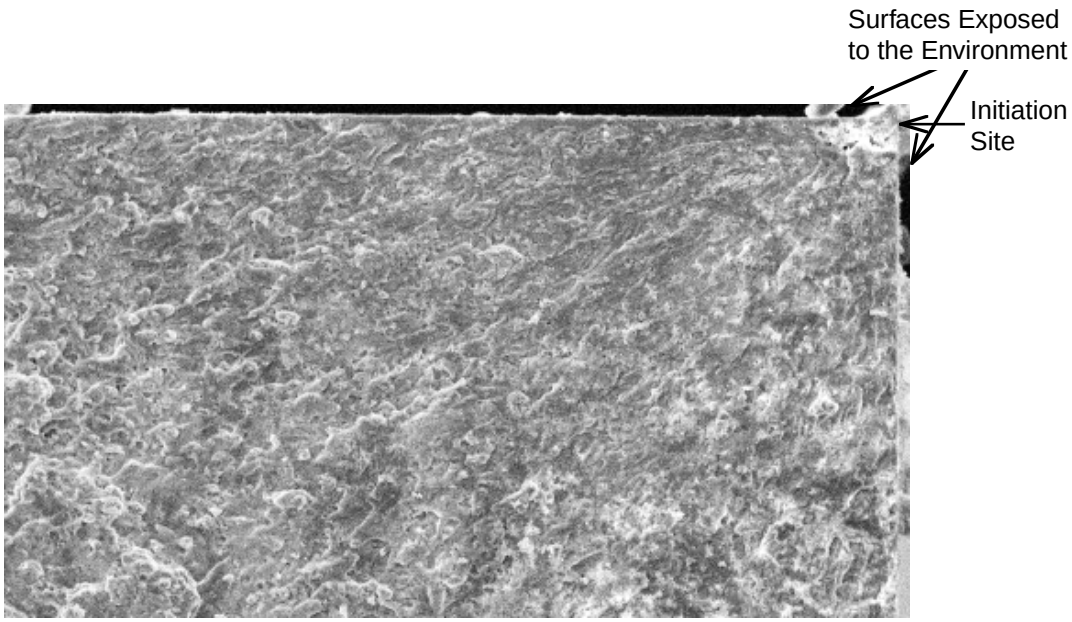

(a) Specimen C-8, σ_{MAX} = 255 MPa; 31,098 cycles to failure.

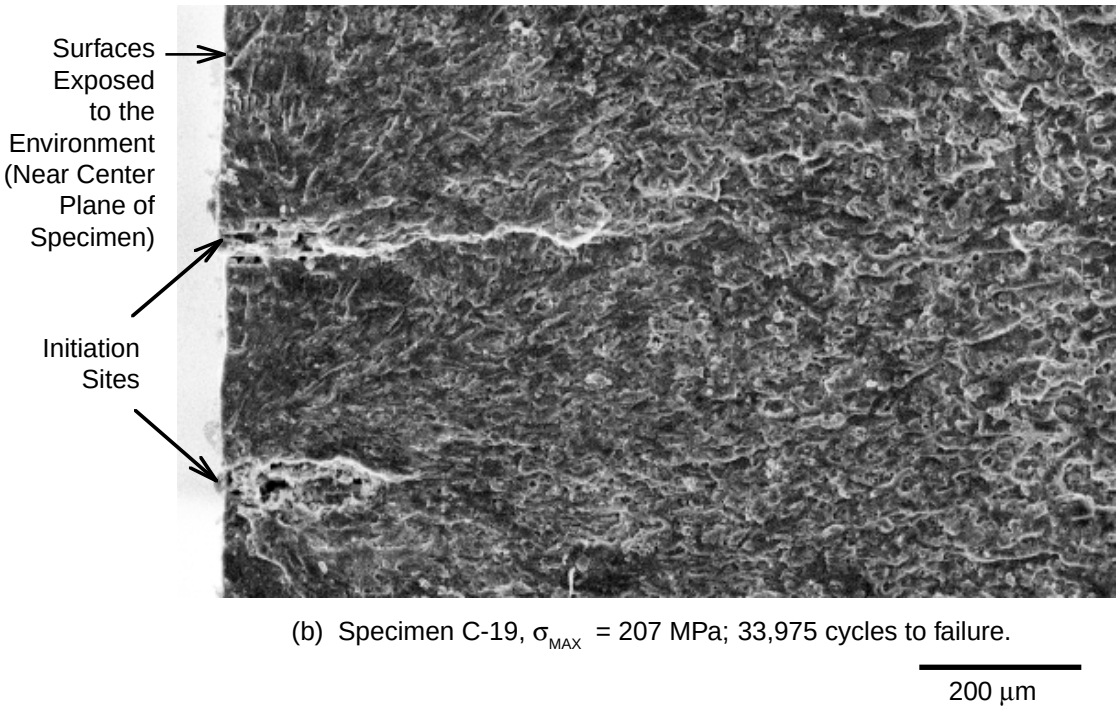

(b) Specimen C-19, σ_{MAX} = 207 MPa; 33,975 cycles to failure.

FIGURE 35. FRACTURE SURFACE APPEARANCE OF BARE 2024-T3 FATIGUE SPECIMENS TESTED IN 0.5 M NaCl SOLUTION.

5.3 DISCUSSION.

The location of fatigue crack nucleation in clad 2024-T3 sheet was observed to vary with the aggressiveness of the environment. Environments of low to moderate aggressiveness (vacuum or laboratory air) produced fatigue failures that nucleated at the corners of the specimen. A more aggressive environment (arsenated salt water) promoted crack nucleation away from the specimen corners at multiple locations. In bare 2024-T3 sheet, cracks nucleated at the corners of the specimens in environments with low to moderate aggressiveness. Fatigue cracks nucleated in more aggressive environments due to elongated pits resulting from constituent particle corrosion. Substantial and consistent reductions in the fatigue life occurred only in the environments that produced elongated pits (i.e., in laboratory air as shown in figure 30).

These observations indicate that a modest driving force exists that promotes crack nucleation at the corners of the specimen. This driving force can be overcome in aggressive environments because other crack nucleation sites become active over the clad surface or, in bare 2024-T3 sheet, because rapid pitting creates crack nucleation sites in the vicinity of constituent particles.

The affinity of crack nucleation for the corners of the specimen does not appear to be due to local environmental conditions at those locations because corner nucleation occurred in tests conducted under vacuum. It is unclear whether favorable crack nucleation conditions were created by unique stress conditions or material conditions (e.g., cold work induced by machining of the specimen gage length through-thickness surfaces) at the specimen corners.

In a previous report[1] from this research program, corrosion-fatigue damage in salt water was divided into two categories: (1) in bare 2024-T3 sheet, cracks nucleate at constituent particles and (2) in clad 2024-T3 sheet, crystallographic (Stage I) cracks nucleate at a location that, on final failure, is at a corner of the fracture surface. These observations are confirmed by the present results and by the work of other investigators.[21,22] However, the present results extend these observations to less aggressive environments that show that (1) the fatigue life of bare 2024-T3 sheet is not substantially reduced and, at some stress levels, can be increased by a moderately aggressive environment that does not produce elongated pits (i.e., in laboratory air, as shown in figure 27), and (2) the fatigue life of clad 2024-T3 sheet is substantially reduced (i.e., by a factor of 2 to 10, as shown in figure 27) by a moderately aggressive environment even though the location and appearance of the nucleation site are not affected substantially by the environment.

The effect of environment on the fatigue life of bare 2024-T3 coupled with the effect of that environment on the crack nucleation location indicates that the formation of elongated pits is the major reason that severely aggressive environments reduce fatigue life. The reason that laboratory air can increase the fatigue life over that of the vacuum environment is unclear.

For clad 2024-T3, fatigue failures always nucleated in the clad. The reduction in fatigue life in the laboratory air environment is attributed to enhanced crack nucleation in the clad rather than an enhancement in the crack propagation rate because no corresponding reduction in fatigue life was observed for bare 2024-T3. No obvious change in the crack nucleation mechanism was observed between the vacuum and laboratory air tests on clad 2024-T3, and it is clear that no large-scale

surface stress concentrators (e.g., pits) that enhance crack nucleation were created by the laboratory air environment. Consequently, we must look to other possible interactions between the laboratory air environment and the clad to understand the reason crack nucleation was enhanced.

A likely mechanism for enhanced crack nucleation is the weakening effect of hydrogen on pure aluminum. Relevant work showing the effect of hydrogen on crack propagation in pure aluminum was cited in a previous report[1] and is provided below.

- Hydrogen cracking in pure aluminum has been reported in at least two cases. Bond et al.[23] induced cracking in high-purity aluminum, transmission electron microscope specimens by injecting small amounts of hydrogen into the microscope. The hydrogen in the microscope column enhanced cracking and dislocation activity, which suggests that embrittlement was actually a result of hydrogen enhanced localized plasticity (known as the HELP mechanism).

- Tong et al.[24,25] observed that hydrogen usually increased the rate of corrosion fatigue cracking in pure aluminum single crystals in Mode II and in mixed Mode I/Mode II loading. Sustained cracking was restricted to the close-packed crystallographic planes and directions. In most cases, crack growth rates were substantially higher (by as much as a factor of 100) in water-vapor-saturated air when compared with the dry-air results. Exceptions to this trend were observed in specific situations when the crystallographic orientation was favorable for the aqueous environment to promote secondary microcracks that effectively blunt the primary crack tip.

- Using an ion microprobe, Tong et al. determined that local deformation substantially increased the amount of hydrogen in aluminum single crystals immersed in various aqueous environments over that possible by diffusion alone. The high hydrogen contents were found near fatigue fracture surfaces and were attributed to transport enhanced by dislocation sweeping. For example, they found that pure aluminum fracture surfaces fatigued in water-vapor-saturated air exhibited a hydrogen content of 6.02 ppm compared with 0.58 ppm for dry air with a relative humidity of less than 20%. Furthermore, they used an ion microprobe to show that hydrogen could promote plastic deformation by reducing the atomic binding energy of aluminum. The magnitude of this reduction was measured to be 11% for an average hydrogen content of 7.5 ppm. The mechanical weakening effect of hydrogen was confirmed through measurements showing that the critical resolved shear stress of aluminum was reduced by hydrogen absorbed from aqueous solutions or moist air when compared with aluminum stored in dry air. For example, the critical resolved shear stress was 1.96 MPa and 1.65 MPa for aluminum with hydrogen levels adjusted to 0.58 and 4.43 ppm, respectively.

The work of Tong et al. and Bond et al. is especially relevant to our study because they identify credible mechanisms involved in the overall process of hydrogen enhanced nucleation and growth

of fatigue cracks in the pure aluminum clad layer on 2024-T3 sheet exposed to aqueous and moist air environments. Their experiments with pure aluminum show that

- aqueous and moist air environments can produce high levels of hydrogen in the lattice, especially when effective diffusion rates are enhanced by dislocation sweeping from local deformation.
- once in the lattice, hydrogen significantly reduces the critical resolved shear stress.
- the reduction in shear resistance is accompanied by a reduction in the atomic bonding energy in aluminum as a result of dissolved hydrogen.
- hydrogen in aluminum can increase the crack growth rate substantially under static or fatigue loads.

These findings suggest that, although the cladding of 2024-T3 clearly protects the core alloy from corrosion in a range of environments, the clad can be a favorable site for fatigue crack nucleation. Furthermore, the effects of hydrogen on pure aluminum suggest that countermeasures that limit the availability or the effects of hydrogen might provide enhanced corrosion-fatigue performance in clad 2024-T3.

5.4 SUMMARY.

- The fatigue life of bare and clad 2024-T3 sheet was examined in environments of vacuum, laboratory air, 0.5 M NaCl solution, and 0.5 M NaCl + 0.13 M As_2O_3 solutions to evaluate the importance of environmental factors on corrosion fatigue life. For bare material, the fatigue life in the salt water environments was substantially less than the life under vacuum. The fatigue life in air was less than the fatigue life under vacuum at a maximum fatigue stress of 255 MPa; however, at 207 MPa, the relative magnitudes of the fatigue life were reversed.
- Clad material tested in salt water exhibited fatigue lives that were a factor of about 7 to 30 less than the fatigue lives under vacuum. Fatigue life in air was a factor of 2 to 10 less than the fatigue life under vacuum.
- In bare 2024-T3 sheet, cracks nucleated at the corners of the fracture surfaces in environments with low to moderate aggressiveness. Fatigue cracks nucleated in more aggressive environments due to elongated pits resulting from constituent particle corrosion. Substantial and consistent reductions in the fatigue life occurred only in the environments that produced elongated pits.

- The location of fatigue crack nucleation in clad 2024-T3 sheet was observed to vary with the aggressiveness of the environment. Environments of low to moderate aggressiveness (vacuum or laboratory air) produced fatigue failures that nucleated at the corners of the specimens.

- A likely mechanism for enhanced crack nucleation in 2024-T3 sheet with pure aluminum clad is the weakening effect of hydrogen on pure aluminum.

6. REFERENCES

1. C. G. Schmidt, J. E. Crocker, J. H. Giovanola, C. H. Kanazawa, and D. A. Shockey, "Characterization of Early Stages of Corrosion Fatigue in Aircraft Skin," Report No. DOT/FAA/AR-95/108 (February 1996).

2. C. G. Schmidt, D. A. Shockey, P. J. McAlpine, W. M. Taylor, and V. J. Monteparte, "Corrosion Fatigue Experience in Commercial Aircraft," Topical Report, FAA Contract No. 93-G-065 (May 1996).

3. R.M.N. Pelloux, "Crack Extension by Alternating Shear," *Engng. Fract. Mech.* **1**, 697-704 (1970).

4. C. Q. Bowles and D. Broek, "On the Formation of Fatigue Striations," *Int. J. Fract.* **8**, 75-85 (1972).

5. P. C. Paris and F. Erdogan, "Critical Analysis of Crack Propagation Laws," *Trans. Am. Soc. Mech. Engrs.* **85D**, 528-534 (1963).

6. Y. Murakami, N. Shiraishi, and K. Furukawa, "Estimation of Service Loading from the Width and Height of Fatigue Striations of 2017-T4 Al Alloy," *Fatigue Fract. Engng. Mater. Struct.* **14** (9), 897-906 (1991).

7. K. Furukawa, Y. Murakami, and S.-I. Nishida, "A Method for Predicting Service Load from the Width and Height of Striation," *J. Soc. Maters. Sci. Japan* **45**, 340-345 (March 1996).

8. R. H. McSwain and R. W. Gould, "Analysis of a Helicopter Blade Fatigue Fracture by Digital Fractographic Imaging Analysis," *Proceedings of the International Conference and Exposition on Fatigue, Corrosion Cracking, Fracture Mechanics and Failure Analysis*, V. S. Goel, Ed. (American Society for Metals, Salt Lake City, UT, 1985), pp. 87-91.

9. T. Kobayashi and D. A. Shockey, work in progress, SRI International, Menlo Park, CA, 1998.

10. T. Kobayashi and D. A. Shockey, "FRASTA: A New Way to Analyze Fracture Surfaces, Part 1: Reconstructing Crack Histories," *Advanced Materials & Processes* **140**, 28-34 (1991).

11. T. Kobayashi and D. A. Shockey, "Fracture Analysis Via FRASTA, Part 2: Determining Fracture Mechanisms and Parameters," Advanced Materials & Processes 140, 24-32 (1991).

12. D. E. Passoja and J. A. Psioda, "Fourier Transform Techniques—Fracture and Fatigue," in *Fractography and Materials Science, ASTM STP 733*, L. N. Gilbertson and R. D. Zipp, Eds. (American Society for Testing and Materials, Philadelphia, PA, 1981), p. 355.

13. R. H. McSwain, "Digitized Fractographic Image Analysis," Ph.D. thesis, University of Florida, Gainesville, FL (1985).

14. R. W. Gould and R. H. McSwain, "Fractographic Feature Identification and Characterization by Digital Image Analysis," in *Fractography of Modern Engineering Materials: Composites and Metals*, ASTM STP 948, 263-292 (1987).

15. C. G. Schmidt, T. Kobayashi, D. A. Shockey, and T. H. Flournoy, "Correlation of Fracture Surface Topography with Fatigue Load History," Proceedings of the International Committee on Aeronautical Fatigue 1997, Edinburgh, Scotland (June 16-20, 1997).

16. T. Kobayashi, D. A. Shockey, C. G. Schmidt, and R. W. Klopp, "Assessment of Fatigue Load Spectrum from Fracture Surface Topography," *Int. J. Fatigue* **19**, S237-S244 (1997).

17. P. Wawrzynek and A. Ingraffea, "FRANC2D: A Two-Dimensional Crack Propagation Simulator," Version 2.7 User's Guide, NASA Contractor Report 4572 (March 1994).

18. JSME S 001-1981, "Standard Method of Test for Elastic-Plastic Fracture Toughness, J_{IC}," Japan Society of Mechanical Engineers, Tokyo (October 1981).

19. G. R. Irwin, "Plastic Zone near a Crack and Fracture Toughness," Proc. 7th Sagamore Conf. (1960), p. IV-63.

20. Metals Handbook, *Fractography and Atlas of Fractographs*, Vol. 9, Eighth Edition (American Society for Metals, Metals Park, OH, 1974), pp. 68-70.

21. J. Chaudhuri, Y. M. Tan, V. Gondhalekar, and K. M. Patni, "Comparison of Corrosion Fatigue Properties of Precorroded 6013 Bare and 2024 Bare Aluminum Alloy Sheet Materials," *J. Mater. Engr. Perform.* **3**, 371-377 (1994).

22. J. Chaudhuri, Y. M. Tan, K. M. Patni, and A. Eftekhari, "Comparison of Corrosion Fatigue Properties of 6013 Bare, Alclad 2024, and 2024 Bare Aluminum Alloy Sheet Materials," *J. Mater. Engr. Perform.* **1**, 91-96 (1992).

23. G. M. Bond, I. M. Robertson, and H. K. Birnbaum, "Effects of Hydrogen on Deformation and Fracture Processes in High-Purity Aluminum," *Acta Metall.* **36**, 2193-2197 (1988).

24. Z-X Tong, S. Lin, and C-M Hsiao, "The Influence of Hydrogen on Atomic Binding Energy, Critical Slip Shear Stress, and Fatigue Crack Propagation Rate of Aluminum Single Crystals," *Metall. Trans.* **20A**, 921-924 (1989).

25. Z-X Tong, S. Lin, and C-M Hsiao, "The Influence of Water Vapor on the Fatigue Crack Propagation Kinetics in Pure Aluminum Single Crystals," *Metall. Trans.* **20A**, 925-933 (1989).

APPENDIX A

SEM STEREO PROGRAM DEVELOPMENT

To facilitate the analysis of failure surfaces in aging aircraft fuselages, SRI International attempted to develop a higher resolution method for characterizing surface topography based on the scanning electron microscope (SEM). This appendix describes the algorithmic functions of the software program and shows the results of applying this program to three example problems.

DEVELOPMENT OF STEREO SEM ANALYSIS PROGRAM.

In sections 2, 3, and 4, SRI International used a stand-alone, confocal-optics-based scanning laser microscope (COSLM) system for fracture surface topography characterization. Although the COSLM system provides direct and accurate characterization of topography, it is limited in its resolution to magnifications of about 1,500-2,000 times. In analyzing the fatigue behavior of fuselages and other structures, a capability for examining fracture surface topography at higher magnifications would be useful.

A likely base instrument for such a capability is the scanning electron microscope since it can produce higher magnification images desirable for examining important details of corrosion fatigue. Thus we attempted to develop a procedure and software for obtaining numerical topography information from SEM images or photographs.

STEREO ANALYSIS PROGRAM AND IMPLEMENTED FUNCTIONS.

The technique of three-dimensional visual reconstruction using a pair of SEM photographs of a surface area taken from two different directions has been known and used for many years. However, quantifying the topography information accurately, automatically, and efficiently requires a fast and easy-to-use software program.

Stereoimage reconstruction is based on the fact that the location of a specific feature point on the left photograph differs from that on the right photograph, and that this difference is proportional to the elevation (parallax). To develop a computational program to compare the left and right images, to compute the parallax, and to convert the result to elevation we require that

(1) the stereo images be at the same known magnification,

(2) the alignment of the pair of stereoimages be such that the axis of rotation of the view point between the two images is known and parallax occurs in the direction perpendicular to the axis of rotation, and

(3) the angle of rotation between the pair of images is known.

One of the difficulties in analyzing a SEM stereopair of photographs is that in most cases photographs are taken individually by rotating the stage and thereby introducing a slight change in magnification, orientation of image, and imaged area. Thus, the computer program for stereoanalysis has to have an ability to correct for these changes and to set up the stereopair of photographs properly.

We have implemented the following functions:

(1) Superposition of Stereopair Images for Alignment.

This function will allow artificially colored left (red) and right (green) images to be overlaid and displayed on the computer monitor and enable either image to be shifted in the x and y direction, rotated in-plane, and zoomed (magnified or reduced in size) with respect to the other image. All these operations are performed by clicking the mouse.

(2) Computation of Elevation.

After aligning the images, elevation is computed by clicking the mouse. The elevation is computed by comparing the segmental area (5 x 5 pixels) on the left side of the image with the default search window area (11 x 7 pixels) and finding the best fit location within the search window. The shift from the center of the search window is the parallax and this value is recorded. The segmental area in the left image is then shifted one pixel and the process repeated until the entire area is covered. Upon completion of this process, the gray-scale topography information is graphically displayed. If the search window size is not large enough, the elevation image displayed shows spotted areas. In this case, the search window size is increased by pulling down a menu, clicking on a window size specification box, typing in a new window size, and rerunning the calculation.

(3) Display of Result.

The program can display the SEM image, the computed elevation image, and a three-dimensional perspective view image. The perspective view can be rotated freely so that the topography of the surface can be examined from different view angles.

RESULTS.

To demonstrate the program capabilities, we arbitrarily selected several stereopair SEM images from a published book (Stereofractography by K. Komai, Yokendo Ltd. Tokyo, Japan, 1996) and applied our program.

Figures A-1(a) and A-1(b) show a stereopair of fracture surface photographs of a high-strength steel, HT80, tested under fatigue loading ($R = 0.1$, $f = 0.17$ Hz, and $\Delta K = 20$ MPa$\sqrt{m}$) in sea water at room temperature. The fracture surface features indicate a mixture of intergranular and transgranular fracture. Figure A-1(c) shows the gray-scale topography image computed by our program, and figure A-1(d) shows a perspective view of the surface.

The size of the images [figures A-1(a) and A-1(b)] is about 400 x 397 pixels, the search window size was 27 x 7 pixels, and the time of computation was about 38 seconds.

Figures A-2(a) and A-2(b) show a stereopair of fracture surface photographs of high-strength steel (HT60) fractured under static bending for the purpose of measuring cracktip opening displacement. The fatigue precrack area and stretch zone are evident. Figure A-2(c) shows the gray-scale topography image generated by the current program, and figure A-2(d) displays a 3D perspective view. The elevation results clearly illustrate the stretch zone step.

The size of the images was about 320 x 325 pixels; the search window size was 31 x 11 pixels; and the time of computation was about 29 seconds.

Figures A-3(a) and A-3(b) are a stereopair of SEM photographs of a 2024-T3 aluminum fracture surface in the area where an overload was applied during fatigue loading. The crack propagation direction was from top to bottom. The horizontal ridge in the middle of the image was caused by an overload. This surface exhibits a complex microscopic structure, and the calculated elevation data shown in figure A-3(c) depicts the feature details well.

In summary, an SEM-based stereoanalysis program has been developed that can be used to study details of fracture surface topography at higher magnifications than is possible with a confocal optics scanning laser microscope. Further improvements are necessary to shorten computational time and to reduce the local noise in the elevation data.

(a) Left SEM Photograph

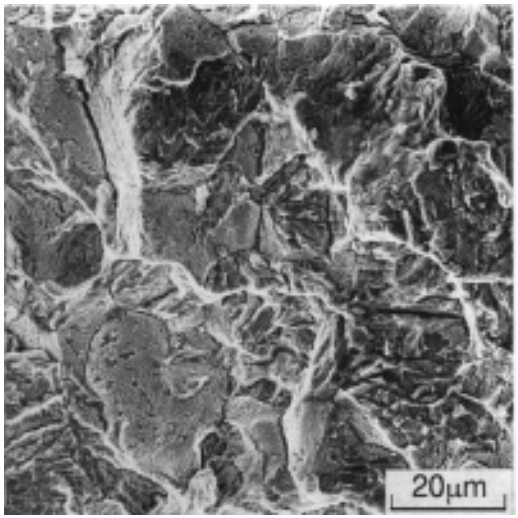

(b) Right SEM Photograph

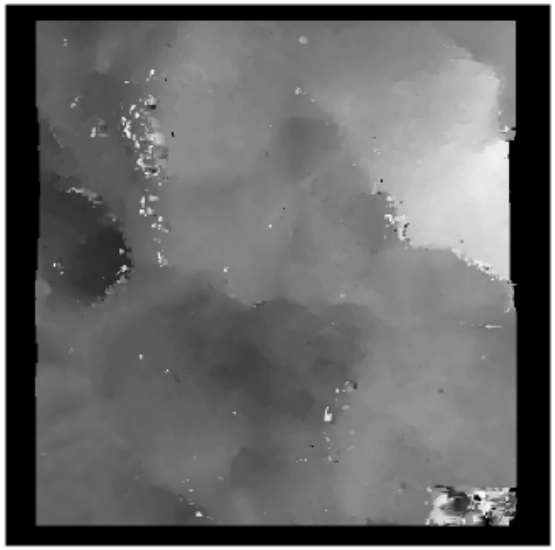

(c) Grayscale Topography Image

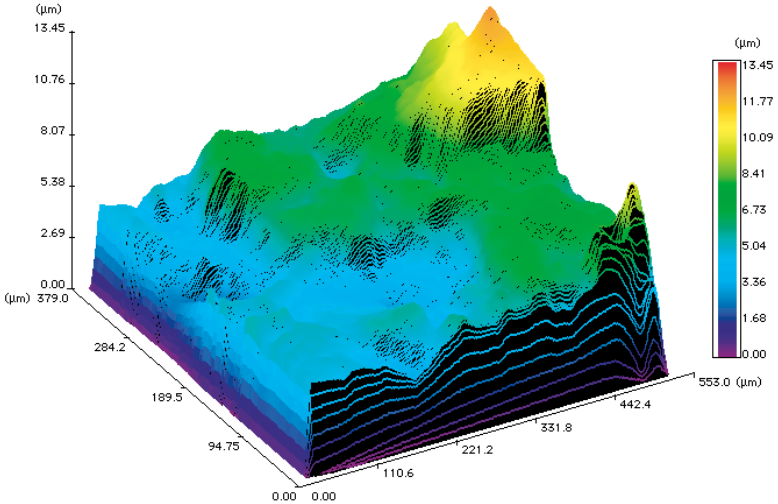

(d) Perspective View of Fracture Surface

FIGURE A-1. FATIGUE FRACTURE SURFACE OF A HIGH-STRENGTH STEEL TESTED IN SEA WATER SHOWING A MIXTURE OF INTERGRANULAR AND TRANSGRANULAR AREAS.

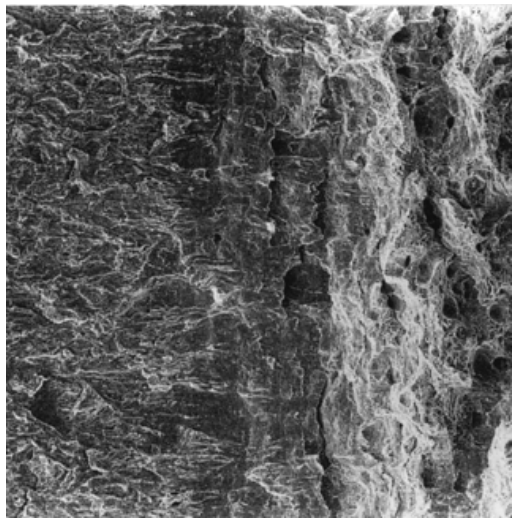

(a) Left SEM Photograph

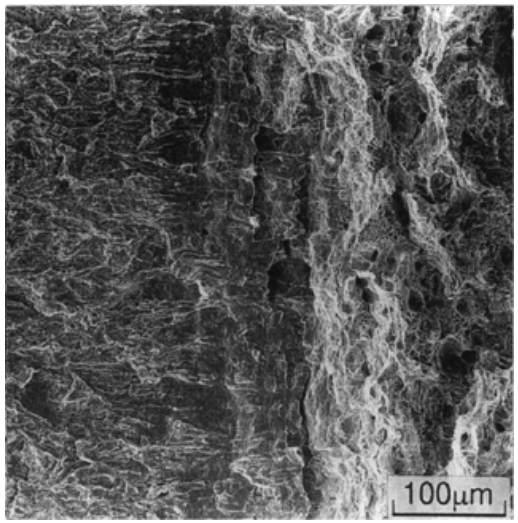

(b) Right SEM Photograph

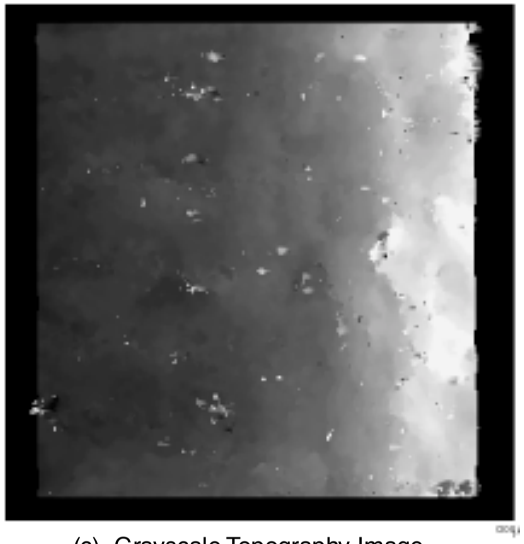

(c) Grayscale Topography Image

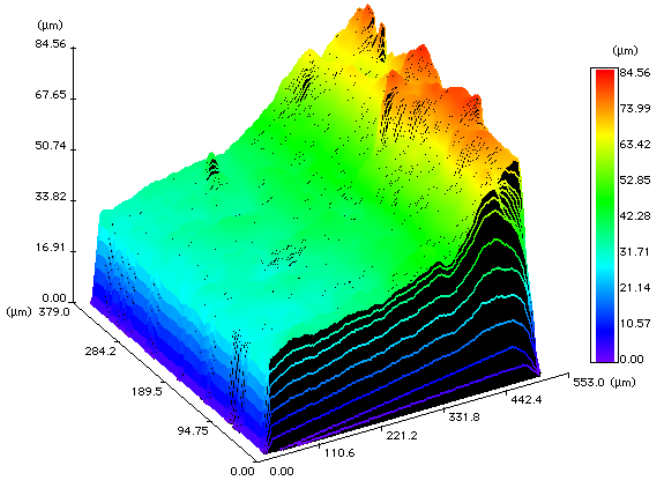

(d) Perspective View of Fracture Surface

FIGURE A-2. FRACTURE SURFACE OF A HIGH-STRENGTH STEEL IN THE VICINITY OF A FATIGUE PRECRACK FRONT SHOWING THE STRETCH ZONE.

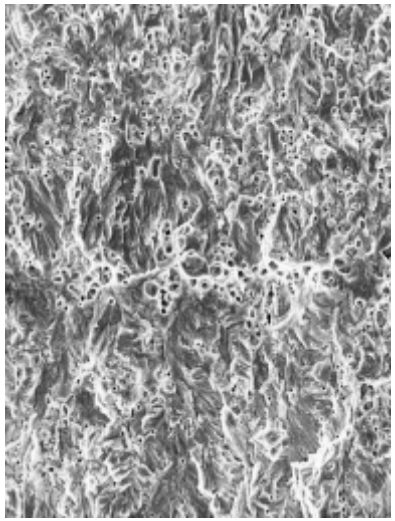

(a) Left Image

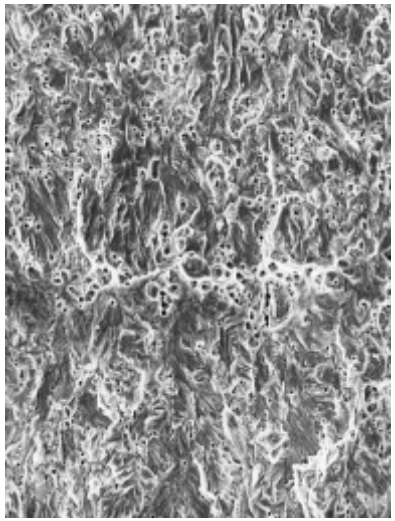

(b) Right Image

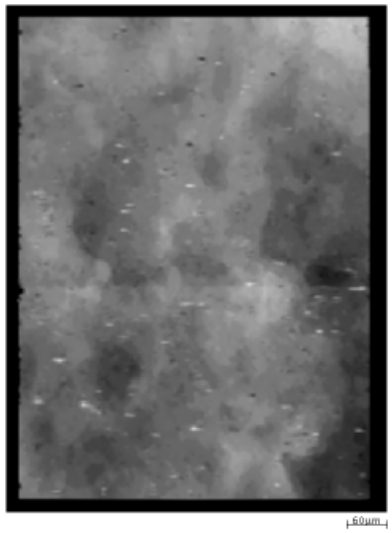

(c) Gray-scale Topography Image

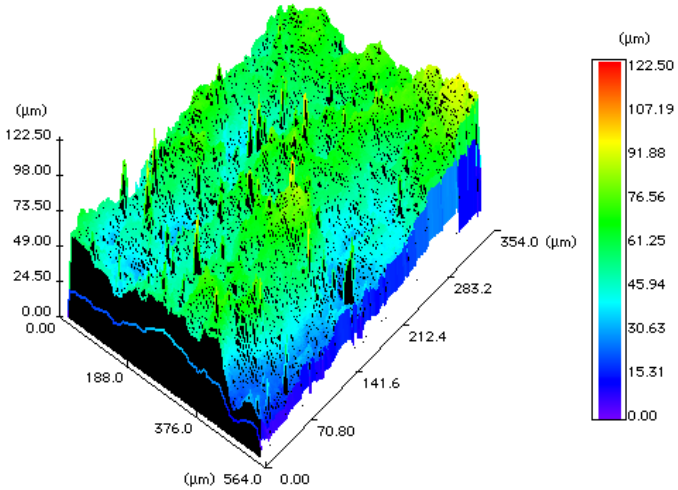

(d) Perspective View of Surface Topography

FIGURE A-3. STEREOPAIR OF SEM PHOTOGRAPHS OF THE FRACTURE AREA WHERE AN OVERLOAD WAS APPLIED DURING FATIGUE LOADING. SAMPLE MATERIAL WAS ALUMINUM 2024-T3 SHEET.